ABSTRACT

Title of Thesis: APPLYING GEODESY TO MODEL POSTSEISMIC SLIP OF THE 2016 MW 6.4 MEINONG EARTHQUAKE

Rebecca Ann Butcher Master of Science, 2019

Thesis Directed By: Dr. Mong-Han Huang, Department of Geology

In regions of rapid convergence such as southwest Taiwan, unmapped active structures at multiple depths increase the uncertainty of seismic hazard estimates. The 2016 M_w 6.4 MeiNong earthquake occurred below the main Taiwan detachment, and may have illuminated some preexisting, but undocumented, fault structures. In this study, I use geodetic measurements to constrain afterslip on the main fault for 15 months following the MeiNong earthquake. The inverted afterslip is concentrated around the peak coseismic slip asperity without significant aftershock correlation, which implies heterogeneous frictional properties on the fault. Additionally, slip model misfit indicates shallower faults that are critically stressed before the earthquake creep due to the MeiNong coseismic stress. My results can help identify active faults located at shallower depth as well as their seismic potential in southwest Taiwan.

APPLYING GEODESY TO MODEL POSTSEISMIC SLIP OF THE 2016 MW 6.4 MEINONG EARTHQUAKE IN SOUTHWEST TAIWAN

by

Rebecca Ann Butcher

Thesis submitted to the Faculty of the Graduate School of the
University of Maryland, College Park, in partial fulfillment
of the requirements for the degree of
Master of Science
2019

Advisory Committee:
Dr. Mong-Han Huang, Chair
Dr. Vedran Lekic
Dr. Wenlu Zhu

Acknowledgements

I'd like to first thank Mom and Dad, for without your endless support and encouragement, I would never be writing this. My advisor, Mong-Han Huang for his patience and for being not only an amazing mentor, but one of my closest friends. Regan Bartha, for still wanting to marry me. Emily McIntire (née Wyatt), for that promise we made years ago to get our master's one day. Sarah LeTarte, for taking on the same challenge with me and crushing it at Missouri State University (we did it!). Alexandra and Angela for being the craziest Geminis, best sisters, and for providing constant motivation in the form of song lyrics and internet memes. James Bader, for giving me the best year of graduate school and memories I will cherish forever. My friends Jessica, Shannan, Javier, and Alex. Finally, my hamster Ubuntu, for being my best friend and helping me through the toughest year of my life, rest in peace little potato.

Table of Contents

List of Tables

List of Figures

List of Abbreviations

GPS - Global Positioning System

CGPS - Continuous Global Positioning System

InSAR - Interferometric Synthetic Aperture Radar

LOS - Line of Sight

ASF - Alaska Satellite Facility

SLC - Single-Look Complex

SRTM - Shuttle Radar Topography Mission

DEM - Digital Elevation Model

SBAS - Small Baseline Subset Algorithm

ISCE - InSAR Scientific Computing Environment

SNAPHU - Statistical-Cost, Network-Flow Algorithm for Phase Unwrapping

VR - Variance Reduction

GPa = Gigapascals

Chapter 1: Introduction

1.1 The Earthquake Cycle

The earthquake cycle is defined by an interseismic, coseismic and postseismic period. The interseismic period is the time during which a fault is loaded with a quasi-static stress variation and begins to accumulate strain. During this interseismic period, the time scale of stress variation can range anywhere from decades to centuries. Strain increases over time in areas where patches on fault planes are locked, or coupled, and began accumulating stress (Interseismic fault in Figure 1a). Once strain accumulated on the fault exceeds its shear strength, strain energy stored in a fault would release and generate an earthquake. This occurs by the locked areas rapidly becoming unlocked and releasing energy, shown by the red step function in Figure 1b. The coseismic period describes the process of slip along the fault plane during this rupture period (Coseismic fault in Figure 1a). Depending on the magnitude, earthquake ruptures can be localized to a few meters of slip or span to hundreds of kilometers and rupture time can vary from a few seconds to a few minutes (*Kanamori,* 1994). The fault rupture velocity is usually ~80% of the S-wave velocity. The stress changes rapidly in the coseismic period causing a stress decrease at some places on the fault surface and an increase in stress at other places. Postseismic deformation is defined as the transient processes that follow earthquakes in the days and even years after large events (*Bürgmann et al.*, 2000). During the postseismic period, stress continues to be released on the main fault, decreasing in strain and causing the fault to continue to slip (Postseismic graph in

Figure 1b) releasing the remaining energy from the coseismic period. Once strain begins to accumulate steadily again, the postseismic period ends and returns to the interseismic period, starting the earthquake cycle again.

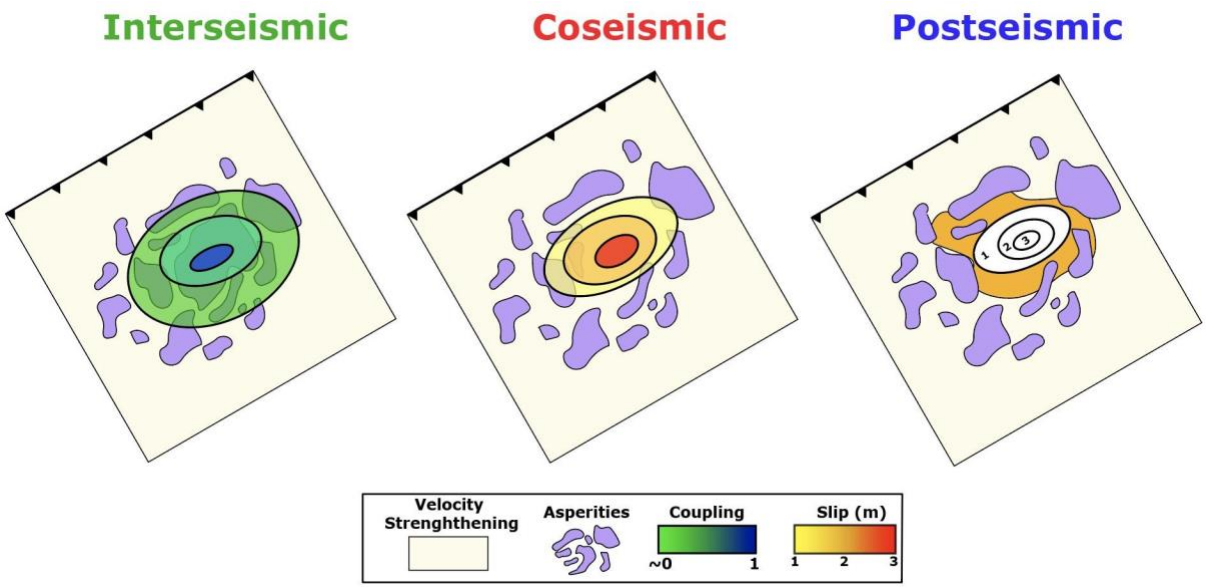

Figure 1a: Fault-scale representation of interseismic, coseismic and postseismic periods (purple is asperities) with graphs of slip and strain overtime (Figure 1b). Interseismic is represented by green lines in slip and strain plot, interseismic fault plane experiences coupling from 1 (blue - locked and accumulating stress) to ~0 (green - weak coupling unlocked or accumulating low stress). Coseismic fault is representing slip (from 1 to 3 meters) on locked portion and red color on slip and strain plots. Postseismic fault has coseismic contour intervals with outline color in slip following the earthquake shown by blue lines in slip and strain plots.

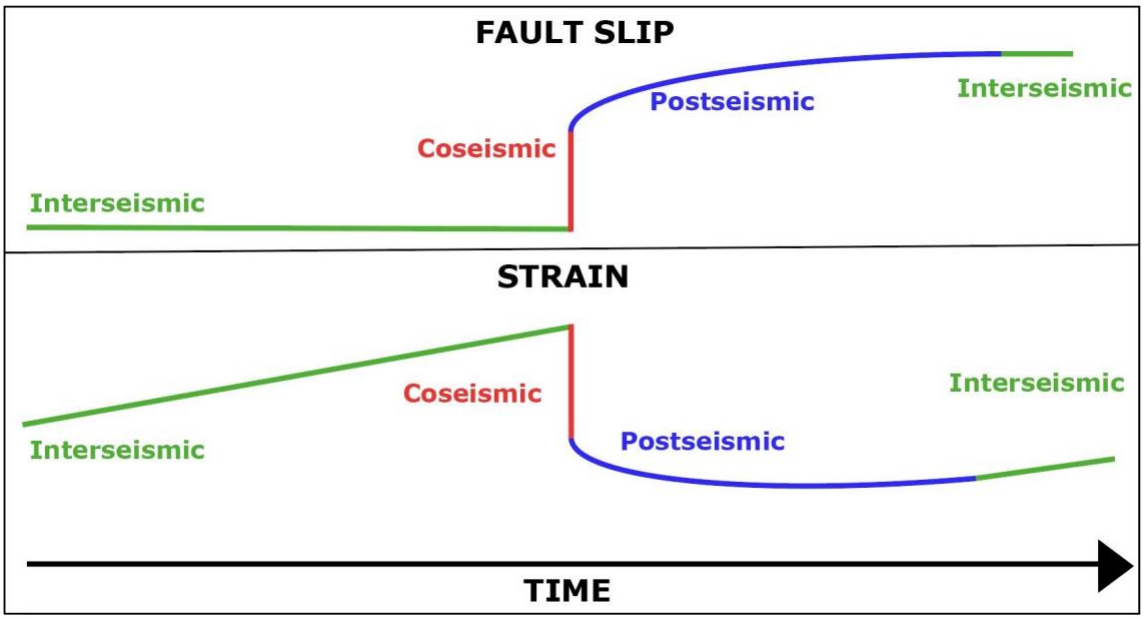

Figure 1b: Graphical representation of interseismic, coseismic and postseismic cycles of slip and strain overtime. Interseismic is represented by green lines. Coseismic is red color. Postseismic period is blue lines.

Depending on the earthquake magnitude, depth, focal mechanism, and location, different types of postseismic deformation behaviors can operate, including aftershocks, afterslip, viscoelastic relaxation and poroelastic rebound (*Bürgmann and Dresen*, 2008; *Wang et al.*, 2012). Afterslip is a considerable mechanism of postseismic deformation in the first few months following an earthquake and is typically defined as aseismic creep on the fault plane (orange area on postseismic fault in Figure 1a). This stable sliding is a result of the release of remaining energy on the fault in areas that were affected by the coseismic stress release (*Scholz*, 1998). The sliding is stable due to areas on the fault that respond by getting stronger with the increase in velocity, this is known as velocity strengthening. In velocity strengthening material, the friction increases with accelerating velocity. This friction increase allows the fault to move without causing additional earthquakes or unstable sliding. It has also been suggested that afterslip can trigger aftershocks to occur on the main earthquake fault in areas

where stress had increased (*Perfettini and Avouac,* 2004). When materials fail in response to a velocity increase, this is called velocity weakening. Aftershocks occur as seismic events following the earthquake in velocity weakening areas on the fault.

Several years following an event that is both deeper into the earth and larger in magnitude, viscoelastic relaxation can begin to appear as postseismic deformation responses (*Wang et al.,* 2012). Viscoelastic relaxation is a slow relaxation response from the upper mantle after the asthenosphere becomes stressed due to the earthquake (*Diao et al.,* 2014).

Another mechanism of postseismic deformation is poroelastic rebound. When a fault undergoes stress changes such as compression and extension, there is a small change in the volume of the surrounding rocks and pore pressure gradient. The change in volume creates changes in the pore fluid pressure gradients around the fault in which fluids move through, and eventually drain out, or 'rebound' to their normal state (*Peltzer et al.,* 1998). Poroelastic rebound occurs on the same time scale as afterslip but is more difficult to model if fault geometries and diffusivity of fluids in the area are not known.

Analyzing postseismic deformation has allowed me to extract valuable information regarding the effects large stress perturbations have on the surface as well as lithospheric rheology (e.g. *Bürgmann,* 2008; *Huang et al.,* 2014). With modern geodetic techniques, postseismic deformation has been studied and documented since the 1960's (*Smith and Wyss,* 1968) which has given valuable insight into the detailed mechanisms of the earthquake cycle.

Chapter 2: Background

2.1 Motivation

The unpredictable behavior of earthquakes and the amount of energy they release makes them one of the deadliest natural disasters on this planet. Earthquakes have occurred since possibly before the onset of plate tectonics and their records are buried within geological structures and cultural documents around the world. The most powerful earthquakes are contiguous with the Pacific Ocean where seismic activity is both prolific and poorly understood due to the lack of observations at seismogenic depths. Earthquakes account for the majority of deaths due to natural disasters, about 60,000 people a year worldwide, most fatalities being from developing countries (OECD, 2008). Worldwide efforts across many disciplines are working together in order to better understand earthquake cycles and identifying active faults. Understanding the earthquake cycles in areas capable of generating large events is one of the first steps in mitigating seismic hazards.

Earthquakes can occur on faults that reach to ground surface to depths of ~700 km. In fold-and-thrust belts along active plate margins, faults can be buried within kilometers-thick sediments. Mapping faults is difficult as we cannot see deep into the Earth. Unknown, unmapped faults are known as blind faults. Earthquakes that occur

on blind faults have greater hazard potential than known mapped faults as there is no direct way to evaluate the slip behavior until an earthquake occurs on the fault. Understanding seismic potential of a tectonically active region is important for future seismic hazard mitigation and assessment.

Recently, the use of satellite geodesy has become a critical technique in the evaluation of earthquake probability analysis. Global Position System (GPS) has very high (mm-level) sensitivity to ground displacement, but due to the limitation of station deployment, it is extremely challenging to provide crustal deformation information down to local (<10 km) scale. It is therefore difficult to estimate interseismic fault creep and locking depth of active faults solely using GPS. Interferometric Synthetic Aperture Radar, or InSAR can instead provide surface deformation at meter-scale spatial resolution. However, the precision of InSAR is relatively lower than that of GPS and can also be influenced by surface physical condition, regional weather pattern, and observation duration (*Bürgmann et al.,* 2000). Since radar interferometry does not depend on field studies, it is also useful in acquiring images of earthquakes that occur in remote locations, a limitation prior to InSAR. SAR archives allow us to retrospectively study surface deformation as far back as 1992, providing valuable baselines of seasonality and background surface behavior prior to events. Using an interferogram produced before and after an event in an area without GPS coverage or previous field benchmarks, we can still accurately study earthquake coseismic deformation.

InSAR grants a high spatial sampling that GPS networks lack as stations are usually spaced a few meters to hundreds of kilometers apart. Interferograms can image

every pixel on the solid Earth surface in locations where water is not present. Combining GPS and InSAR, we are able to cover a much wider region with relatively high (mm-to-cm) accuracy.

2.2 Aim of This Study

In this study, I plan to investigate afterslip as the main postseismic deformation mechanism following the MeiNong earthquake. I will be utilizing geodetic inversions of InSAR and GPS with fault geometry based on *Huang et al.* (2016) and details of shallower tectonic structure by *Le Béon et al.* (2017) to conduct my analysis. Additionally, I will compare month-to-month afterslip total moment release to aftershocks on the main earthquake fault plane. Assessment of seismic hazards along with the better understanding of the seismic cycle grants critical information regarding the capacity of an area to harbor devastating earthquakes within regions of rapid convergence. A thorough geodetic investigation of Taiwan will allow us to better assess the spatial and temporal distribution of slip occurring on unknown faults at various distances following earthquakes.

2.3 Tectonic System of Taiwan

Taiwan is formed as an island arc with a metamorphic basement and thousands of meters of Cenozoic deposits on top of it. The strata of the island are disseminated into a strip-like, N-S trending patterns perpendicular to the converging Eurasian and Philippine Sea plates (Figure 2A). The eastern and western parts of Taiwan are separated by the Central Mountain Range, which is made up of low to high grade metamorphic rocks and rises 0.5 cm/year on average (*Ho,* 1975). The western part of

Taiwan is mostly comprised of marine sediments while east of the Central Range is the Coastal Plains, mostly. To the southwest, the area is comprised of two main geologic settings, the Western Foothills and the Coastal Plain. The Western Foothills (yellow shaded area in Figure 2A) is located west of the Central Range and made up of sediments that were deposited during the Oligocene to the Pleistocene, when major orogeny began. During the early Pleistocene orogeny, the deposited sediments of the Western Foothills became folded and faulted, forming some active structures we see today. The Western Foothills continue towards the west along the deformation front of Taiwan, forming tablelands and merging with the Coastal Plain. This deformation front in the Coastal Plain of southwest Taiwan has many known active faults due to the collisional behavior of the island (Figure 3).

Taiwan is one of the most seismically active regions in the world as it is located at the convergent boundary of the Philippine Sea Plate and Eurasian Plate. The complex collisional configuration and position of the island makes it prone to complicated structures, high density of faults and large earthquakes. At the northeast side of the island, N-S extension is currently taking place at ~3 cm/year in a back-arc region (*Lallemand and Liu*, 1998), while in the south, the Eurasian Plate is subducting under the Philippine Sea plate with a rapid convergence rate of 8.2 cm/year towards N58°W (*Yu et al.*, 1997, *Hsu et al.*, 2009*; Lin et al.*, 2010). Active mountain building and rapid shortening at fold-and-thrust belts can cause faults at various depths to slip during earthquake cycles (*Fielding et al.*, 2004). This observation is also comparable to the characteristics of seismicity and major earthquakes in southwest and central Taiwan as the result of collision between the two aforementioned plates.

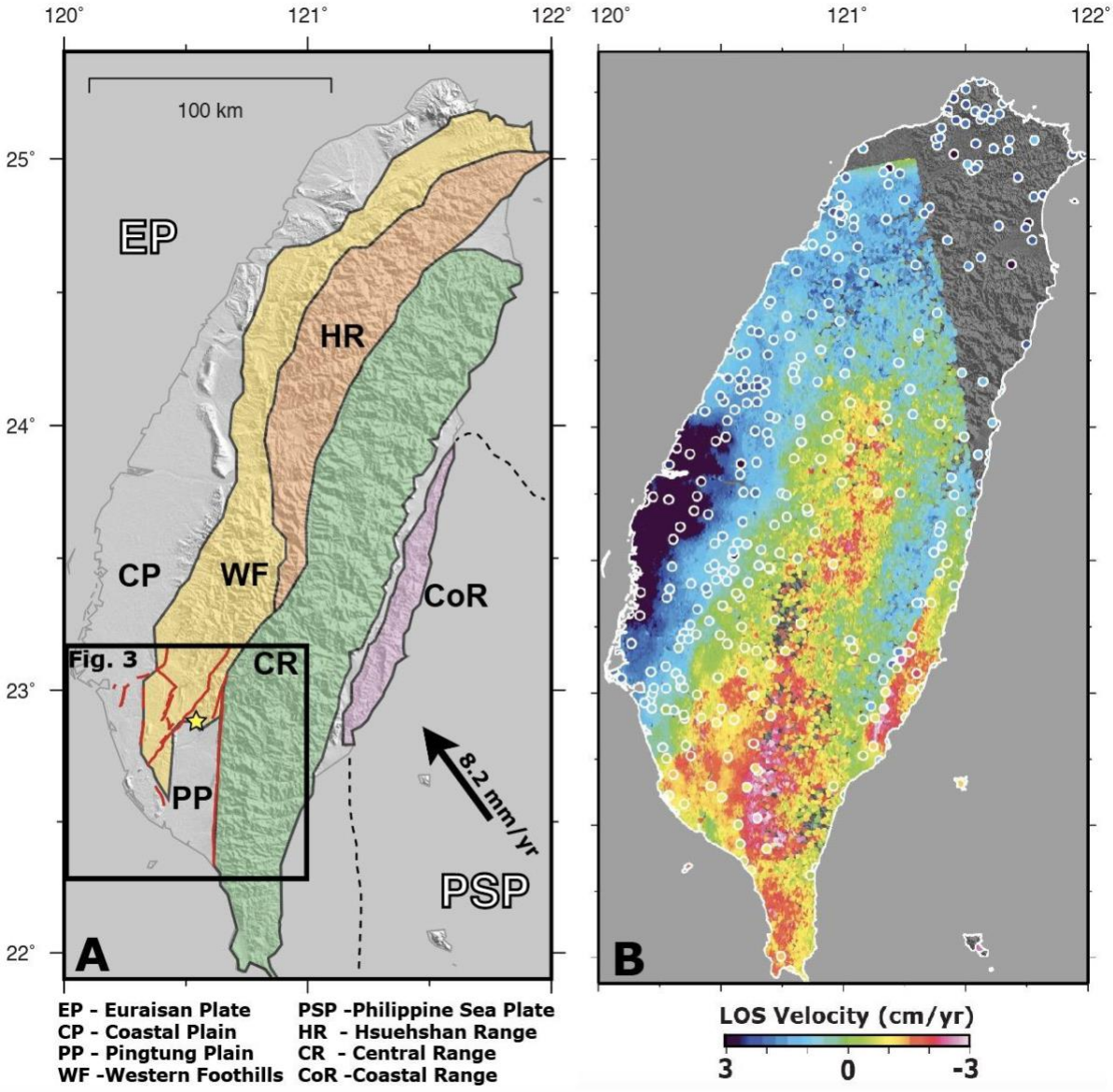

Figure 2: Geologic map of Taiwan (A). Gray indicating quaternary alluvial deposits of the Coastal Plains (CP) and Pingtung Plains (PP), orange indicates Hsuehshan Range (HR) of sandstones, yellow indicating the Western Foothills (WF) comprised of slate, green indicates the Central Range (CR) with schist and volcanics on the easternmost side, the Coastal Range (CoR) is in purple. Philippine Sea Plate is (PSP) and Eurasian Plate is (EP). Black box is outline of Figure 3. (B) Interseismic deformation map of Taiwan. InSAR mean interseismic line-of-sight (LOS) velocity. Blue and red- background colors indicate velocity toward and away from the satellite, respectively. White circles indicate GPS stations with LOS velocity as the color fill.

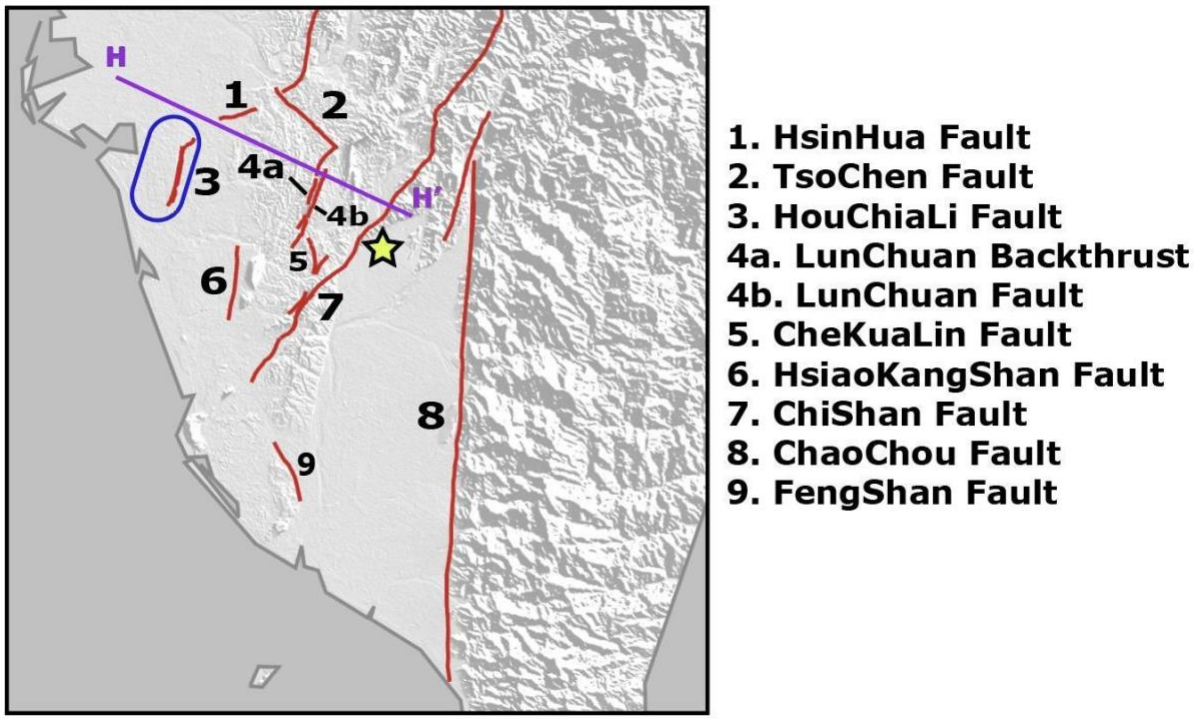

Figure 3: Mapped active faults of southwest Taiwan. Location is cut from black box in Figure 2. Red lines represent active faults. Yellow star is 2016 MeiNong earthquake epicenter. Blue outline is the location of Tainan City on top of the Tainan Tableland. Purple cross-section (H-H') is cross section for Figure 4.

With the complex structural geology of Taiwan in mind, being able to interpret the location of future earthquakes is difficult. Although maps of southwest Taiwan's active faults exist, such as Taiwan Earthquake Model (TEM), these models are difficult to use for the interpretation of blind thrust faults as the model only consists of mapped active faults. An extensive and well documented interpretation of southwest Taiwan was made by the Chinese Petroleum Corporation in 1989 using petroleum seismic reflection surveys. With analyses of the seismic reflections and surface geologic mapping data, *Le Béon et al.*, 2017 re-interpret the structural geology of SW Taiwan (Figure 4). However, this seismic reflection data does not provide information below ~5 km. As accurate imaging past this depth is sparse, it is difficult to assess fault

geometry, fault slip deficit information, and seismic hazard potential below the main detachment where locked faults are located. We therefore should rely on a combination of geodetic data, seismic data and borehole information to generate an interpretation.

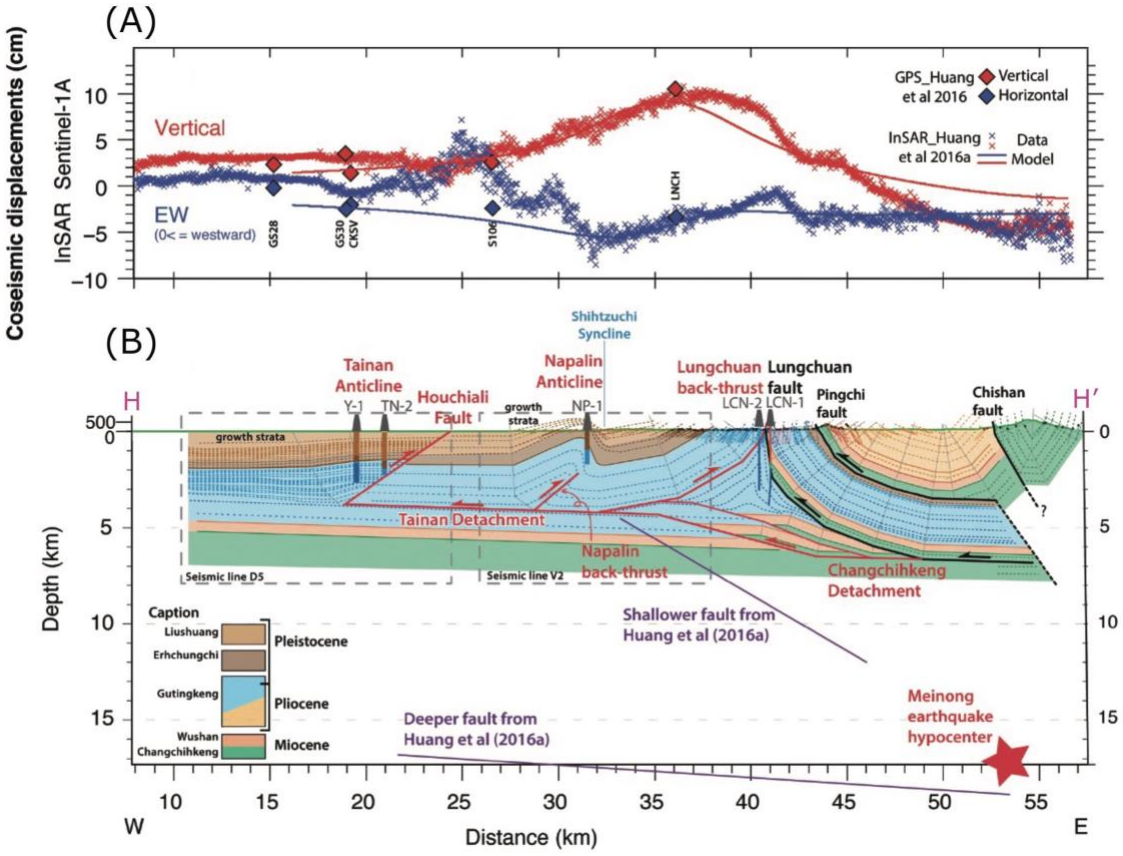

Figure 4: Coseismic vertical (red) and horizontal (blue) displacements in cm (A) of Sentinel-1A InSAR measurements (x marks) and GPS stations (diamonds) GS28, GS30, CKSV, S106, and LNCH. Model fit (solid red and blue lines) from coseismic fault slip model of Figure 5. Cross-section from *Le Béon et al.*, 2017 interpreting the subsurface faults of southwest Taiwan. Borehole data TN-1, TN-2, and LCN-2 (Huang et al. 2004), NP-1 (*Chung*, 1968), Y-1, and LCN-1. Petroleum seismic reflection profiles D5 and V2 (*Chinese Petroleum Corporation*, 1989) with depth conversion performed on line D5 (*Marc et al.* 2010). Red star indicates MeiNong hypocenter. Purple fault geometry is used in this study and orientations obtained from *Huang et al.*, 2016.

2.4 2016 MeiNong Earthquake in Southwest Taiwan

The February 6, 2016 M_w 6.4 MeiNong earthquake was an oblique event with both strike-slip and thrust components (*Huang et al.,* 2016b) that ruptured at 15-20 km depth on a blind fault (yellow star in Figure 2A). This earthquake caused the most severe damage, 117 fatalities and total collapse to 10 buildings, ~30 km west of the epicenter with no significant observed damage to the epicentral region. This event is marked as the deadliest earthquake in Taiwan since the 1999 M_w 7.6 ChiChi earthquake that struck central Taiwan at a shallow ~12.5 km depth. The blind thrust fault that hosted the MeiNong earthquake has no previously recorded seismic activity or mapped information and is located below the main southwest Taiwan detachment.

The complex orientation of faults shown in the southwest Taiwan cross section (Figure 4) makes it difficult to fully understand their interactions with one another. Seismic hazard assessment of densely populated areas dominated by faults is critical to both the economy and the residents of cities such as Tainan, the 4th largest city in Taiwan, that was affected by this earthquake (blue circle in Figure 3). Without having information regarding the locations and orientations of active faulting structures below the main detachment (red line labeled "Tainan Detachment" in Figure 4), there can be significant seismic risk due to these unknown deep fault structures and their slip budget. The coseismic study of the MeiNong earthquake by *Huang et al., 2016* uses a two fault system to explain the surface uplift from the earthquake (Figure 5). Main fault plane is optimized using seismic data and geodesy, while shallow fault is optimized using only geodesy. From the coseismic study, the peak amount of slip from the earthquake on the main fault plane is ~1.2 meters with model fit shown in Figure 4.

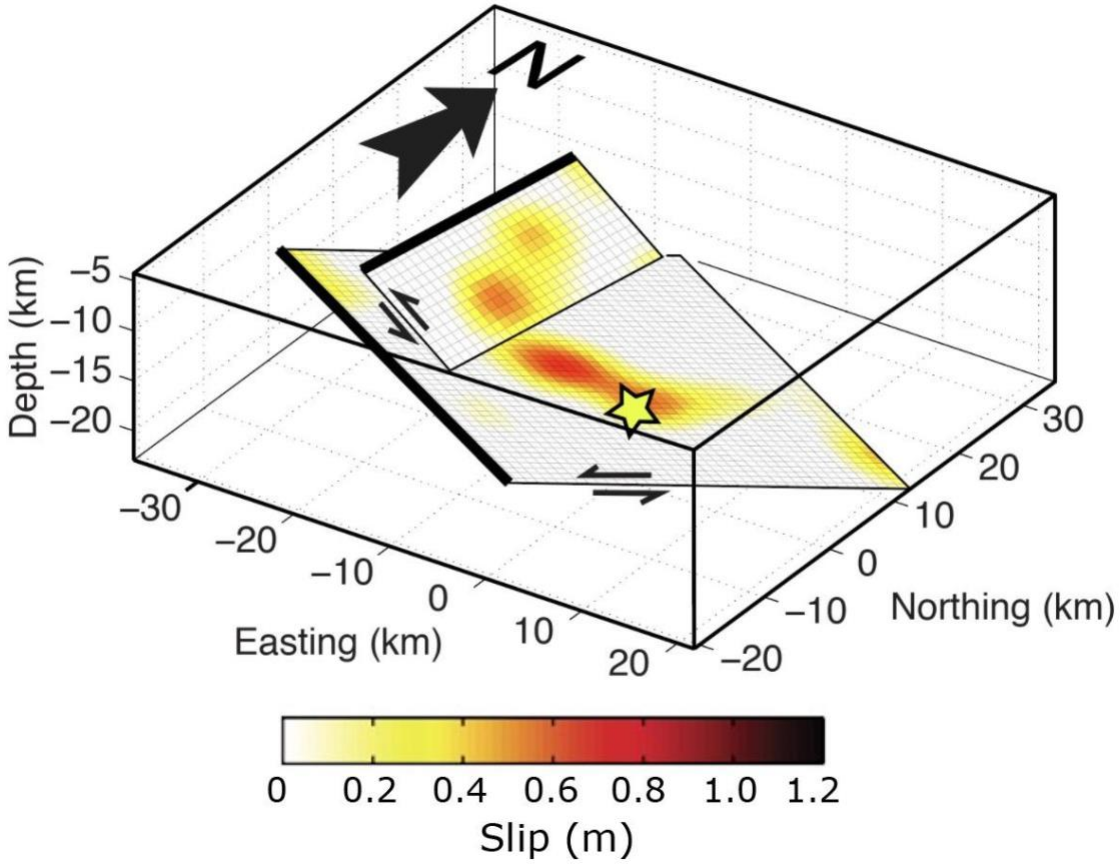

Figure 5: Coseismic slip model by Huang et al., 2016 for the 2016 Mw 6.4 MeiNong earthquake. Yellow star indicates hypocenter. Thick black line represents up-dip direction. Model fit to geodetic surface observations shown in Figure 4.

Recent information has drawn attention to potential seismic hazards lurking within blind faults of southwest Taiwan. Based on geodetic inversions, *Ching et al.*, (2011) suggests that a M_w 6.4 earthquake that is similar to the 2010 JiaShian earthquake could occur every 12-24 years. The NW-striking JiaShian earthquake and the following aftershock sequence had similar depth and orientation to that of the MeiNong earthquake. The JiaShian earthquake occurred on one of a series of E-W strike and north dipping Miocene structures below the main detachment of southwestern Taiwan

(*Huang et al.*, 2013). There have been five *M* ~6 mid-to-lower crustal events that have occurred following the JiaShian earthquake, with the most damaging being the MeiNong earthquake that occurred in 2016.

Chapter 3: Methods

With the advent of satellites, imaging the earth has led to new insights into understanding of lithospheric processes. Interferometric synthetic aperture radar is a powerful tool in observing large-scale surface deformation quickly following earthquakes. Combining this high spatial resolution of InSAR supplemented with the continuous temporal sampling rate of GPS allows for a greater understanding of the earthquake cycle than historically available.

3.1 Obtaining Geodetic Data

Copernicus programme's Sentinel-1 mission comprising of two-polar orbiting satellites under the contract with the European Space Agency (ESA) developed for C-band synthetic aperture radar imaging. Interferograms from Sentinel-1 are obtained as raw data in the form of *Single-Look Complex* (SLC) data downloaded from the University of Alaska, Alaska Satellite Facility (ASF) data portal for remotely sensed imagery of the Earth. The raw SLC products contain focused SAR data that are geo-referenced by using orbit and attitude from the imaging satellite. The SAR data is provided in zero-Doppler slant-range geometry and are corrected for azimuth bi-static delay, elevation antenna pattern and range spreading loss.

The GPS data of southwest Taiwan are obtained from Academia Sinica and the Central Weather Bureau of Taiwan. The GPS stations are maintained by the GPS laboratory at Academia Sinica and the data are available at http://gpslab.sinica.edu.tw.

3.2 Introduction of Geodetic Techniques – InSAR

Synthetic aperture radar (SAR) combines satellite orbit information, an active electromagnetic imaging system, and received signal data to produce high resolution radar images. The radar systems emit bursts of electromagnetic waves and collect the return energy from a target in the antenna look direction (*Osmanoglu et al.,* 2016). Satellite data can be gathered from both ascending (moving south to north) and descending (moving north to south) polar orbitals and are right-looking in this study. Two SAR images taken at different times are combined to generate a radar interferogram, which reveals information about the third dimension (elevation) by measuring travel path variations as a function of satellite position and time of acquisition.

If the ground begins uplifting or subsiding between two satellite acquisitions, we can use changes in the return signal (amplitude and phase) to calculate surface displacement. Taking the phase difference between the two satellite images will give a result of ground motion towards or away from the antenna once topographic and atmospheric effects are removed (Figure 6). Synthetic aperture radar is capable of remotely mapping and monitoring surface deformation from the scale of millimeters to meters. InSAR measurements are sensitive to topography, ground motion, atmospheric conditions, spatial separation between satellites (baseline) and atmospheric conditions (*Ferretti et al.,* 2001; *Colesanti et al.,* 2003).

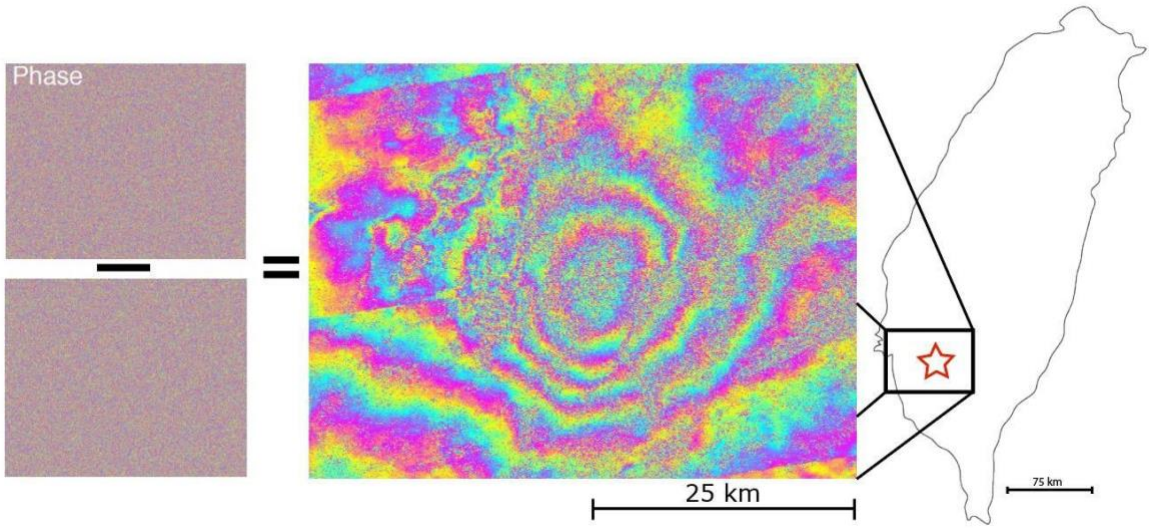

Figure 6: By observing the phase difference between satellite acquisitions before and after an earthquake, we are able to see circular "fringes" in areas where the ground uplifted or subsided rapidly. Each color cycle, or "fringe" represents a phase change of 2π radians. The left two images are two different satellite acquisitions when observed together give the relative motion of the ground in the area the satellite passed over. This image shows the location of the 02/06/2016 MeiNong earthquake (indicated by a red star) and the resulting coseismic interferogram (indicated by the black box) from two satellite acquisitions, the first on 02/02/2016 and the second one 12 days later on 02/14/2016.

I use Copernicus Sentinel-1A (S1A, operated by the European Space Agency) Synthetic Aperture Radar (SAR) acquisitions to generate ascending (track 69) and descending (track 105) interferograms of southwest Taiwan. Sentinel-1 is a day and night, all-weather, two-satellite constellation that has high (100%) transmissivity at 1-10 GHz. The wavelength of Sentinel-1A is 5.6 cm (C-band) and was processed using the topsApp module added to the ISCE (InSAR Scientific Computing Environment) 2.1 software (*Rosen et al.*, 2012). Sentinel-1 satellites are capable of taking images 3 to 6 days apart when the second satellite in the constellation, Sentinel-1B is actively

imaging. In this study, I use both Sentinel-1A and Sentinel-1B satellite data so the time between acquisitions of our dataset varies between 6 and 12 days.

I use Shuttle Radar Topography Mission (SRTM) Digital Elevation Model (DEM) (*Farr et al*., 2007) with one-arcsecond resolution (~30 m) to remove the topographic phase contribution in order to obtain only surface displacements. To unwrap the phase and derive the height values from the products, I use an implementation of the Statistical-Cost, Network-Flow Algorithm (SNAPHU) v1.4.2 (*Chen and Zebker*, 2002). I match InSAR acquisitions creating pairs for every possible date combination within 50 days between October 2014 to January 2018, producing a total of 418 interferograms (271 ascending and 147 descending; Figure 7).

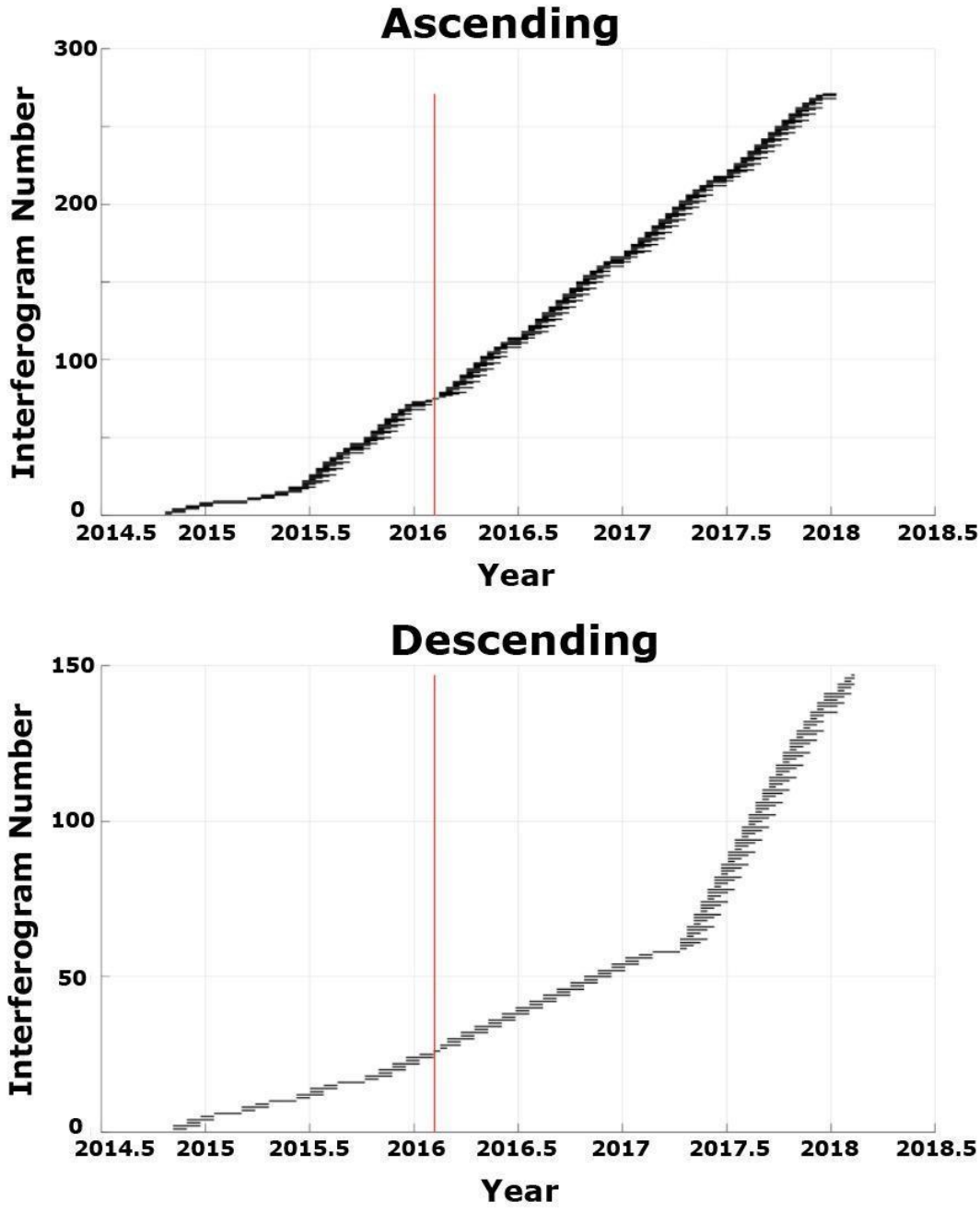

Figure 7: Interferogram acquisition pair combinations for both ascending and descending. Red line indicates the time of the 2016 M_w 6.4 MeiNong earthquake. Interferograms are from Sentinel-1A and Sentinel-1B satellite tracks. Increase in slope on descending plot after 2017 represents where an earthquake occurred in northern Taiwan promoting the European Space Agency to turn on Sentinel-1B satellite.

To construct a continuous record of ground deformation over 15 months, I use a modification of the Small Baseline Subset (SBAS) algorithm (*Berardino et al.,* 2002) and apply it to single-look interferograms. This technique allows me to produce a time series of InSAR data of a small area with a short time span between acquisitions. Using shorter distances in baseline geometry and shorter time between acquisitions allows for reduced cross-correlation between the two signals. I then generate both ascending and descending time series to observe interseismic, coseismic and postseismic surface deformation of southwest Taiwan adopting the method used in *Huang et al.* (2016a). Using both ascending and descending orbits allows for differentiation between the vertical and horizontal components of surface deformation. Using the surface displacement data from both GPS and InSAR, I can create models of faults at depth and compare the predicted surface deformation of our models to the actual surface deformation of our geodetic data.

3.2.1 Comparison of Seasonal InSAR Coherence

As I am conducting a study using data collected over multiple years, changes in the seasons, and therefore the conditions of the atmosphere, will vary significantly. There are usually changes within the time between the two satellite acquisitions that is defined as $\hat{\gamma}$, a function of expected value of the interferometric phase. Coherence is similar to correlation in which I can use estimates of coherence to observe the quality of complex data. Coherence is defined as:

Equation 1:

$$\hat{\gamma} = \frac{\sum_{i=1}^{N} u_{1i} u_{2i} *}{\sqrt{\sum_{i=1}^{N} |u_{1i}^2|} \sqrt{\sum_{i=1}^{N} |u_{2i}^2|}}$$

Where N is defined as independent image samples, u is the product of the amplitudes of the two initial images. The value of coherence, $\hat{\gamma}$, ranges from 0, less coherent, to 1, which is more coherent. Using this equation, I do a comparison of southwest Taiwan coherence in both wet and dry seasons in order to observe and document possible uncertainties in my results.

Taiwan has relatively high humidity as it is situated in the subtropical zone, with the southwest coastal location having the highest humidity of the whole island. Central Weather Bureau data from 1971 to 2010 indicates an annual mean humidity of 81% in the southwest coastal region (*Lin et al.,* 2017), the area of interest for our study. A large change in the relative humidity of an area can lead to significant errors in satellite data of measured ground deformation (*Zebker et al.,* 1997). Increased amounts of moisture in the troposphere will slow electromagnetic waves, while waves traveling through the dispersive nature of the ionosphere tend to accelerate the waves. The acceleration and deceleration of the wave phases decreases the uncertainty and coherence of InSAR images making it more difficult to differentiate noise from actual surface deformation.

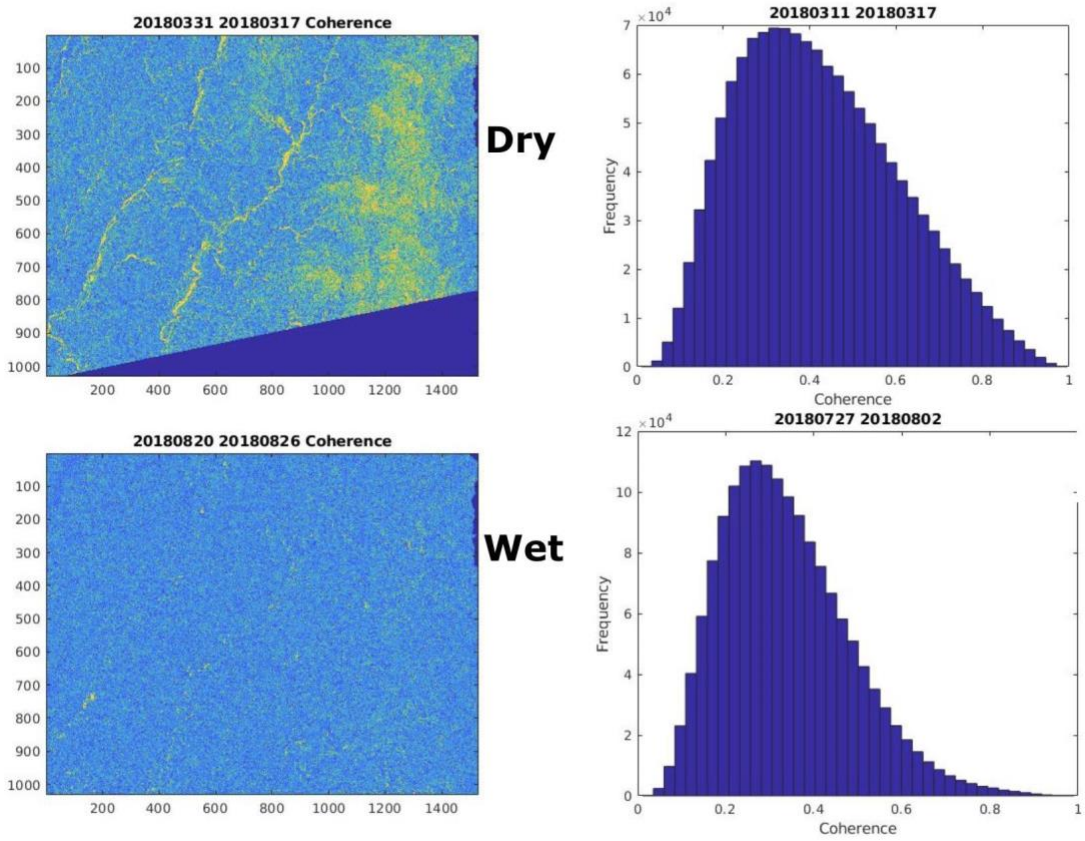

Figure 8: Comparison of the amplitude of InSAR coherence between wet and dry seasons. Dry season acquisitions are March 11, 2018 and March 17, 2018. Wet season acquisition is July 27, 2018 and August 2, 2018. Gaussian distribution represents coherence of the whole image. Brightness represents the higher coherence.

Plotting pixel coherence across an image in both wet and dry seasons shows a normal distribution with dry coherence centered around ~0.3 and wet coherence centered around ~0.25 (Figure 8). Comparing the images from a 6-day pair of acquisitions taken during the wet season and dry season show a noticeable difference in the ability to distinguish rivers and topography. The brighter image (dry image in Figure 8) shows higher amplitude of the return signal from the satellite acquisitions. By just observing the images, it is clear the dry season is easier to distinguish from the grainy wet season. After graphing the coherence of the image pixels, the mean

coherence in the wet season is overall lower than in the dry season. Though the mean coherence of the images is different, the maximum coherence for acquisitions in wet and dry season can vary significantly (Figure A16). After performing a two-sample t-test and selecting a critical value of 2.3 with 8 degrees of freedom, I obtained a calculated t-statistic of 0.28. Indicating that there is a negligible difference in coherence between wet and dry seasons before atmospheric corrections. Given that the atmospheric phase is usually a random distribution, stacking InSAR images reduces the effects of this uncertainty.

3.3 Introduction of Geodetic Techniques – GPS

A limitation to InSAR is the inability to monitor the evolution of terrain and man-made structures on-demand and in real-time. Using terrestrial observations such as GPS overcome this limitation especially in Taiwan, an island that is host to of the densest GPS networks in the world. Over 390 continuously recording GPS (CGPS) stations are located in Taiwan and are operated by Academia Sinica, Central Weather Bureau and Ministry of Economic Affairs. In this study, I select 120 GPS stations in southwest Taiwan within the coordinates 120ºE-120.7ºE, 22.6ºN-23.4ºN to cover the MeiNong postseismic deformation.

3.4 Limitations of Geodetic Data

Uncertainties in satellite data can arise from the effects of the troposphere and ionosphere, which introduces noise that can make images difficult to interpret. Errors are introduced when the satellite's electromagnetic waves are slowed down due to the

atmosphere. Uncertainties can also arise during phase unwrapping such as discontinuities as a result of terrain slopes and low signal-to-noise ratios (*Allen,* 1995).

GPS stations can be deliberately interfered with by people or animals and the equipment can also degrade over time causing uncertainties in the acquired data. Other sources of error include monument instability and loading of the crust by oceans and surface water (*Williams et al.,* 2004). External effects on GPS stations such as equipment failures and changes in the environment may also have effects on the accuracy of GPS time series. Signal propagation effects include receiver noise, ionosphere and atmosphere effects and signal scattering. Understanding the amplitude of noise and seasonality helps to remove these contributions from the data but does not remove the uncertainty all together.

3.5 InSAR Correction

In order to improve InSAR postseismic observations in far-field, I use the acquired GPS data to constrain the InSAR displacement in long wavelength. To achieve this, I first convert the GPS displacement data from 3-dimensions (east-west, north-south and vertical) to line of sight (LOS) in both ascending and descending orbits and calculate the difference between GPS simulated LOS and the closest InSAR sampling from the GPS station. Then, I fit the difference with a plane function using least squares. I finally remove this plane function from the InSAR measurements, so the InSAR long-wavelength displacement is approximately the same as the CGPS measurements (Figure A17). In order to distinguish postseismic signal from these other possible motions before, during, and after the MeiNong earthquake, I analyze CGPS time series data from late 2010 to the end of 2017. Using a time series allows for the ability to

distinguish postseismic deformation from annual and semiannual periodic motions, coseismic deformation and secular motions with a position model (Equation 2):

Equation 2:

$$y(t_i) = a + bt_i + c\sin(2\pi t_i) + d\cos(2\pi t_i) + e\sin(4\pi t_i) + f\cos(4\pi t_i) + g\,H(t_i - t_{eq}) + k\log[1+(t_i - t_{eq})/\tau]\,H(t_i - t_{eq})$$

Where *a* is the initial position (background noise) and *b* is secular motion (slope in the displacement is velocity) with linear rate (Figure 9). Seasonality is represented by annual (terms *c* and *d*) and semiannual (terms *e* and *f*) periodic motions (Figure 10 & 11). The time of the earthquake is t_{eq} and coseismic deformation is estimated by term *g* representing earthquake magnitude multiplied by the discontinuous Heaviside step function, H. Postseismic deformation is represented by the logarithmic decay model where the amplitude of postseismic deformation is *k* and τ is the time decay constant (*Ding, et al.,* 2015*)*.

Annual and semiannual periodic motions can arise from groundwater pumping or rainy versus dry season ground changes. Background noise can include interseismic strain rate and contributions from atmospheric affects or environmental changes.

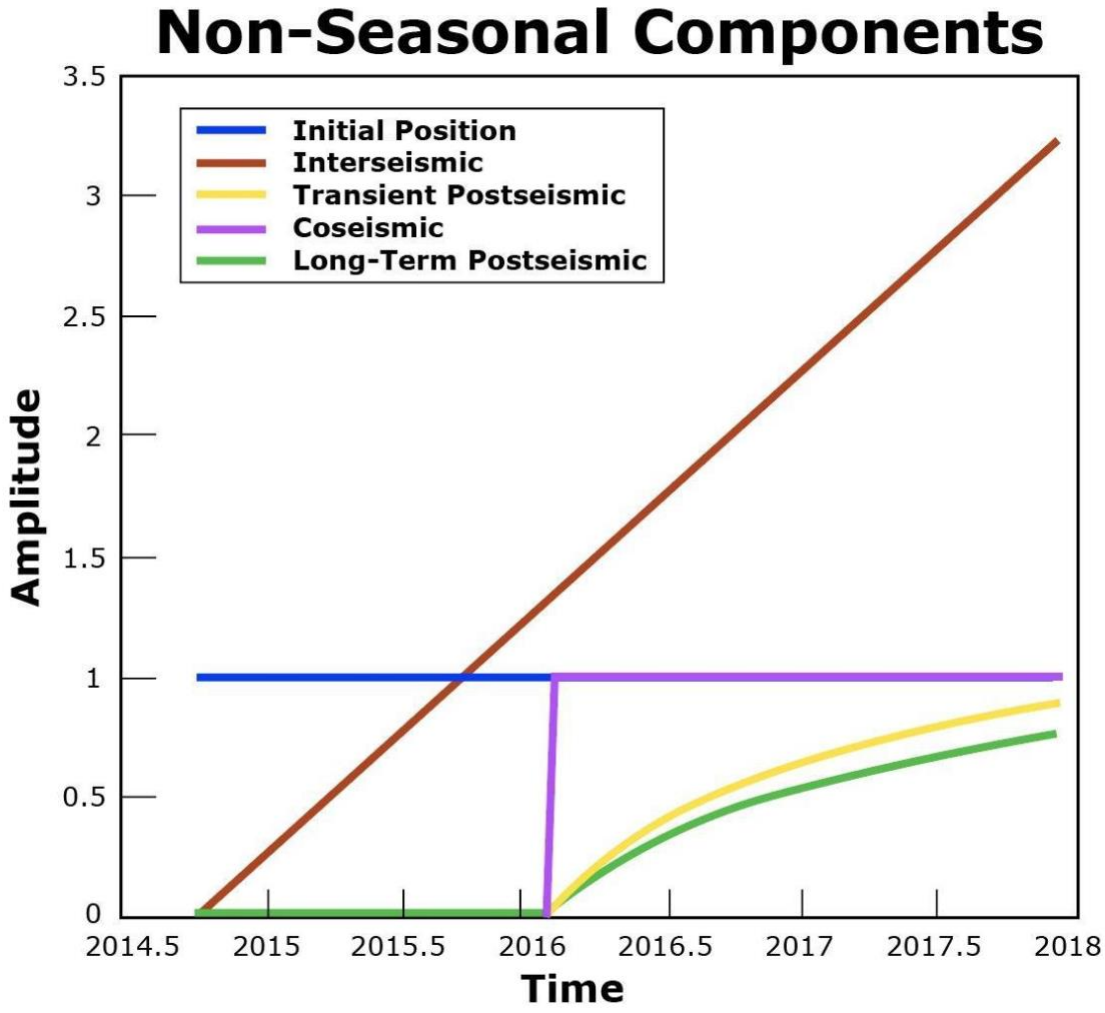

Figure 9: Non-seasonal components used to estimate postseismic deformation of the MeiNong earthquake. Initial position (amplitude of the background noise) is the blue line (term a in Equation 2), interseismic displacement is the orange line (term b in Equation 2), transient postseismic displacement is the yellow line (term k in Equation 2), coseismic displacement is the purple line (term H in Equation 2) and long-term postseismic displacement is the green line (term k in Equation 2).

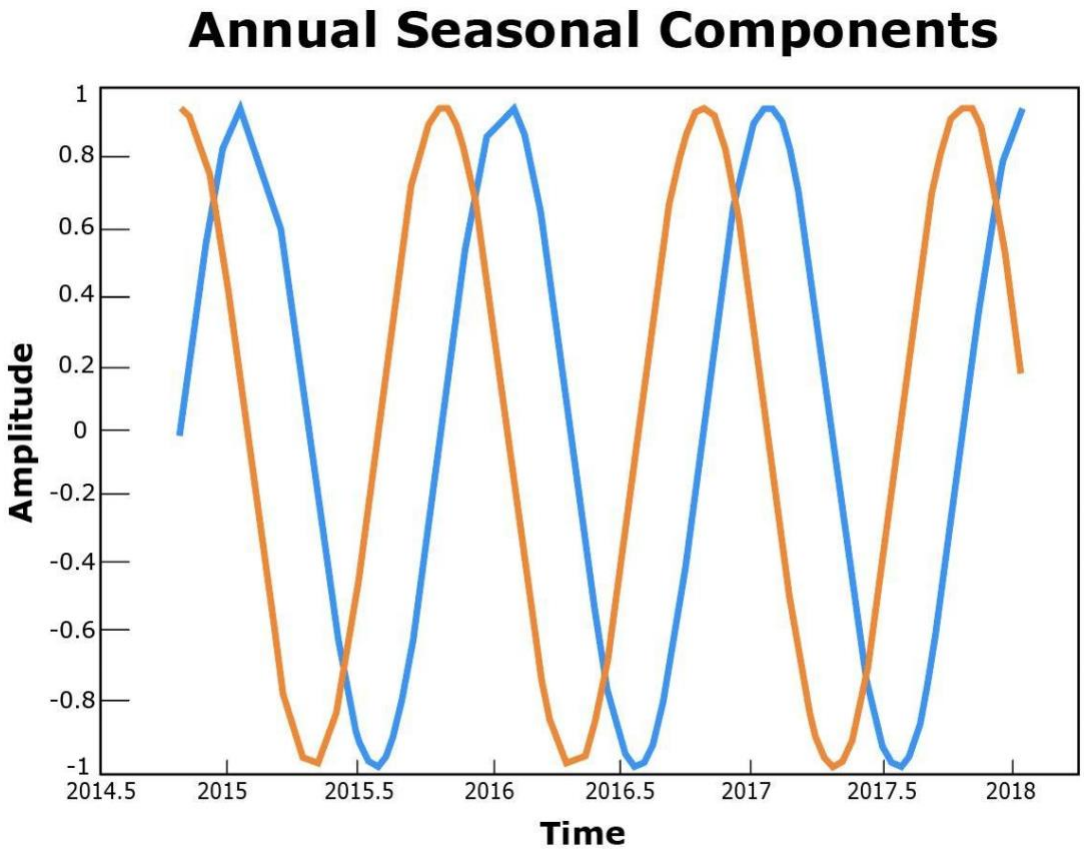

Figure 10: Annual seasonal components used to estimate postseismic deformation of the MeiNong earthquake. Blue and orange line represent annual components (terms c and d in Equation 2). Yellow and purple lines represent semi-annual components (terms e and f in Equation 2). Y-axis is amplitude.

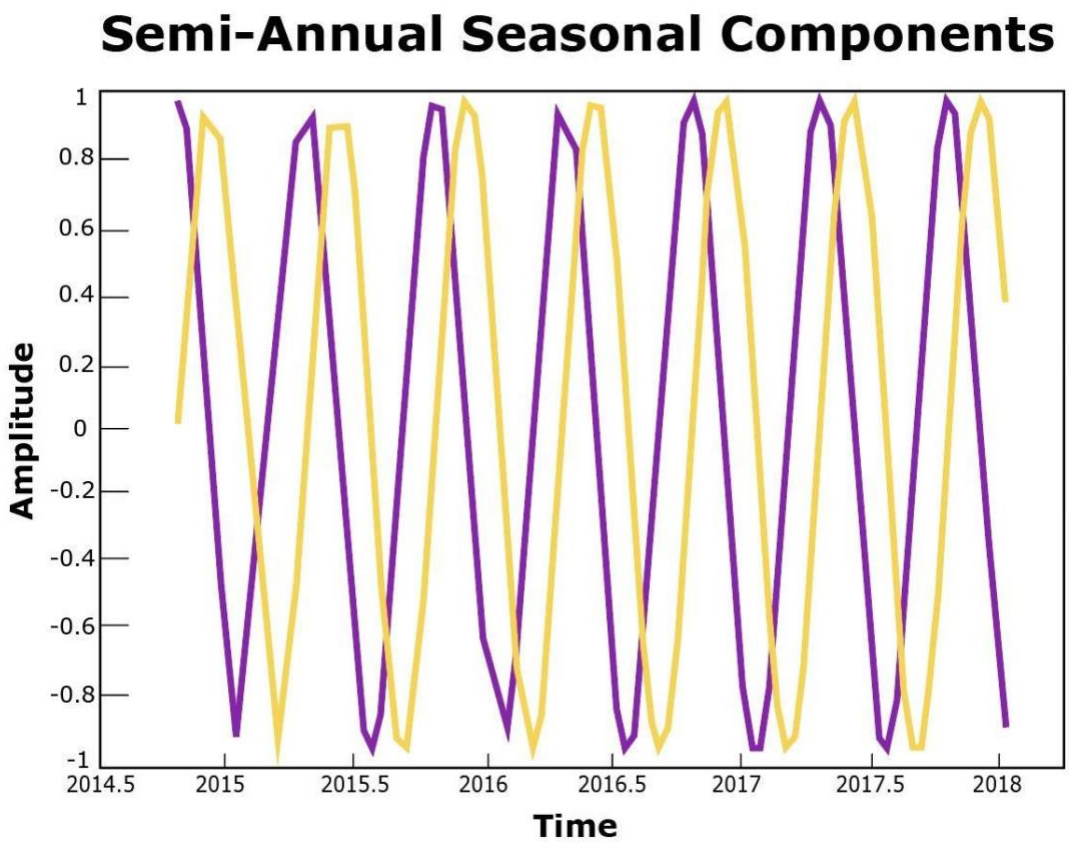

Figure 11: Semi-annual seasonal components used to estimate postseismic deformation of the MeiNong earthquake. Yellow and purple lines represent semi-annual components (terms e and f in Equation 2). Y-axis is amplitude.

Removing the non-deformation phase components from the data allows me to view a stack of interferograms separating the interseismic, coseismic, and postseismic periods and observing the deformation from each. I use the corrected interferograms and GPS data to construct fault models and time series of the earthquake-related deformation history.

3.6 Inversion of GPS and InSAR

Finite source inversion combines both InSAR and GPS to model slip distribution following a similar approach as described in *Huang et al.* (2016b). Green's

functions are equations used to describe a surface response from slip on a fault. In this study I use the EDGRN/EDCMP code (*Wang et al.,* 2003) to compute Green's functions for southwest Taiwan, adopting the same one-dimensional (1-D) horizontally layered velocity structure (Table 1) as described in *Huang et al.* (2013). I use the similar fault geometry optimized in *Huang et al.* (2016b) with the strike, dip and rake of the fault being 299°/15°/48°, respectively. I slightly decrease the size of the fault plane along strike and down dip by 4 km creating a new fault length and width of 40 km. This 40 km x 40 km fault plane is then discretized into sub-faults measuring 1 km long and 1 km wide.

Table 1: Five-layer velocity structure of western Taiwan used for inversions.

DEPTH (km)	THICKNESS (km)	Vp (km/s)	Vs (km/s)
0.0	2.5	4.339	2.478
2.5	12.5	5.662	3.344
15.0	15.0	5.87	3.413
30.0	10.0	6.419	3.616
40.0	∞	7.8	4.5

For slip distribution, I use a non-negative least squares (NNLS) subroutine to invert for slip at every sub-fault patch across the main fault geometry with GPS and InSAR as data constraints. For joint inversions, I first determine weighting between both datasets by initially weighing the GPS and InSAR data equally, then regularly increasing GPS weighting as I was underfitting GPS data in the inversions. Inversions were performed using the two-fault system from *Huang et al., 2016,* the two-fault

system including the detachment fault from *Le Béon et al.*, 2017, as well as a just the main earthquake fault. I use these different inversions to observe the differences in variance reduction in order to determine the best fit model. Using the single fault system, I select weight parameters by allowing the InSAR dataset to be fit without substantially degrading the GPS fit. To achieve an optimal smoothing value and weighting between the two geodetic datasets, I examined the tradeoff in the variance reduction for each data type. I select weighting parameters (purple stars shown in Figure 12) then test a range of smoothing parameters as shown in Figure 13. A final weighting was selected for both data sets of InSAR set at 1 and GPS fixed at 7. With the values of weighting and smoothing fixed, I run all inversions using these parameters.

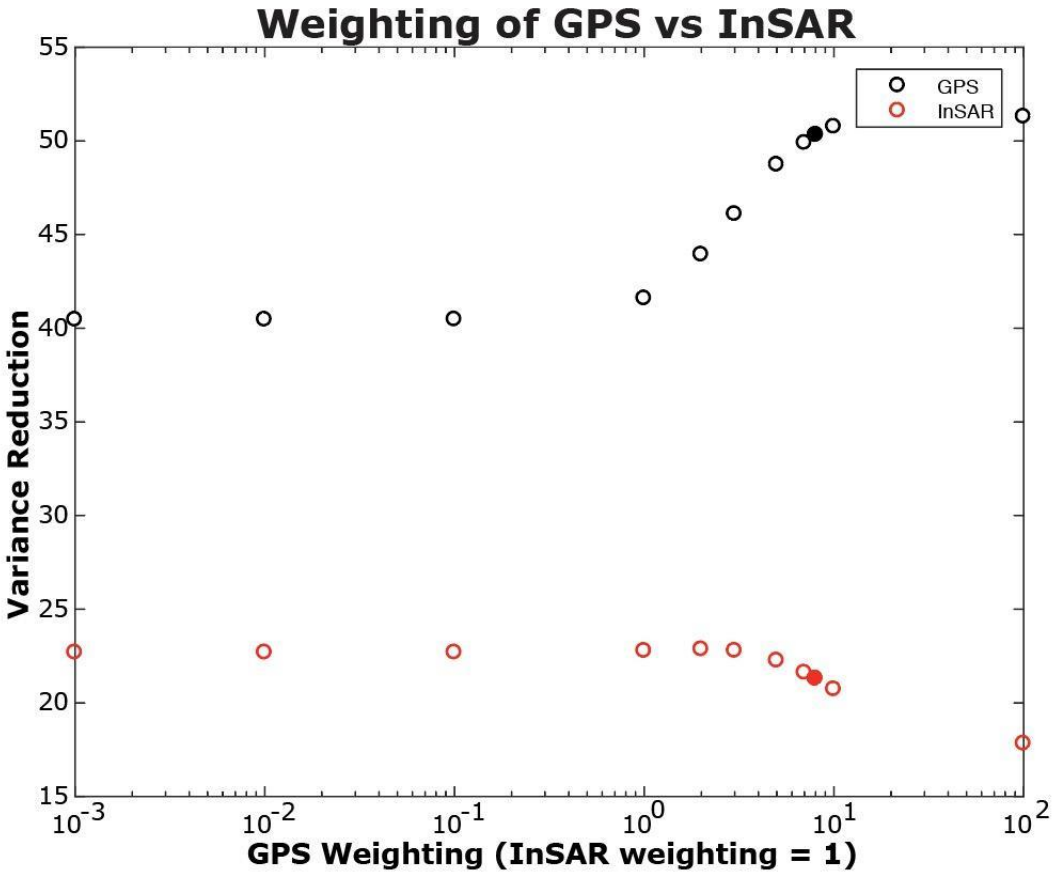

Figure 12: Weighting of both GPS and InSAR. Variance reduction for GPS and SAR measurements indicated by the different weighting with InSAR as the fixed dataset. The solid circles indicate the preferred GPS weighting.

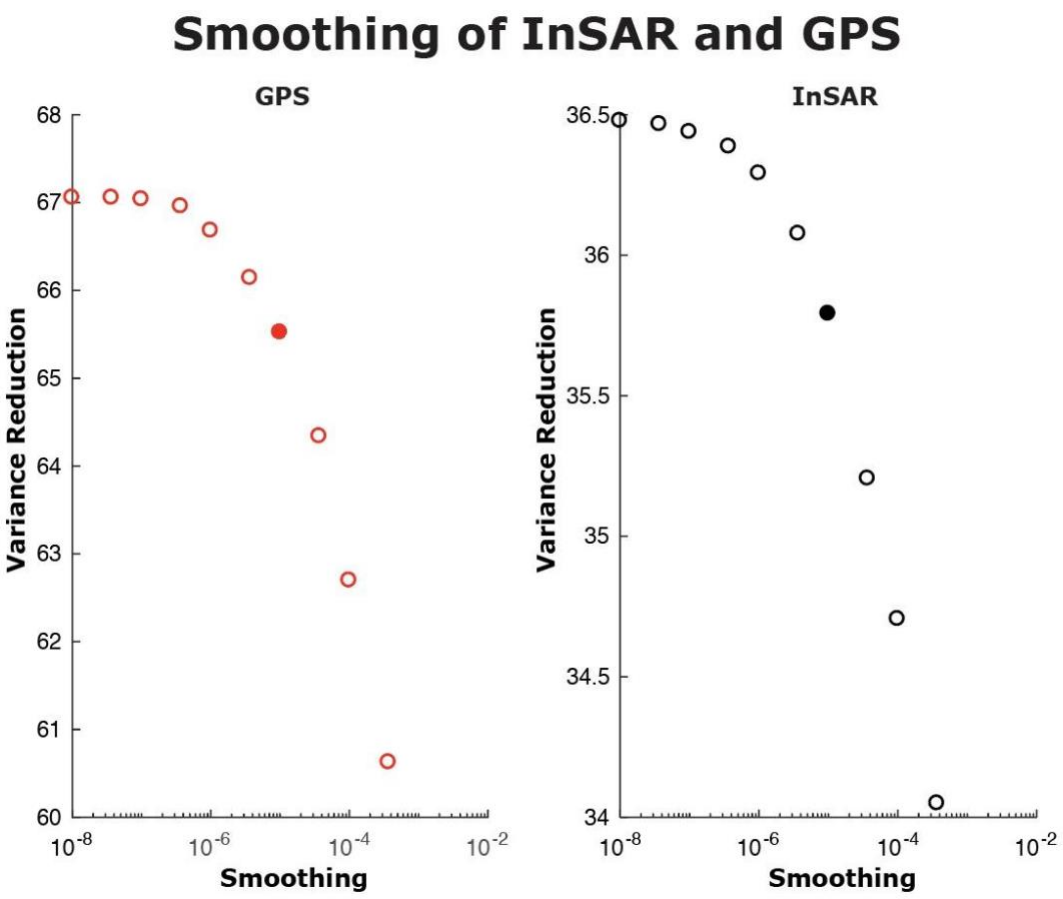

Figure 13: Smoothing of InSAR and GPS with percent variance reduction. Optimal smoothing selected was 10^{-5} as indicated by solid circles on both GPS and InSAR plots.

To better observe slip distribution after setting both GPS and InSAR weighting, I adjust the Laplacian-smoothing operator to obtain the highest percent variance reduction (Equation 3). Adjusting the smoothing is used to avoid overfitting or underfitting the model for both datasets and to prevent impossible oscillatory slip on the fault (*Harris and Segall,* 1987). Variance reduction is defined below, where d_i is the observed data and s_i is the prediction based on the model:

Equation 3:

$$VR = \left[1 - \frac{\sum_i (d_i - s_i)^2}{\sum_i d_i^2}\right] \times 100$$

With the data properly weighted and smoothing applied, I am able to generate a monthly distribution of afterslip on the main fault for 15 months following the earthquake. Afterslip inversions on the main fault are then used to generate a predicted surface displacement model that is useful in comparing the actual geodetic data for a model fit comparison.

3.7 Aftershock Observations

For aftershocks, I use the relocated seismicity catalog compiled by the Central Weather Bureau in Taiwan. Due to high background seismicity in southwest Taiwan, I constrain the spatial distribution of the aftershocks to 5 km above and 5 km below the main fault plane. In this study, I only consider seismicity within this depth range and the spatial range of 120.25°E to 120.65°E and 22.75°N to 23.22°N as aftershocks on the main MeiNong earthquake fault (colored dots in Figure 14).

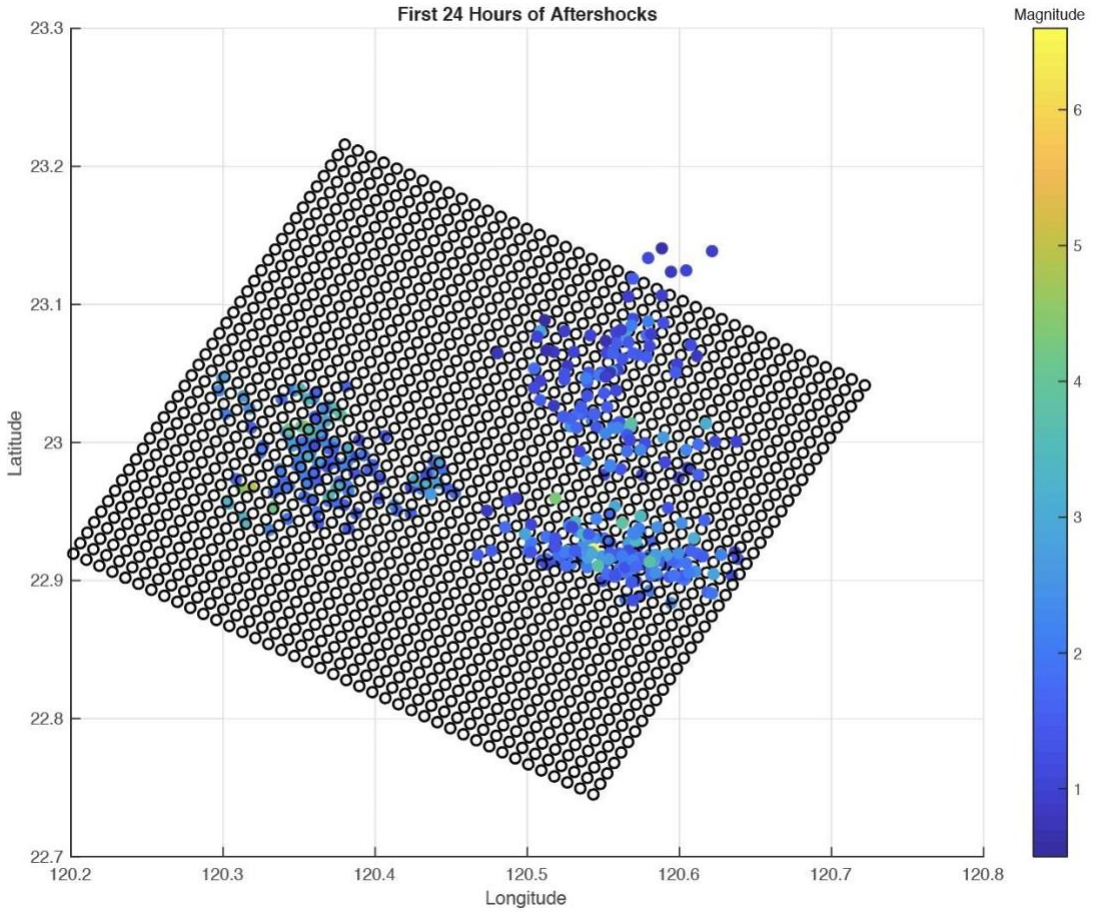

Figure 14: First 24 hours of aftershocks from the 2016 M_w 6.4 MeiNong earthquake above and below the main fault plane. Filled circles represent aftershocks and color represents magnitude. Black shaded box is the main fault plane from the MeiNong earthquake.

In order to remove background noise from the analysis, I plot a time series of cumulative seismicity of southwest Taiwan since 2015. Using this, I estimate a linear trend of cumulative seismicity before the MeiNong earthquake and remove this trend from the post-earthquake time series. I then remove aftershocks that are less than M 1.0 in order to keep background seismicity and noise from interfering with our observations. Comparing geodetic inversions to seismicity data allows us to observe the spatial-temporal relationship between aftershocks and afterslip within the area of the main earthquake fault. In observing the temporal aftershock behavior, I use the

cumulative seismicity within the same depth range before the MeiNong earthquake to estimate the background seismicity rate. With the background noise calculated, I can then remove this contribution from the postseismic time series and observe the temporal decay.

3.8 Stress Driven Afterslip

The stress driven afterslip model is estimated only considering stress changes due to the earthquake as the source of afterslip. I use Coulomb 3.3 software to observe stress-driven afterslip due to the coseismic stress release (*Toda et al.,* 2011). For the Coulomb input parameters, I use the standard input for the coefficient of friction of $\mu = 0.3$ assumed to be constant for all faults, and the shear modulus, *G*, is 32 GPa. The Young's modulus, *E*, is 80 GPa with the dimensionless Poisson's ratio (PR) of 0.25. The main fault strike, dip, and rake is 299°, 15°, and 48°, respectively. The shallow fault strike, dip, and rake are 8°, 30°, 100°, respectively. The detachment strike, dip, and rake are 0°, 5°, 90°, respectively from *Le Béon et al.*, 2017. I do not know if the fault extends far from ruptured area, but I assume that the source of localized deformation is afterslip triggered by stress increase around the rupture area, similar to *Fukushima et al.,* 2018. I then convert from the output file of stress in bar to slip in meters using the earthquake Moment (M_o) equation in order to obtain slip (d):

Equation 4:

$$M_o = \frac{16}{7}\Delta\sigma_c r^3 = Gad$$

In which $\Delta\sigma_c$ is the stress drop from Coulomb, *G* is 25 GPa, and is area of slip. To solve for slip (*d*):

Equation 5:

$$d = \frac{16}{7}\frac{\Delta\sigma_c}{G}r$$

In order to convert from radius of a circle used in M_o to area of a square used in *d*, I multiply the value of d by 1.27, since the squares are 1.27 times greater than the circle. I need to convert from a circular area of slip to a square in order for the model to work as my fault is discretized into squares.

Chapter 4: Results

4.1 Geodetic Results

4.1.1 Coseismic Displacement

The peak vertical coseismic displacement from InSAR (red background color in Figure 15) shows a maximum of ~10 cm uplift area that is roughly 9 km wide by 21 km long. GPS station LNCH (labeled in Figure 15) located about ~15 km away from the epicenter also recorded peak coseismic uplift as ~10 cm. The coseismic horizontal displacement of InSAR and GPS both show westward motion during the earthquake in the same area as the peak coseismic uplift. A small area ~1.9 km wide by 3 km long at 120°16'E, 23°01'N, shows significant eastward motion visible from InSAR near the end of the HsinHua Fault (Number 1 in Figure 3). This could possibly indicate liquefaction as there is no visible vertical coseismic displacements (Figure 15). This area is also near the location of significant structural damage and collapse of a residential building.

The GPS and InSAR coseismic displacements estimated from time series modeling (i.e. g in Equation 2) are in good agreement in both horizontal and vertical components (Figure 15 & 16). Surrounding the epicenter (red star in Figure 15 & 16) in the vertical, there is significant subsidence in InSAR measurements which could be a result of background noise or contribution from a north-south coseismic displacement that cannot be well separated (*Huang et al.*, 2016b).

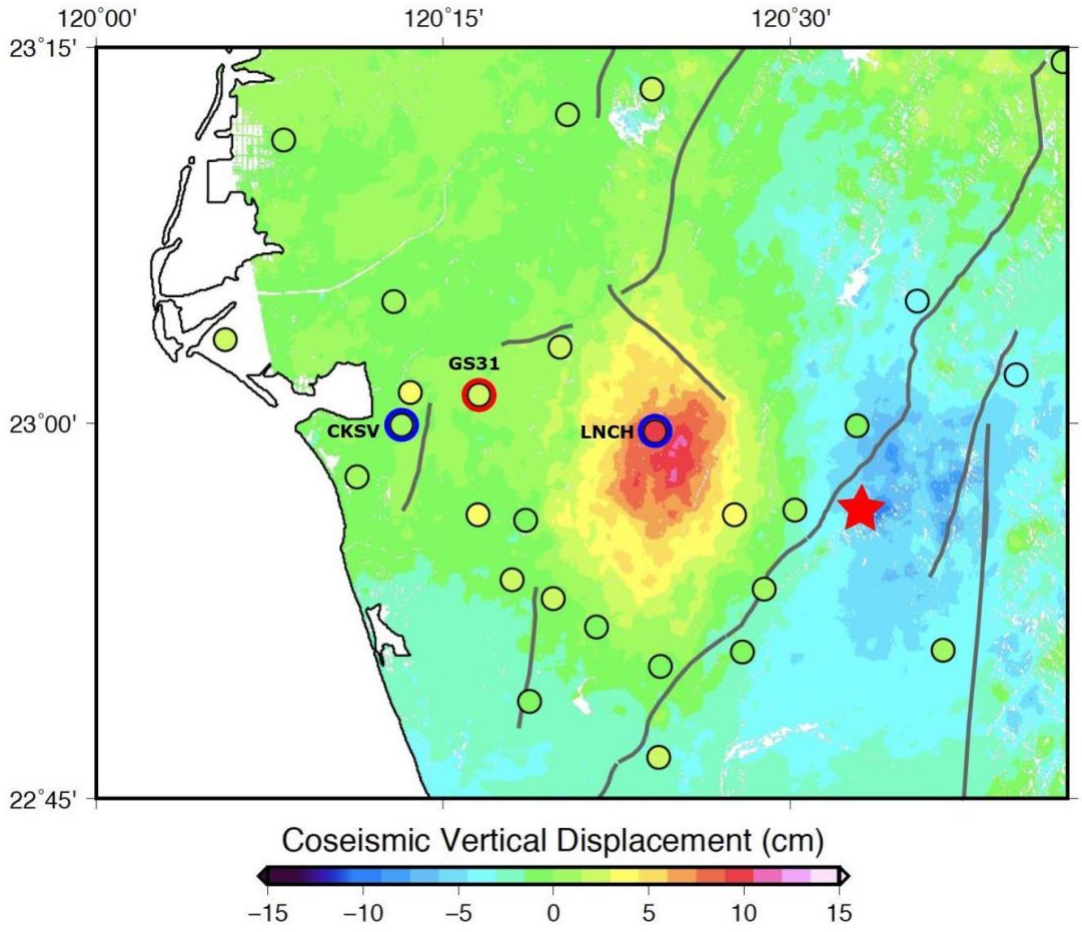

Figure 15: MeiNong earthquake coseismic vertical displacements. Background color represents InSAR vertical displacement in cm based on ascending and descending InSAR with CGPS correction. Background color showing red as uplift and blue as subsidence. GPS stations are denoted by circles with the color fill indicating uplift in cm. Dark gray lines are active faults labeled in Figure 3. Red star indicates epicenter of the MeiNong earthquake. Time series reference station GS31 is in red and target points LNCH and CKSV are in blue.

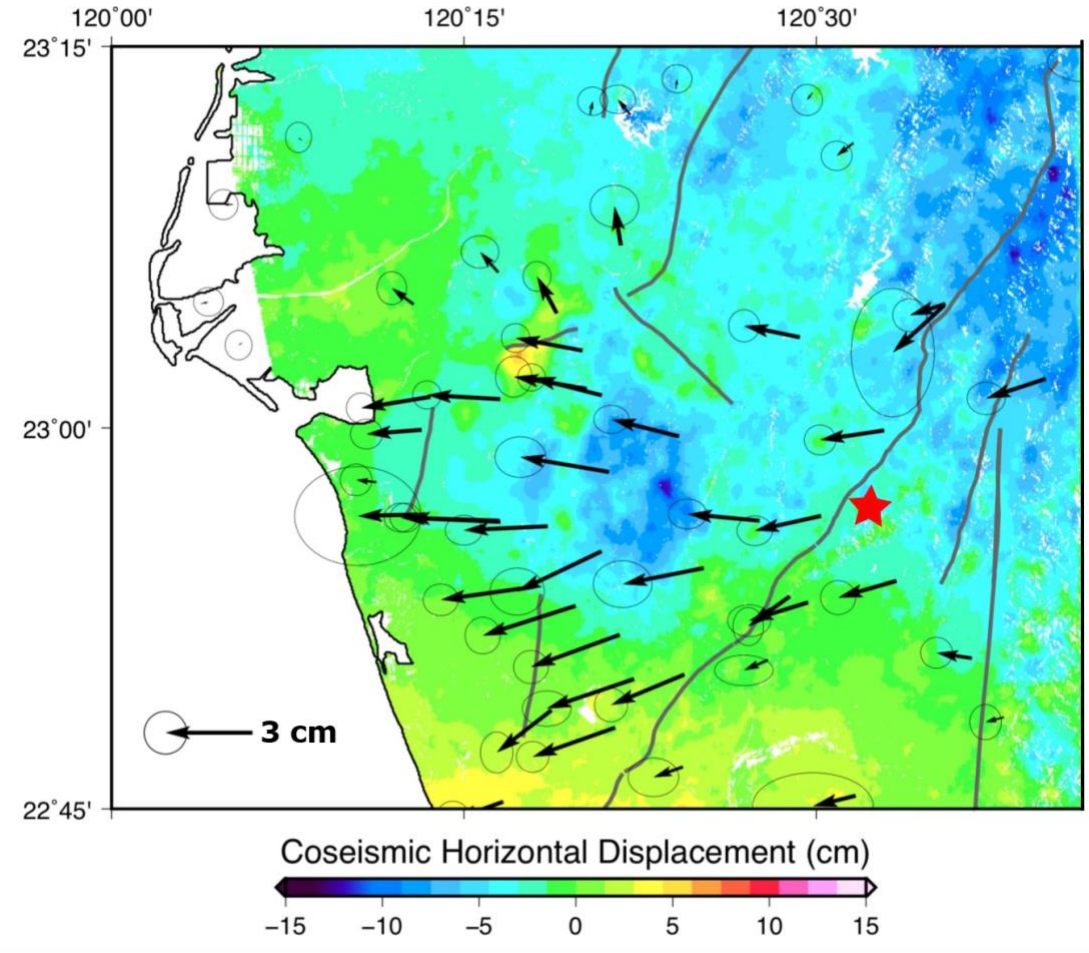

Figure 16: MeiNong earthquake coseismic horizontal displacements. InSAR (background color) shows blue color (negative) indicating westward motion and red color (positive) indicates eastward motion. GPS stations (arrows) showing coseismic horizontal velocity. Red star indicates epicenter of the MeiNong earthquake. Dark gray lines are active faults labeled in Figure 3.

In Tainan City that is ~40 km west of the epicenter, there is no clear coseismic displacement along the Houjiali fault located on the east edge of the Taiwan tableland (Figure 15). Although no significant coseismic displacement was found, there is severe building damage on the tableland possibly due to ground motion amplification in alluvial sediments and poorer construction quality of older buildings.

4.1.2 Postseismic Displacement

In the months following the earthquake, InSAR results show early postseismic transient in the area near the MeiNong epicentral as well as in the Tainan tableland that is ~30 km away. Three months following the earthquake, I observe up to ~3 cm uplift in the area of peak coseismic uplift (Figure 17). The postseismic uplift here reaches ~9 cm after 15 months. The GPS stations show continuously westward motion in the postseismic period for at least 15 months (black arrows in Figure 18). The spatial pattern of postseismic displacement (background color in Figure 18) is similar to the coseismic displacement (Figure 15), but postseismic displacement in vertical component seems to be broader than pattern in coseismic period. The postseismic uplift area is ~30 km wide and ~45 km long reaching areas further south and west of the coseismic uplift area.

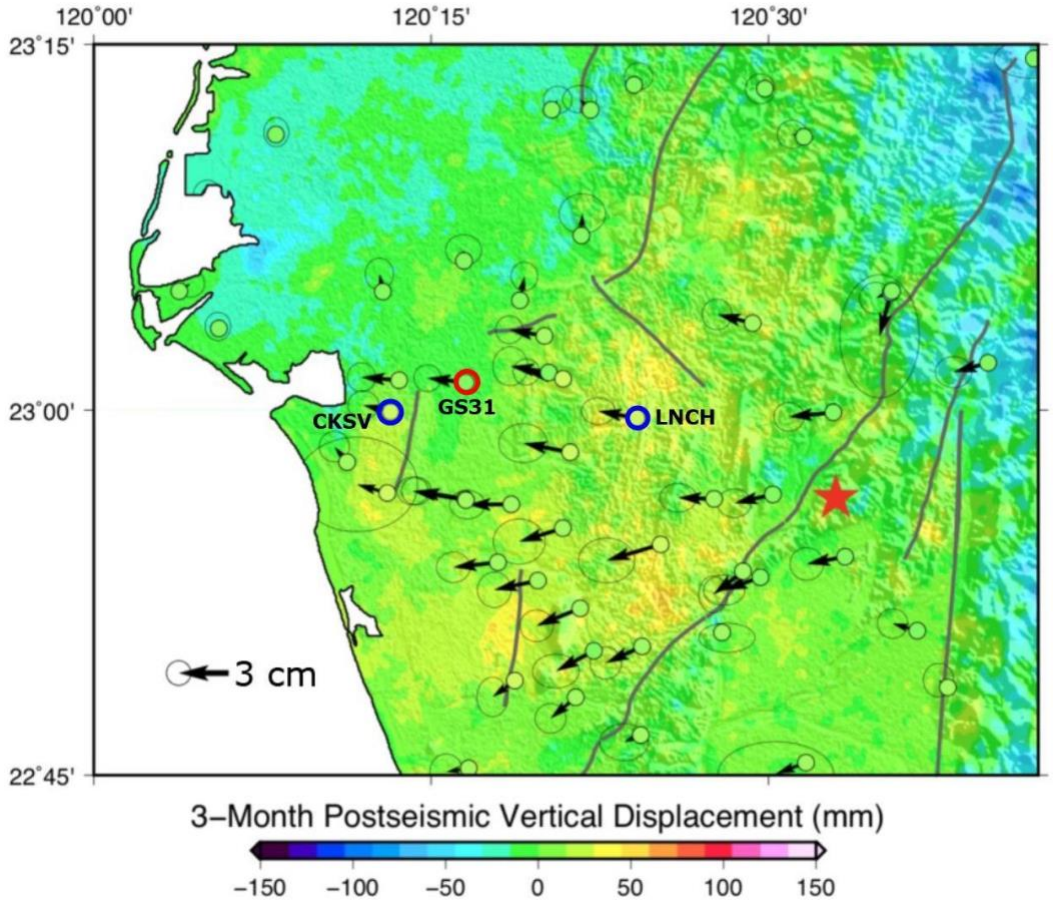

Figure 17: Map of postseismic displacements 3 months following the MeiNong earthquake. The background colors are the postseismic displacement in vertical based on ascending and descending InSAR with CGPS correction. The black circles represent CGPS stations and the color of the circles indicates vertical displacement. CGPS stations with blue circles are targets for time series (CKSV, LNCH) and the red circle is reference (GS31). The black arrows represent GPS horizontal displacement. The gray lines are major active faults labeled in Figure 3. The red star indicates the epicenter of the MeiNong earthquake.

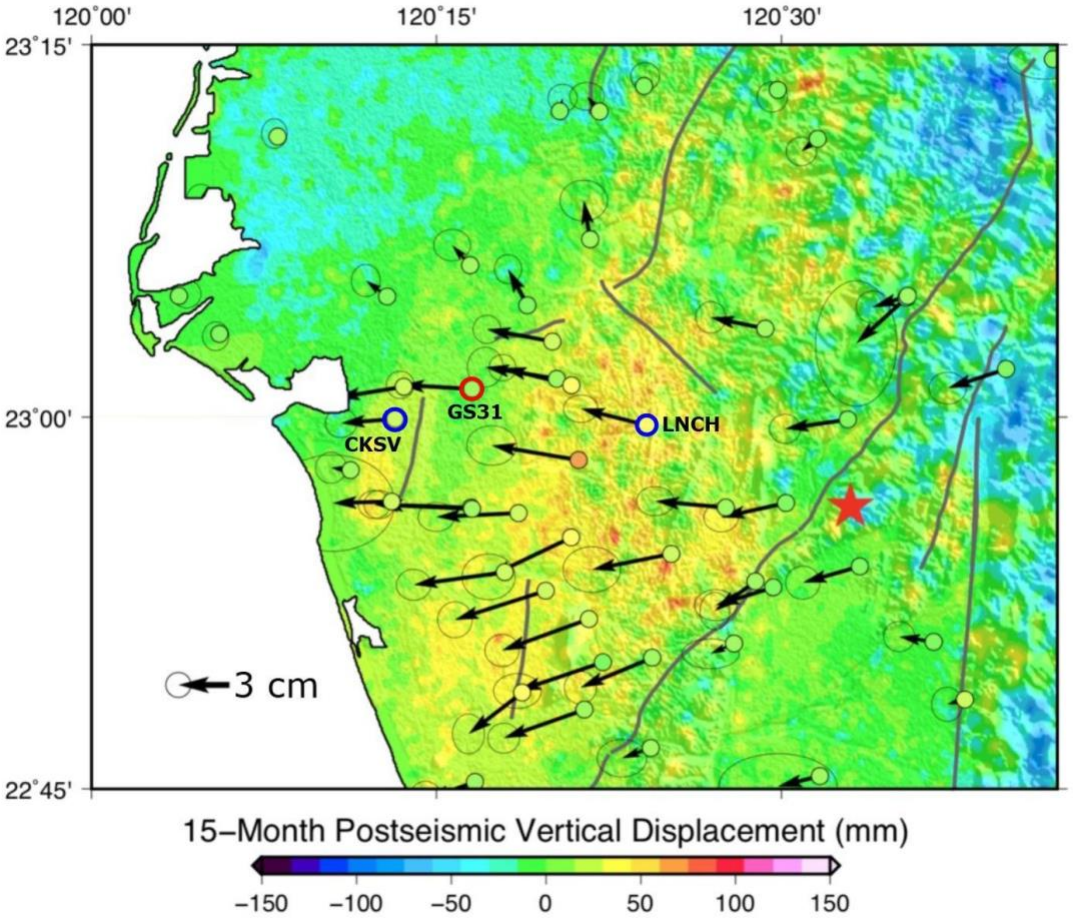

Figure 18: Map of postseismic displacements 15 months following the MeiNong earthquake. The background color is the postseismic vertical displacement in cm based on ascending and descending InSAR with CGPS correction. The black circles represent CGPS stations and the color of the circles indicates vertical displacement. CGPS stations with blue circles are targets for time series (CKSV, LNCH) and red circle is reference (GS31). The black arrows represent GPS horizontal displacement. The gray lines are major active faults labeled in Figure 3. The red star indicates the epicenter of the MeiNong earthquake.

In Tainan tableland, there is a maximum of 3 cm and 4 cm of postseismic displacement in horizontal and vertical, respectively. The amount of postseismic displacement in the first 15 months here is 4 times greater than the value in coseismic period. The spatial pattern of postseismic displacement also shows rapid change in postseismic uplift across both west and east edges of the tableland (Figure 18), which are the locations of the inferred Tainan fault on the west and the Houjiali fault on the

east sides of the Tainan tableland. Additionally, there is up to 1 cm of interseismic uplift in the Tainan tableland observed from both geodesy (*Huang et al.,* 2006; 2009) and radiocarbon dating (*Chen et al.,* 2000). The rapid interseismic and postseismic displacement in the Tainan tableland may imply shallow locking depth or variation of fault frictional properties along depth. I will provide more discussion on this topic in Chapter 6.

Comparing 3-month and 15-month images of postseismic displacement, there is gradual increase in cumulative displacement with similar spatial pattern, implying no change of postseismic mechanism (e.g. switch from afterslip-dominate to viscoelastic relaxation-dominated). The peak postseismic uplift appears to be around ~9 cm in the area where the peak coseismic uplift was observed. There are also patches of uplift surrounding some mapped active faults, such as the HsiaoKangShan fault (Number 6 in Figure 3) to the south of the peak coseismic uplift, and the TsoChen fault north of the peak coseismic uplift.

To highlight time series of surface deformation in regional scale, I select the GPS station GS31 located northeast of Tainan City as the reference point (the blue circle in Figure 17 & 18) as it is between the two targets selected. The target points (the red circles in Figure 17 & 18) are station CKSV, located on the Tainan Tableland, and station LNCH, near the peak coseismic uplift. The time series of station LNCH shows ~10 cm of coseismic uplift, following by rapid postseismic transient (Figure 19). In the horizontal time series, the earthquake caused ~3 cm westward coseismic displacement, but quickly returned to interseismic rate of ~1 cm/year without clear postseismic period.

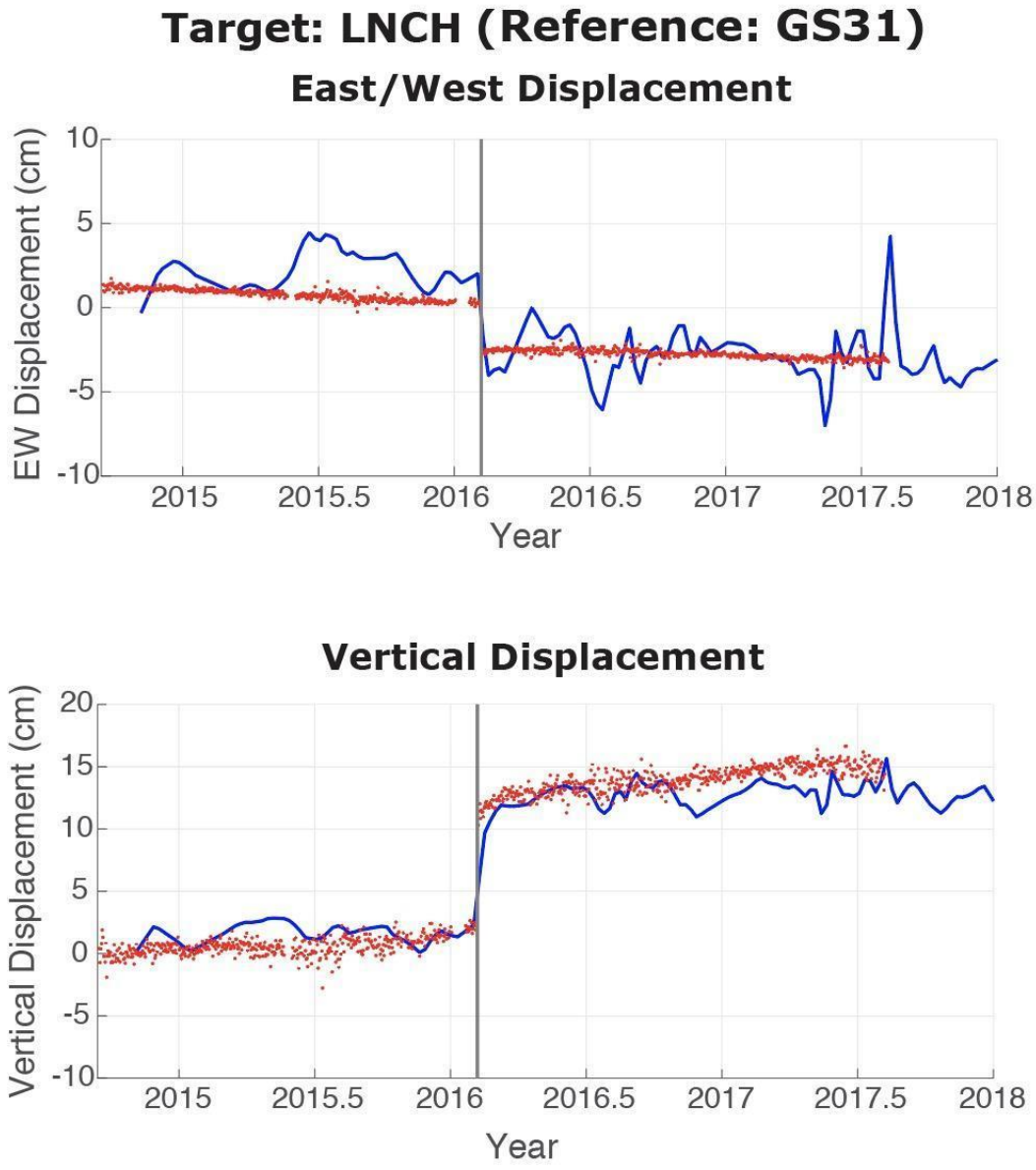

Figure 19: InSAR and GPS time series. Reference point for the time series is at GPS station GS31 (Red circle in Figure 17 & 18). Target (Blue circle in Figure 17 & 18) is within peak coseismic uplift at GPS station LNCH**.** Gray line indicates date of the 2016 MeiNong earthquake, red dots are GPS and InSAR is the blue line. EW displacements in cm are on the top with noticeable coseismic westward (negative direction) displacement at the MeiNong earthquake date line. Vertical displacement time series shows significant coseismic displacement at GPS station LNCH with ~10 cm uplift at the time of the MeiNong earthquake.

In Tainan tableland, GPS time series of station CKSV shows ~1 cm westward coseismic displacement followed by ~0.5 cm eastward postseismic displacement in the

next 6 months (Figure 20). The InSAR time series is, however, noisier than the GPS time series, possibly due to higher (cm-level) noise level of InSAR.

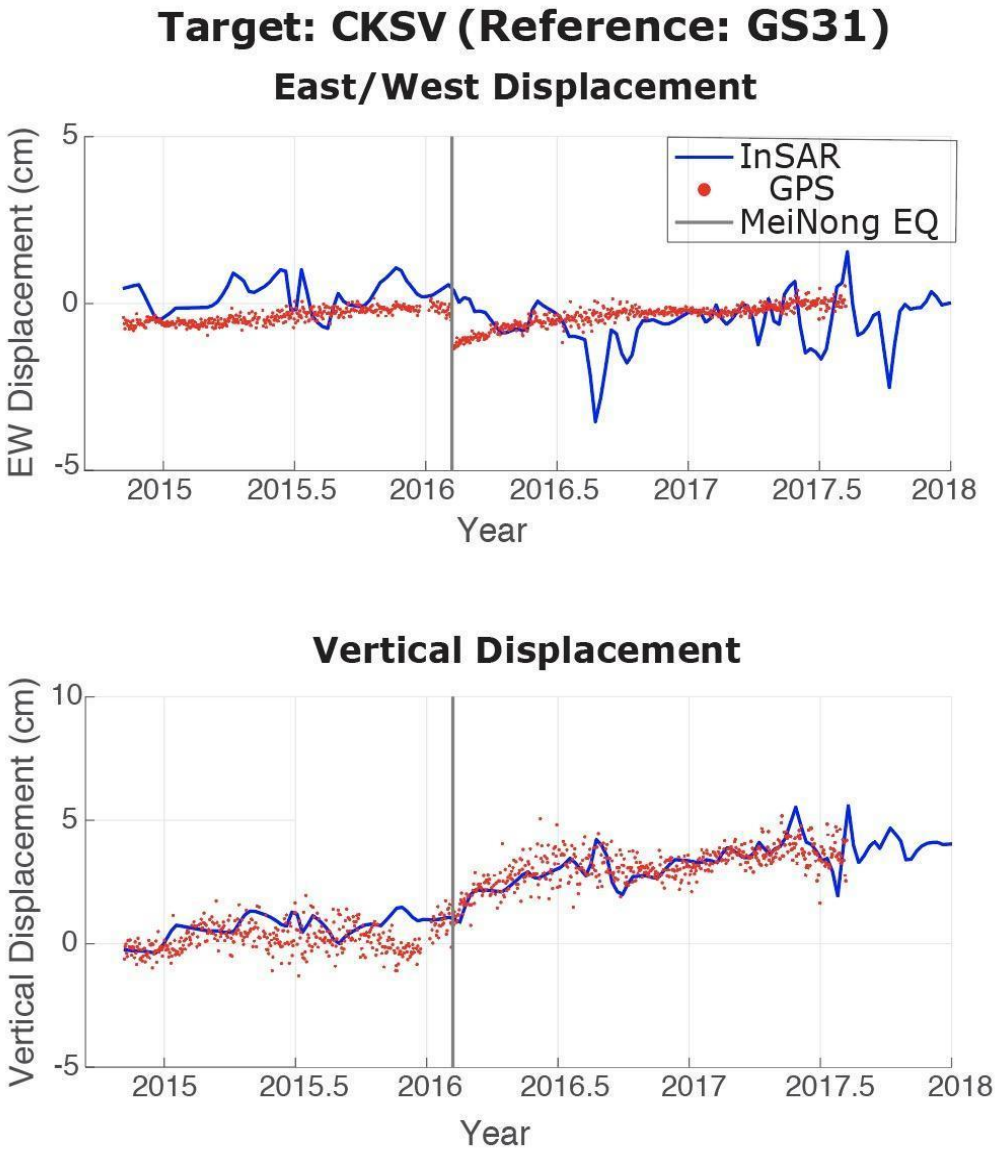

Figure 20: InSAR and GPS time series. Reference point for time series is at GPS station GS31 (Red circle in Figure 17 & 18). Target (Blue circle in Figure 17 & 18) on Tainan Tableland is at GPS station CKSV. Gray line indicates date of the 2016 MeiNong earthquake, red dots are GPS and InSAR is the blue line. EW displacements in cm are on the top with noticeable coseismic westward (negative direction) displacement at the MeiNong earthquake date line. Vertical displacement time series shows no apparent coseismic displacement at GPS station CKSV but a logarithmic postseismic transient is visible following the earthquake.

In the postseismic period, the displacement in the Tainan Tableland shows eastward movement, and the postseismic displacement gradually returns to its interseismic rate about 6 months later. Similar to InSAR time series near GPS station LNCH, I cannot clearly resolve InSAR horizontal time series due to much lower signal. In the vertical time series, no clear coseismic uplift is shown in InSAR time series, but GPS station CKSV shows plausible subsidence a few months prior to the earthquake (red dots in Figure 20). This signal became uplift ~1 month before the earthquake. However, there is a data gap in GPS right before the uplift signal, and the data gap may cause GPS network systematic adjustment. I therefore do not attempt to interpret this signal. Though no coseismic uplift was recorded, the time series shows a clear postseismic uplift of ~4 cm in the first year after the earthquake.

4.2 InSAR and GPS Inversion Results

I invert for postseismic slip distribution with using both InSAR and GPS datasets. I adopt the same fault geometry by *Huang et al.,* 2016b in the inversions. The modeled postseismic slip surrounds the main coseismic slip asperity (Purple contour in Figure 21 & 22). The postseismic slip initially appears northeast and southwest of the main coseismic slip asperity with ~30 cm of slip in the first 2 months (Figure 21). Afterslip in the early postseismic period is also concentrated down dip of the main coseismic slip and it began to appear westward along strike after the first 2 months. Afterslip shown on the shallow fault from *Huang et al.*, 2016b is in Figure A15.

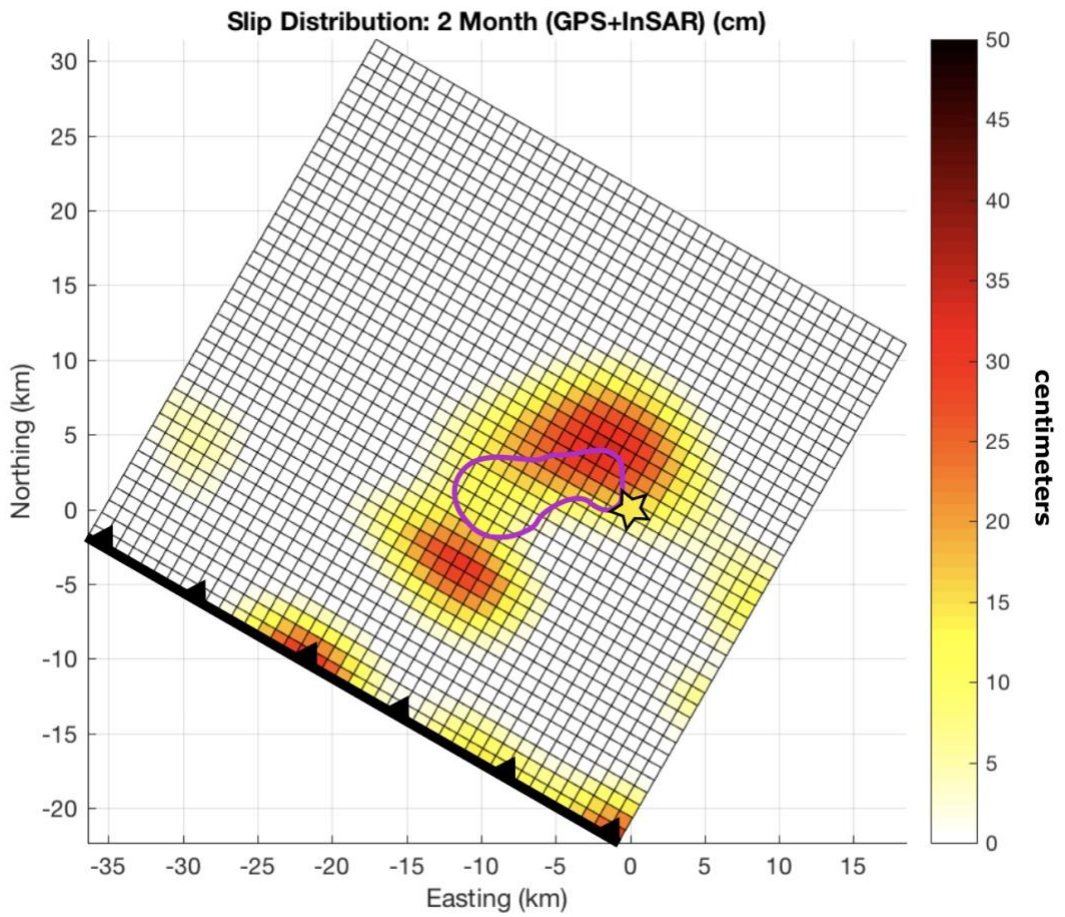

Figure 21: Cumulative afterslip on the main fault plane 2 months following the MeiNong earthquake. Yellow star indicates hypocenter and thick line represents up-dip direction of the fault. Purple outline represents peak coseismic uplift contour of 1 meter. Peak cumulative afterslip is ~30 cm.

After 15 months, the afterslip connects the north and south asperities to a slip patch directly west with ~45-50 cm cumulative slip in this area, completing the crescent shape around the coseismic slip asperity (Figure 22). The inferred 15-month cumulative afterslip moment is ~2.99×10^{25} dyne cm, equivalent to M_w 6.1. Comparing our model to the variance reduction (VR) from *Huang et al.* (2016b) of 72.2% using the same main fault geometry model, our 15-month postseismic VR is 35.3%. The lower VR is possibly due to lower amount of postseismic displacement as well as potential fault slip, either outside or shallower, than the main fault geometry used here. Additionally,

unlike coseismic inversion that is based on seismic and geodetic data constraints, afterslip is aseismic. I therefore can only rely on geodetic data for afterslip inversions. Monthly afterslip results in Figures A1-A14.

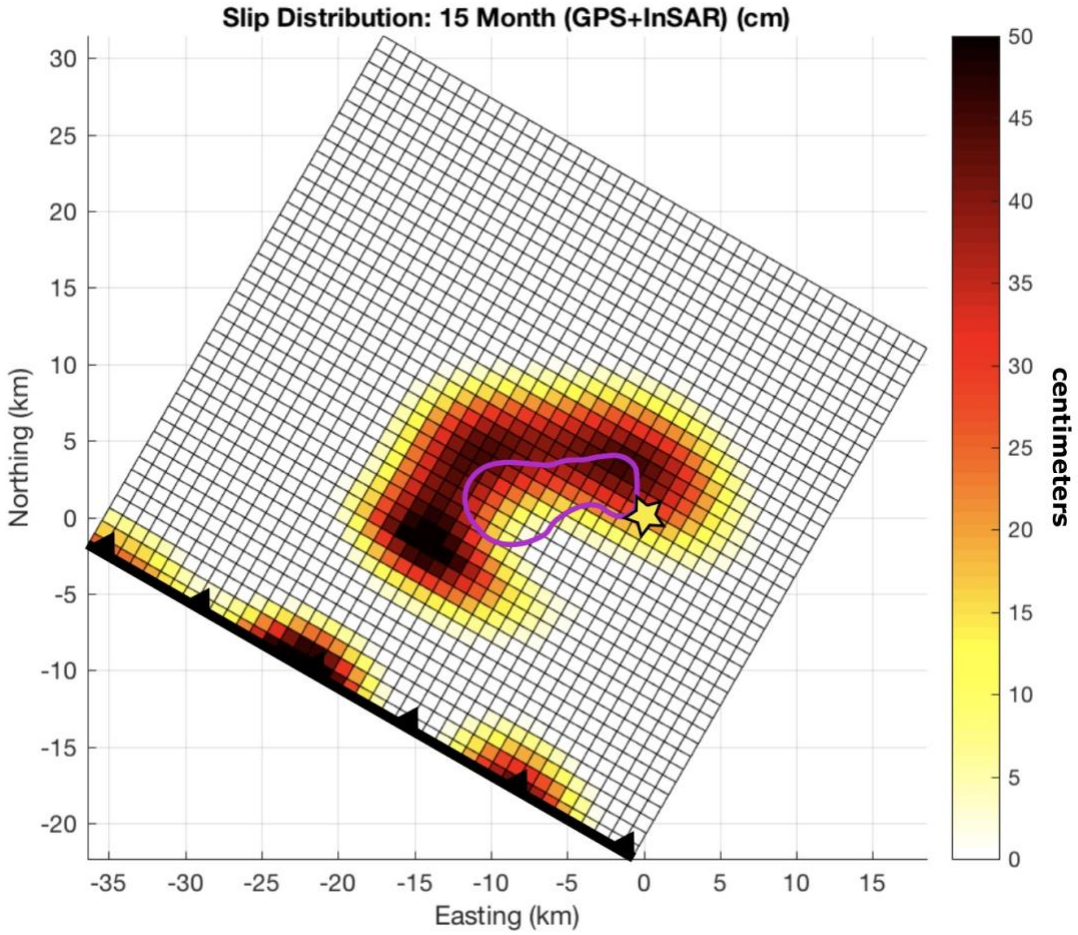

Figure 22: Cumulative afterslip on the main fault plane 15 months following the MeiNong earthquake. Red star indicates hypocenter and thick line represents up-dip direction of the fault. Purple outline represents peak coseismic uplift contour of 1 meter. Peak cumulative afterslip is ~50 cm.

4.3 Stress Driven Afterslip Results

In order to analyze how the fault responded to the coseismic stress change, I constructed a stress driven afterslip model. This model is useful in determining how the surface will respond to afterslip on the fault planes which I can then compare to

geodetic data in order to see how well the model fits the data. After calculating coseismic stress increase and converting to slip, it appears the amount of stress driven afterslip is adequate in accommodating ~50% of slip on the main fault. In the single fault model, the maximum amount of predicted afterslip distributed around the coseismic rupture area is ~0.65 meters, which is roughly half of the peak coseismic slip of ~1.2 meters (Figure 23). This model has a total seismic moment of 8.56×10^{24} dyne cm (M_w = 5.92), which is ~20% of the coseismic moment of 6.4.

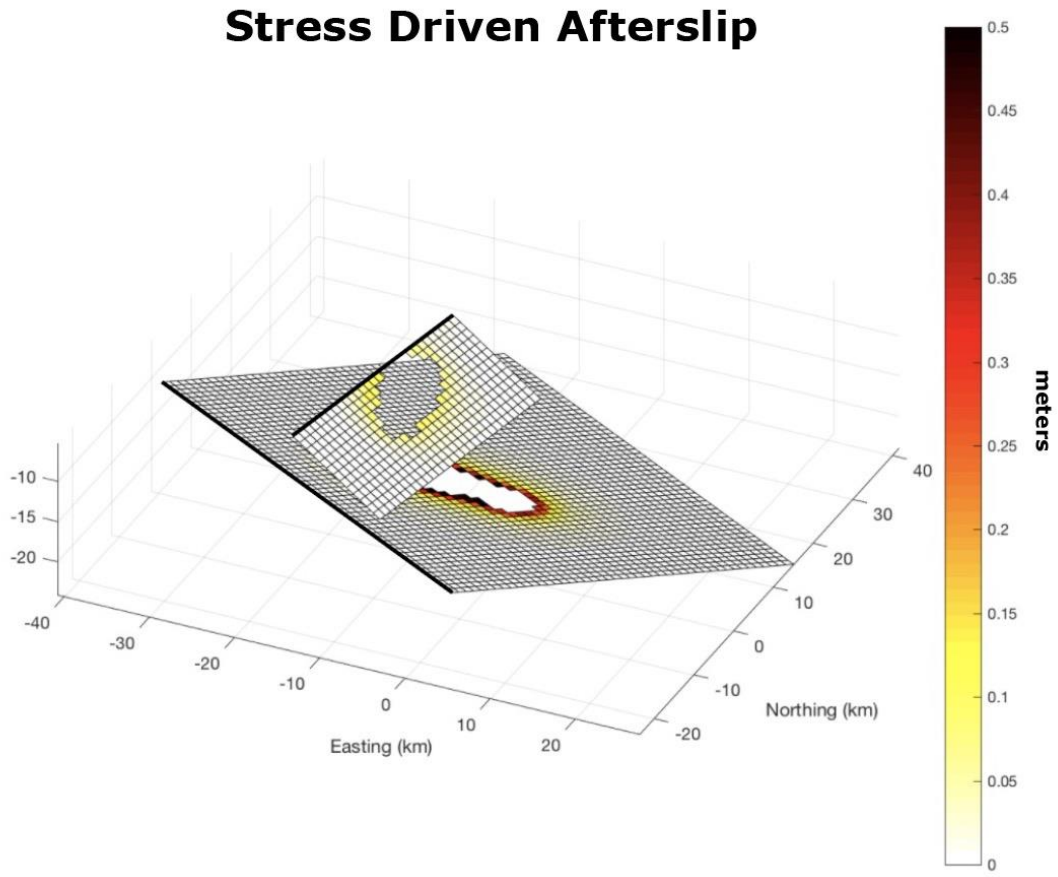

Figure 23: Stress driven afterslip with main fault and shallow fault from *Huang et al.*, 2016. Thick line on both faults represents up-dip direction. Open void on both faults represent the location of the coseismic slip asperity shown on the main fault in Figure 5.

Adding the shallow fault to the stress driven model shows a small amount of displacement around the area of coseismic slip on the shallow fault, with a peak slip of ~0.12 meters. Including the shallow fault and the detachment to the stress driven afterslip model does not significantly increase the amount of predicted surface displacement.

4.4 Aftershock Results

I use the spatiotemporal distribution of aftershocks in the months following the earthquake in order to characterize any correlations with afterslip. When observing the aftershock-to-afterslip relationship, I constrained the aftershocks to be within 5 km above and below the main fault plane. This is to account for inconsistencies in the results due to uncertainties in the relocated depths of aftershocks.

In the first two months following the earthquake, the majority of aftershocks are concentrated on the fault adjacent to the areas of afterslip (Figure 24). Aftershock locations continue to be adjacent to the areas where afterslip is present without much overlapping, and they slowly diminish in occurrence over 15 months (Figure 25). For further information see Appendix.

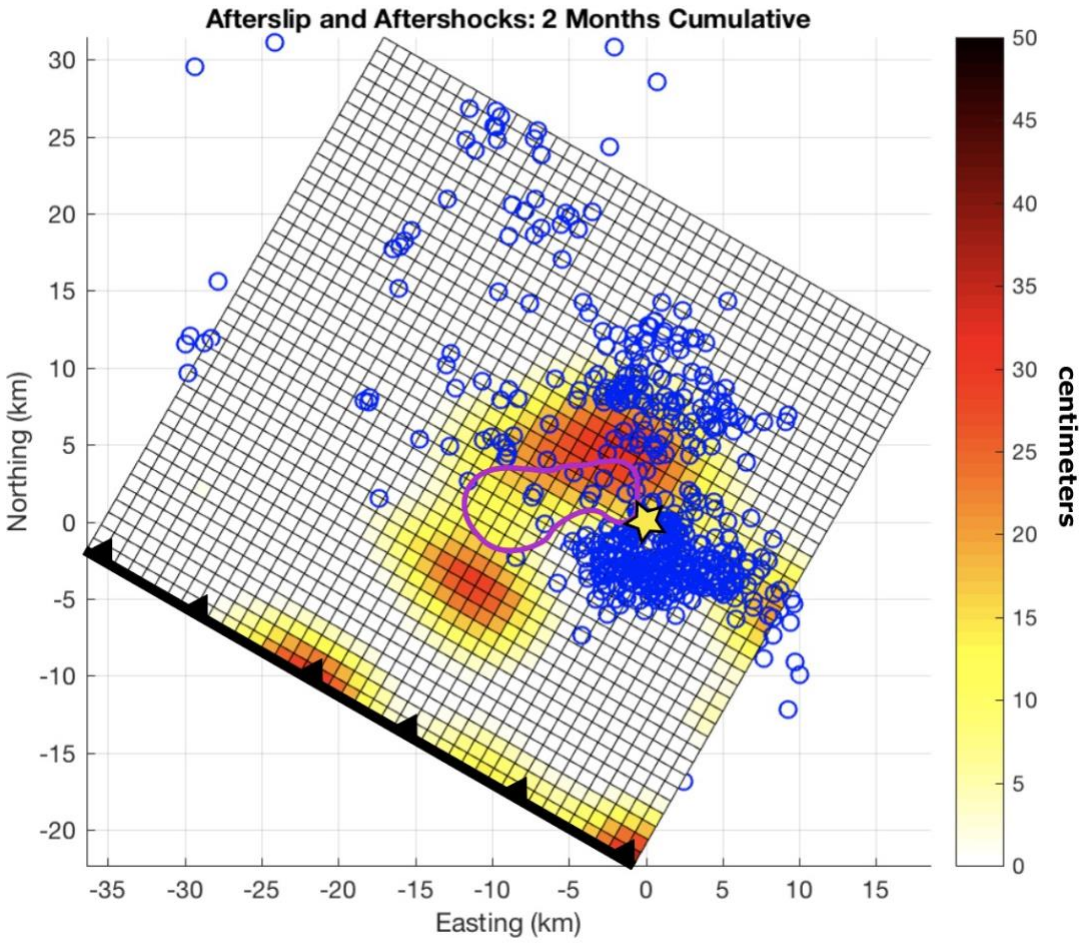

Figure 24: Cumulative afterslip and aftershock comparison 2 months following the earthquake. Blue circles represent aftershocks and yellow star represents mainshock of the MeiNong earthquake. Color on fault is 2 months of afterslip. Purple contour is coseismic slip of 1.2 meters.

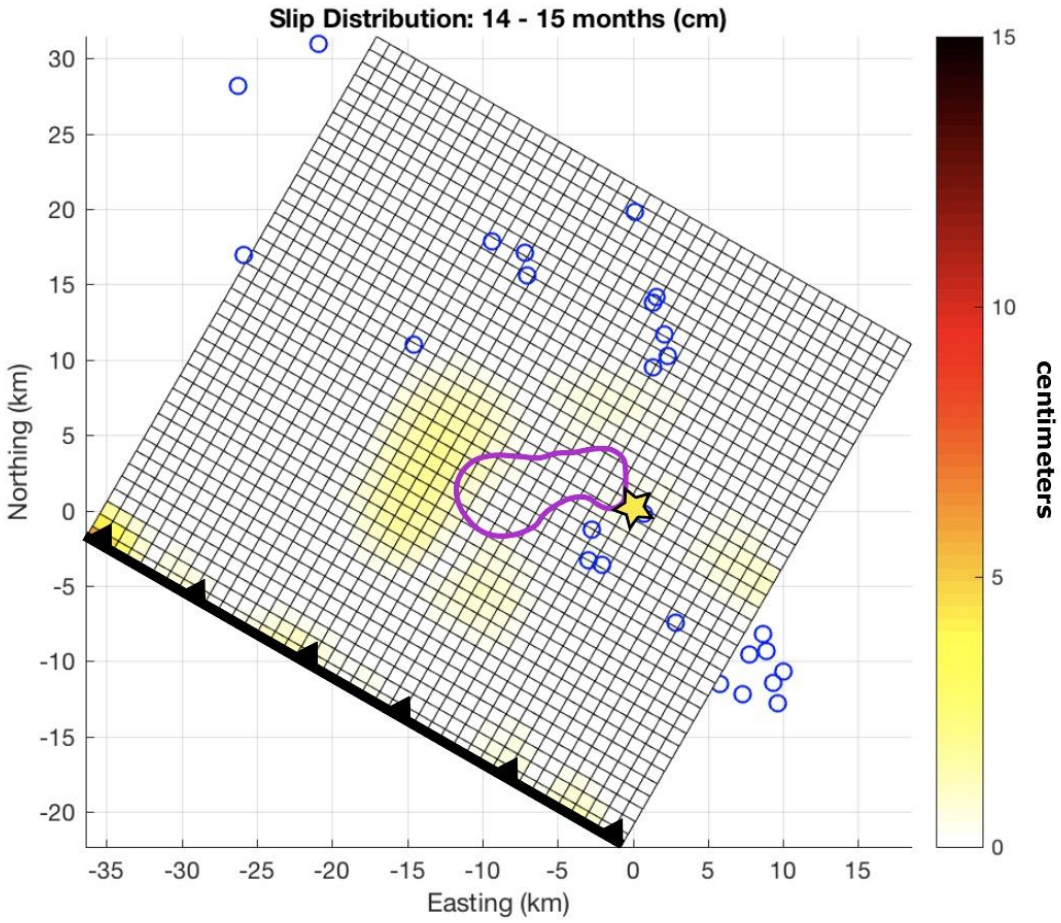

Figure 25: Difference in afterslip and aftershocks between month 14 and 15. Blue circles represent aftershocks and yellow star represents mainshock of the MeiNong earthquake. Color on fault is afterslip. Purple contour is coseismic slip of 1.2 meters.

Chapter 5: Discussion

I use inversions of combined GPS and InSAR data to observe afterslip on the main fault surface for 15 months following the MeiNong earthquake. Along with geodetic data, our analysis includes fault data and orientations from *Huang et al.*, 2016 determined using seismic and GPS data. In order to better explain our reasoning in considering afterslip as the main postseismic deformation mechanism, I compare the inversion results to a stress-driven afterslip model. Aftershock spatial distribution is analyzed in comparison to afterslip in order to see if there are any relationship between the distribution of aftershocks and afterslip on the main fault plane. In this chapter, I will first discuss geodetic observations during co- and postseismic periods, and the estimation of afterslip based on geodetic inversion and coseismic stress change. I will then focus on interpreting the relationship between afterslip and aftershocks in both space and time.

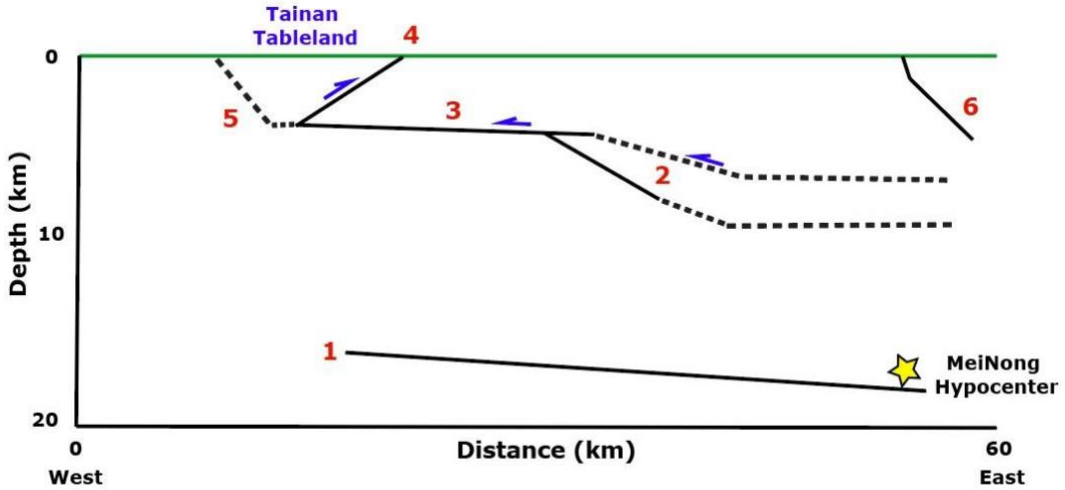

Figure 26: Southwest Taiwan multi-fault orientation. Green line represents the surface, red numbers indicate different faults known and interpreted. (1) Main fault of the 2016 Mw 6.4 MeiNong Earthquake, (2) shallow fault interpretation from *Le Béon et al.*, 2017 obtained via seismic surveys and borehole data (dashed) and fault used for inversions and forward modeling (solid) geometry from *Huang et al.*, 2016 coseismic slip inversions, (3) known Tainan Detachment, (4) Houchiali fault, (5) interpreted western Tainan Tableland fault from sharp gradient on InSAR, (6) Chishan fault. Forward modeling uses faults (1, 2, 3) and inversions use faults (1 and 2).

5.1 Geodetic Observations

The geodetic data shows the majority of coseismic uplift was located ~15 km directly west of the epicenter. The GPS station LNCH recorded the highest amount of uplift and also showed a significant increase in acceleration of westward motion. In the weeks after the earthquake, the area of peak coseismic uplift continued to slowly rise as well as areas that did not exhibit a coseismic signal (Figure 25 below of 3-month interval). Specifically, locations west and south of the earthquake in lower elevation regions began to show a postseismic response where no coseismic displacements were visible on InSAR. The interseismic horizontal motion of southwest Taiwan is ~5 cm/year shown on both GPS station LNCH and CKSV (Figure 27).

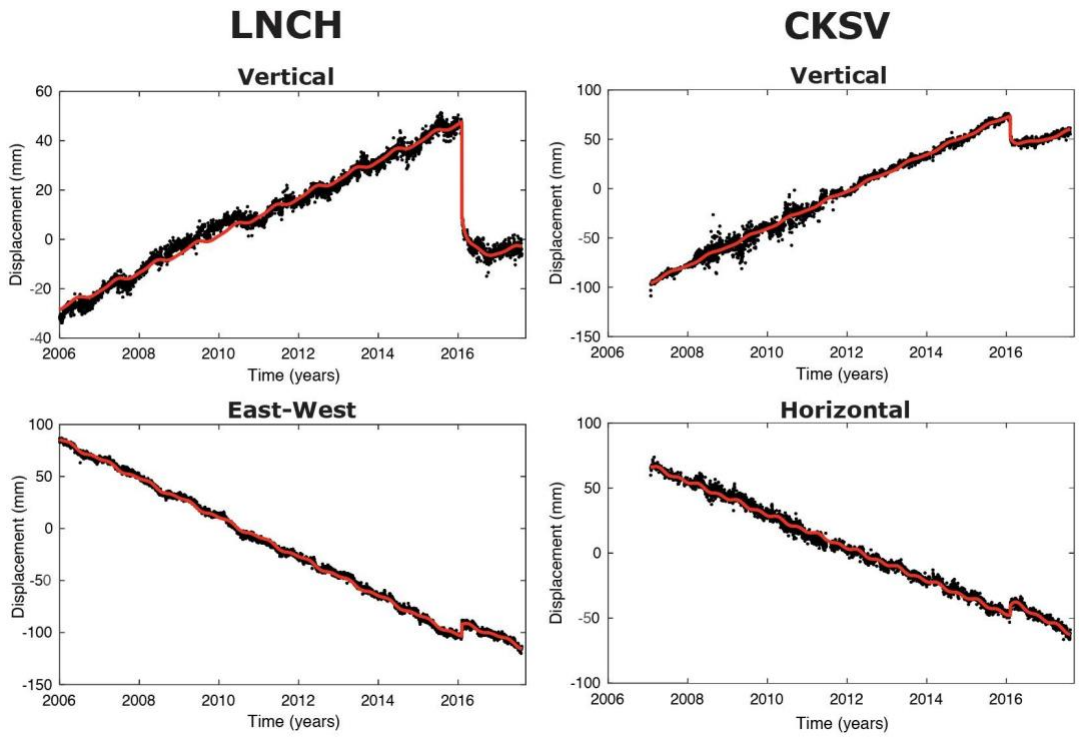

Figure 27: GPS stations LNCH and CKSV vertical and horizontal components. The linear slope in time series represent interseismic velocity, and the MeiNong earthquake occurred in 2016. The postseismic transient followed by the earthquake until it goes back to interseismic velocity.

In 3 months following the earthquake, GPS stations south of the HsinHua fault show accelerated westward movement of ~3 cm while GPS stations north of this fault show up to ~0.5 cm northward motion (Figure 27). The 15-month plot (Figure 28), continues to show an increase in westward motion of the same GPS stations totaling to a cumulative ~6 cm. The GPS stations north of the HsinHua fault continue to move northward by ~2 cm.

Some locations of the mapped active faults appear to be highlighted by uplift signals of ~2-4 cm in the 3-month geodetic observations (Figure 27). This postseismic signal continues to grow in the 15 months following the earthquake as there appear to be ~5-6 cm of uplift in the area. This uplift also appears to surround mapped active

faults (gray lines in Figure 28). If the mapped faults were already creeping, they could have begun creeping more rapidly as a response to the earthquake stress perturbation. If the faults were locked, the earthquake could have unlocked these structures and caused them to begin creeping.

5.1.1 Crustal Deformation of the Tainan Tableland during the MeiNong Earthquake

The geodetic time series shows insignificant coseismic displacement in the Tainan Tableland, yet I clearly observe a rapid postseismic transient in the first few months following the earthquake (Figure 28). A cross-section interpretation of the Tainan Tableland from *Le Béon et al.*, 2017 assumes the tableland is a shear fault-bend-fold structure, including a west dipping fault in the east side of the tableland, and a folding structure in the west side (Figure 4). The interpretation with a folding structure appears to be inconsistent with a sharp change shown in InSAR postseismic interferograms along the west edge of the tableland (Figure 29). The InSAR results suggest the west edge of Tainan Tableland is bounded by an east-dipping fault. On the east side of the Tainan tableland, the rapid change of InSAR displacement across the tableland confirms with the location of the west-dipping Houjiali fault. The InSAR time series shows observable surface deformation during all phases of the earthquake cycles, suggesting very shallow (could be less than 1 km depth) interseismic locking depth (e.g. *Huang et al.*, 2009) as well as fault zone property that is relatively influenced by change of tectonic stress (e.g. stress change due to earthquakes). Conducting a seismic survey in the future would be valuable in better differentiating between the complicated subsurface structures Tainan City is built upon.

The cross-section from 15 months of postseismic displacements shows clear uplift of the tableland. From InSAR measurements on the cross-section, there is more relative uplift across the tableland along the west side (~4 cm in 15 months) than along the east side (~2 cm in 15 months). Our inversion model does not predict uplift with short (~5-10 km) wavelength such as the observation in the Tainan tableland as the source of the model afterslip is on the deep (15-20 km depth) main MeiNong earthquake fault and is ~30 km away from the tableland.

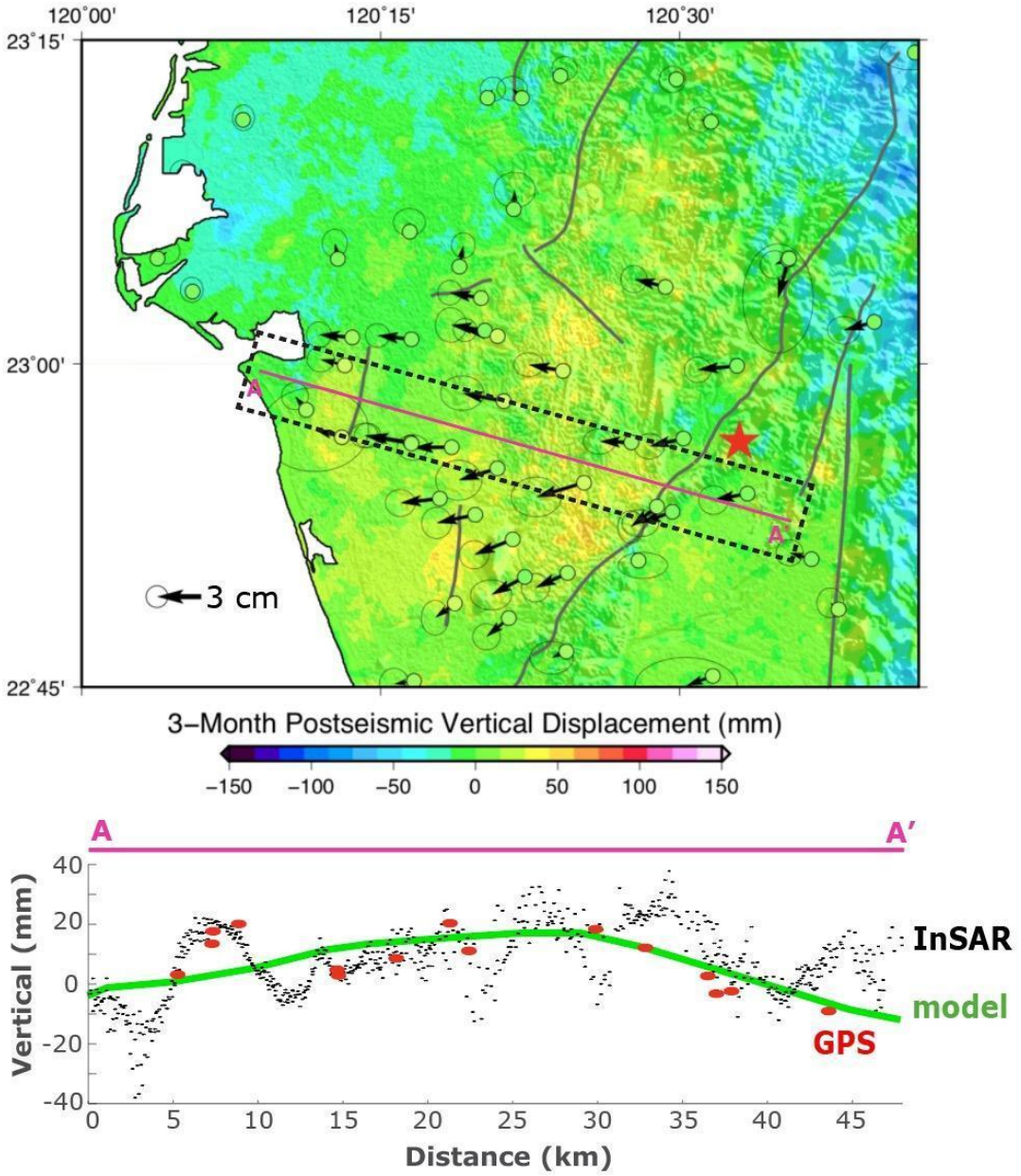

Figure 28: Postseismic surface displacements after 3 months with model fit. Background color of the map indicates InSAR vertical displacement data. Circles with arrows indicate GPS displacement in horizontal (arrows) and vertical (circle fill color). Gray lines indicate active faults labeled in Figure 3. Magenta line represents the cross section below the map of A and A'. Black dashed box represents area covered and GPS stations included in the cross section. Cross section shown below is distance in km and vertical displacement in mm. Black dots represent InSAR vertical points and red dots indicate GPS vertical motion. Green line is the model surface displacement from slip inversions.

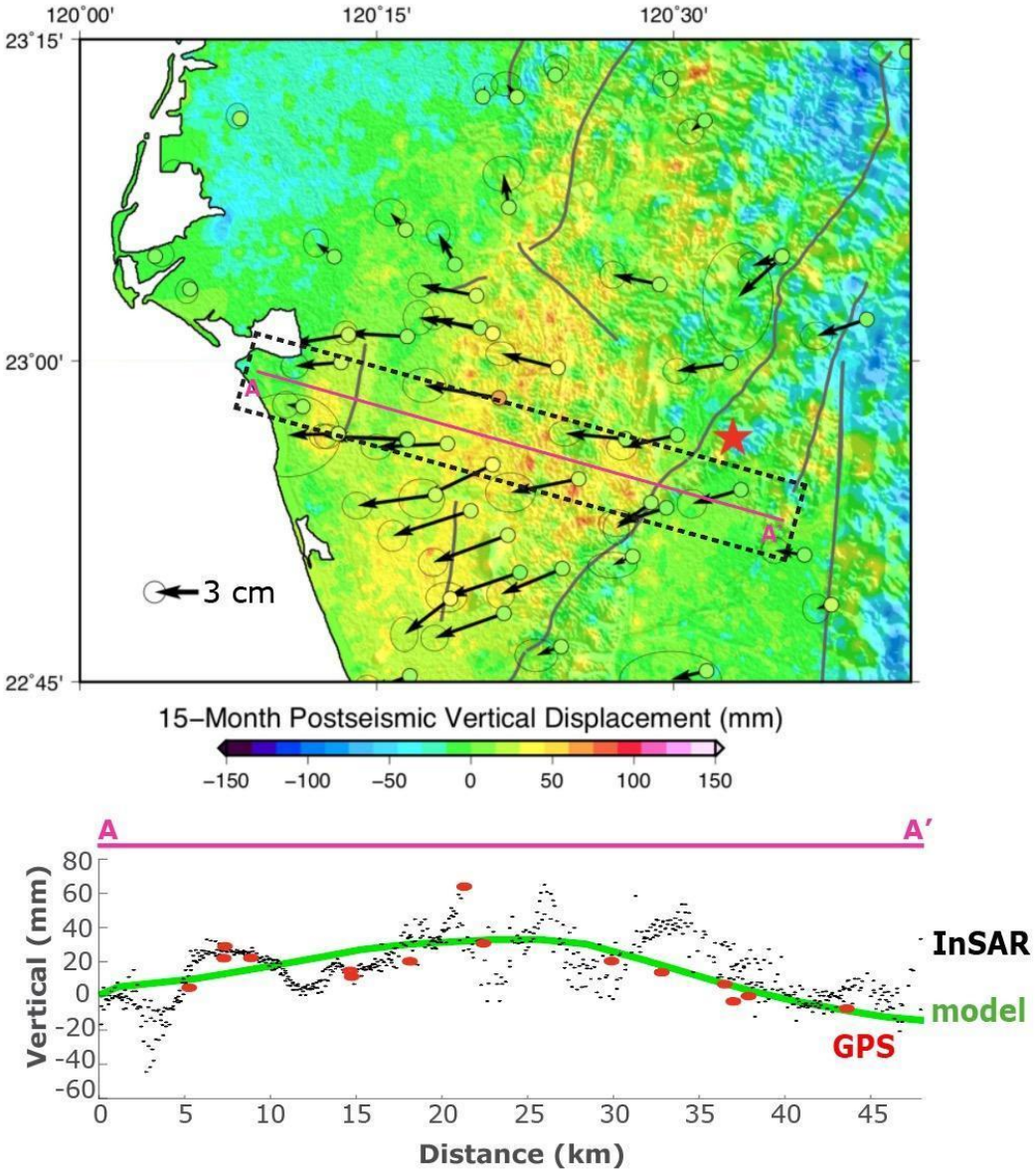

Figure 29: Postseismic surface displacements after 15 months with model fit. Background color of the map indicates InSAR vertical displacement data. Circles with arrows indicate GPS displacement in horizontal (arrows) and vertical (circle fill color). Gray lines indicate active faults labeled in Figure 3. Magenta cross section line A and A' shown below with distance in km and vertical displacement in mm. Black dots represent InSAR vertical points and red dots indicate GPS stations. Green line is model fit of slip inversions.

From analyzing east-west transects across the region of postseismic displacement 3 and 15 months following the MeiNong earthquake (line A-A' in Figures 28 & 29), I find that afterslip solely from the main fault (the green curve in Figures 28

& 29) is unable to predict the short wavelength signals as shown by InSAR (the black dots in A-A' cross-section of Figures 28 & 29). These short wavelength signals suggest the existence of shallow faults (likely above the main detachment) triggered by the MeiNong coseismic stress change. Similar to the Houjiali fault, slip along these shallow fault structures was triggered by the MeiNong earthquake, even though there is no significant interseismic creep found along the faults. Improved understanding of the structures of southwest Taiwan are needed to fully explain geodetic measurements. However, interpretation of these shallow structures is not the purpose of this study and will be left for future investigation.

5.2 Afterslip Inversion and Model Misfit

From the combined GPS and InSAR afterslip inversions, afterslip appears around the main coseismic slip asperity, with the majority of afterslip migrating on the fault in the south westward direction (Figure 22). These results can be interpreted by a mixture of velocity weakening and strengthening frictional material located on the fault plane, as shown in the schematic model in Figure 1a. Characteristics such as the non-uniform features of fault surfaces can play a role in determining the velocity weakening and velocity strengthening portions.

Comparing both GPS and InSAR fit to our predicted surface displacements from the preferred slip model allow us to observe how well our model explains the surface response. A cross-section of both 3-month and 15-month of GPS and InSAR data is taken to demonstrate fit between the InSAR pixel movement and the GPS station movement. In the 3-month cross section, there is a good fit between the locations of the GPS stations (red circles in cross section A-A' of Figures 27 & 28) and InSAR

pixels (black dots in cross section A-A' of Figures 27 & 28). There are series of oscillations with ~10 km wavelength in InSAR data indicating the uplift and subsidence of small-scale features across the region. The short-wavelength features shown in the cross section could be indicative of shallow active faults that were previously unmapped.

When comparing observed (blue arrows in Figure 30) and predicted (purple arrows in Figure 30) horizontal surface displacements from the afterslip model, there is greater misfit outside of the main fault outline (black box in Figure 30). The misfit here indicates that our preferred slip model cannot predict geodetic observations in the far-field, especially south of the main fault, which suggests the presence shallow fault structures. These structures south of the main fault may have been triggered to creep following the earthquake.

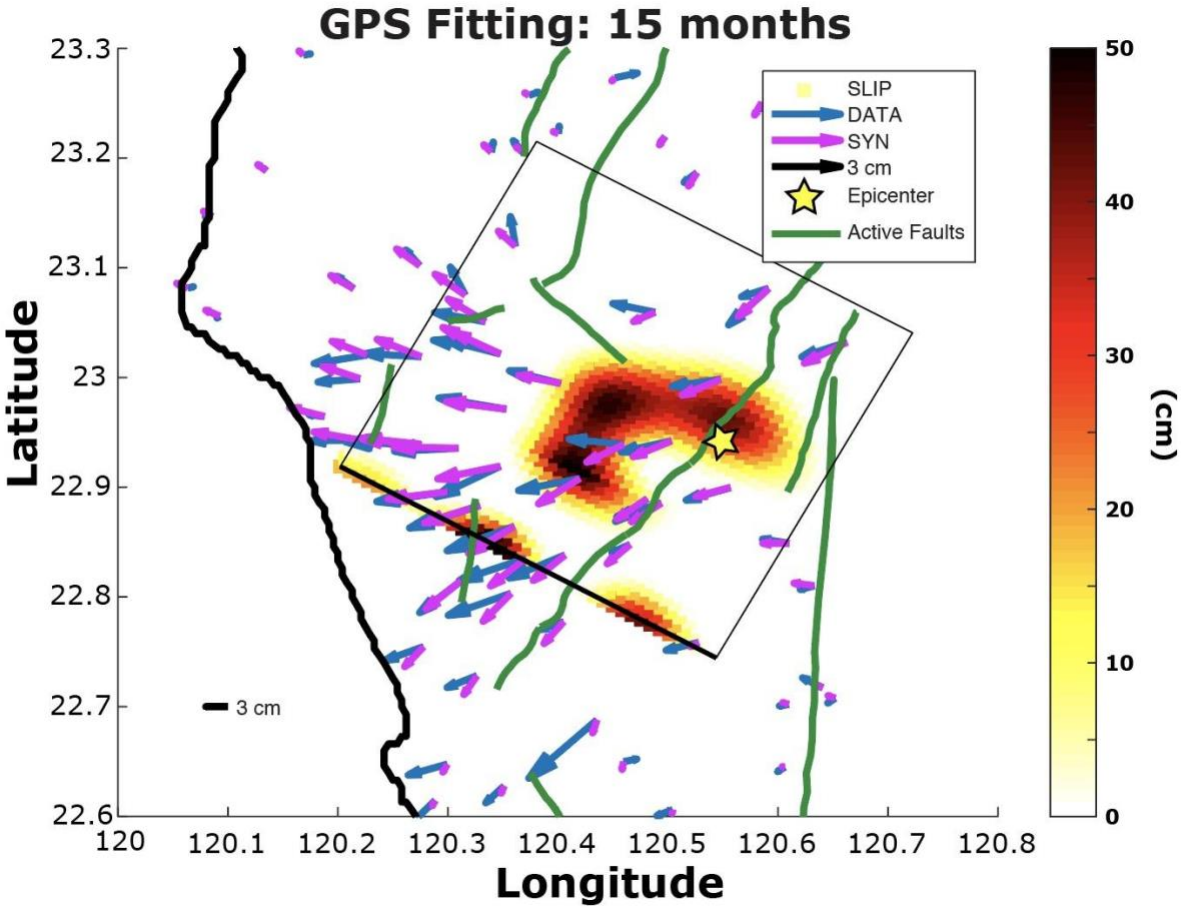

Figure 30: Misfit between GPS data (blue arrows) and predicted surface data from joint inversions (purple arrows) with 1 cm scale bar 15 months following the MeiNong earthquake. Fault outline has thick bar indicating up dip direction. Mapped active faults are indicated by green lines (labeled in Figure 3) and the epicenter is the yellow star. Modeled slip on the fault outline is in cm.

To evaluate model misfit, I use the slip model to forward predict surface displacements in order to highlight the differences between observed InSAR data and modeled synthetic data. The residual plot demonstrating fitting InSAR data is shown in Figure 29 along with data and synthetic. The model fit projected on the surface above the main fault plane is also relatively good compared to the areas south and west of the fault plane (black rectangle in Figures 30 & 31). Estimating the uncertainty of the

model by observing the residual plots in ascending and descending indicates our model does not account for the areas surrounding the main fault.

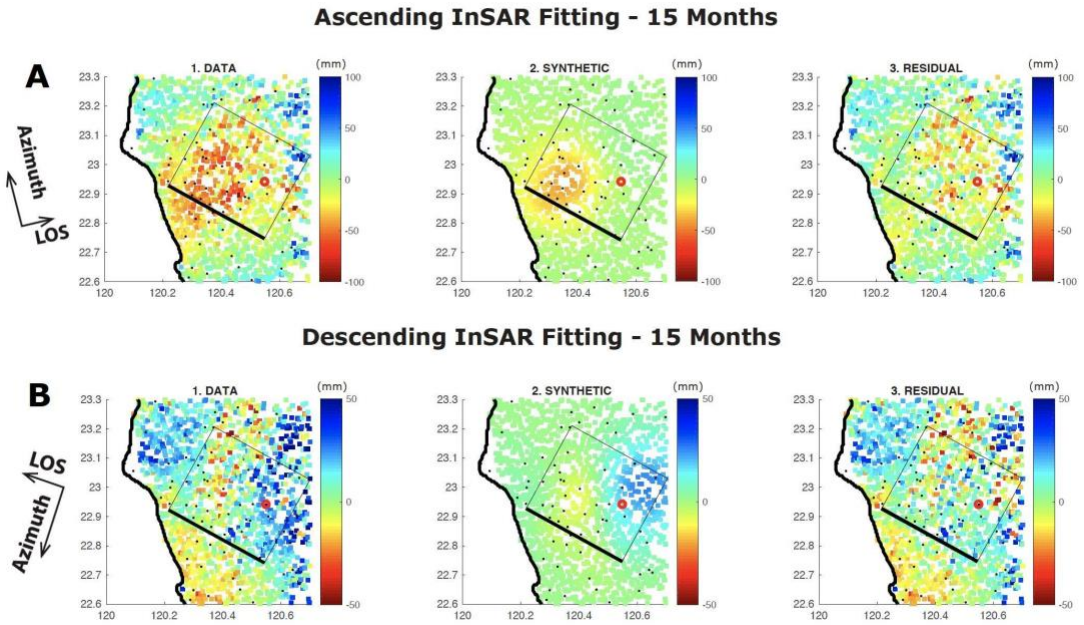

Figure 31: 15 months of ascending (A) and descending (B) GPS and InSAR data to afterslip inversion model fit. Red circle indicates epicenter location. Outline of fault plane is shown on all plots. Background color is InSAR and GPS data (1), synthetic data from inversions (2) and the residual between data and synthetic (3). In ascending (A), red indicates movement towards the satellite line of sight (LOS) and blue indicates movement away from LOS. In descending (B) red indicates movement towards LOS and blue indicates movement away from LOS.

When observing data from the ascending and descending satellites, when the colors of an area are the same in both ascending and descending images (i.e. positive or negative LOS for both ascending and descending images), the area is dominated by vertical motion. When the colors are different in the same area for ascending and descending, horizontal motion is the dominant movement. Northeast of the main fault plane the color differs in both ascending and descending (Figure 31, A & B "1. Data"), implying a horizontal-dominated area. South of the main fault, the color is similar in

both ascending and descending data plots (Figure 31 A1 & B1), implying an area dominated by vertical motion.

5.3 Stress Driven Afterslip and Misfit

For the stress-driven afterslip models, I first calculate stress on the main fault in order to observe predicted surface displacements as a result of the earthquake coseismic rupture. Since the shallower fault proposed by *Huang et al.* (2016b) was triggered by the earthquake, I also calculate stress driven afterslip on this fault. With the addition of the shallow 5-10 km fault the max slip on this fault is ~12 cm (Figure 32). In adding the two shallow structures, the 5-10 km fault and the Tainan Detachment, there are no significant increase in surface predictions from the afterslip model.

Figure 32: Shallow fault only in two views with calculated stress driven afterslip. Thick line represents up-dip direction. Peak afterslip is ~0.13 meters, represented by clear space.

After plotting predicted surface displacements from the stress driven afterslip model alongside GPS measurements from following the earthquake, I notice that there are some inconsistencies and discrepancies between geodetic observations and stress driven afterslip predicted surface displacement. I first plot the horizontal motion (Figure 33) and notice that south of the main fault there is still a high amount of misfit, similar to our geodetic afterslip inversions. The horizontal surface prediction only demonstrates a good fit to geodetic surface observations above the main fault outline. Both the model and data indicate westward motion following the earthquake, but the amount of westward motion from the stress driven model is not enough to account for all observed horizontal movement. The areas of large misfit indicate the need for additional explanations of surface motion other than just afterslip from the earthquake.

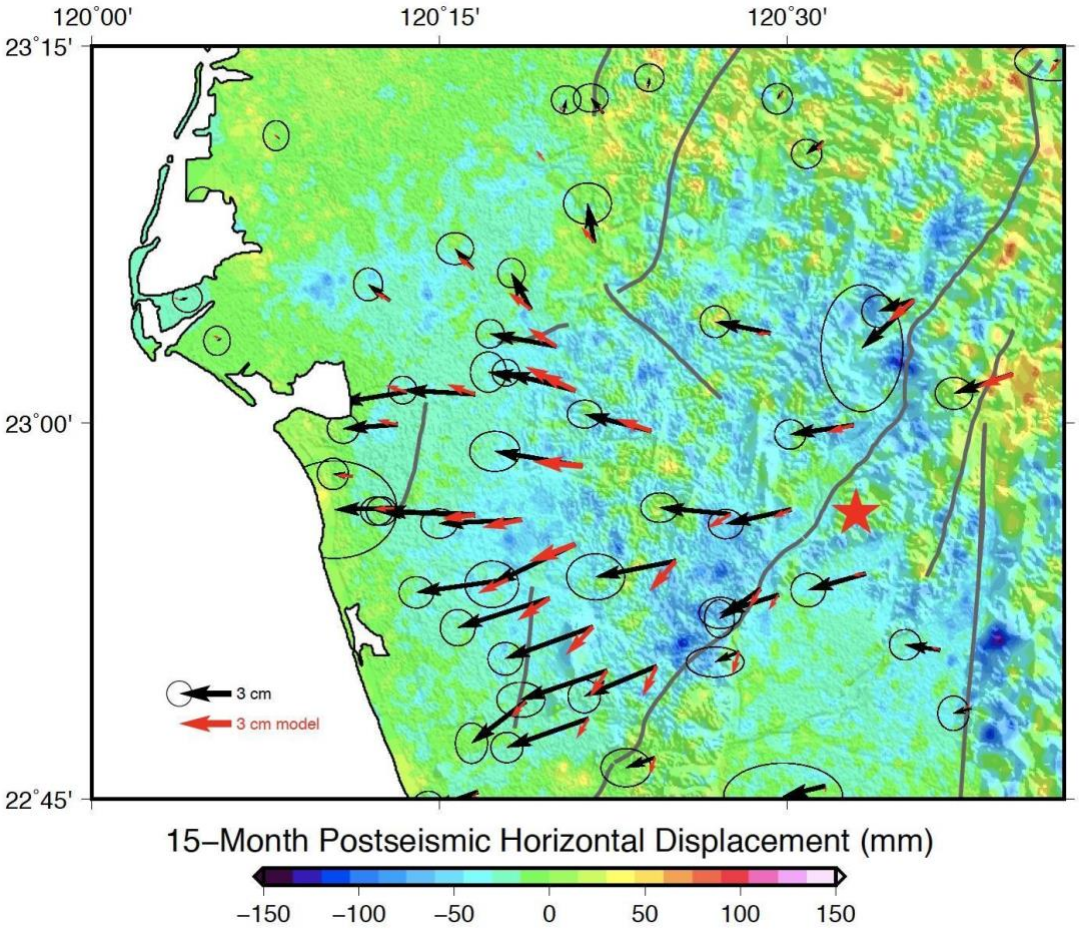

Figure 33: GPS and predicted horizontal surface motion from stress-driven afterslip model. Black arrows indicate GPS data with the uncertainty within the circle. Red arrows indicate surface response from calculated stress driven afterslip the earthquake fault. Background color indicates InSAR postseismic horizontal motion.

The amount of modeled vertical uplift from the stress driven afterslip model is also not enough to explain all of the uplift shown from geodetic measurements. GPS stations in Figure 34 show significantly more vertical uplift than the model, indicating that all of the postseismic uplift is not originating from afterslip alone.

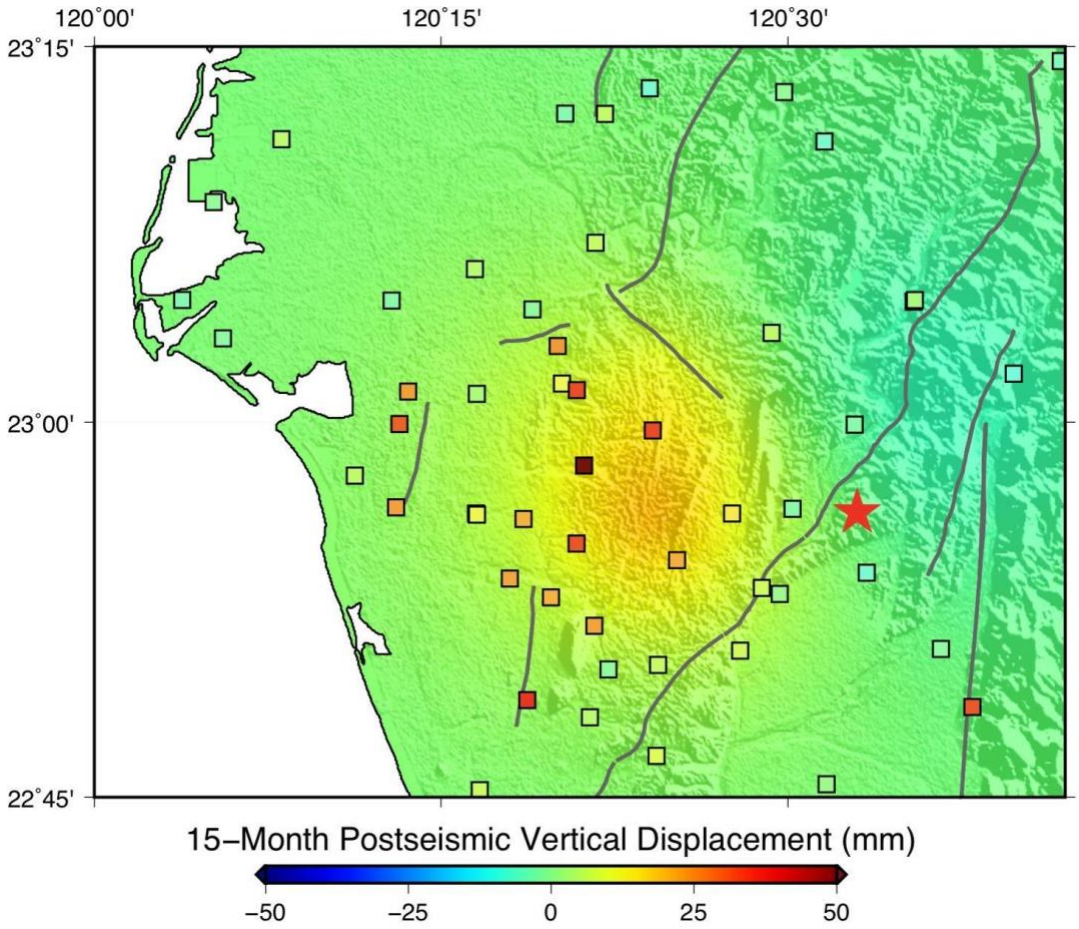

Figure 34: Vertical surface prediction from stress driven afterslip model and GPS stations. GPS stations are black squares with the color indicating amount of vertical uplift. Color in the background indicates anticipated surface uplift from stress driven afterslip.

Since the afterslip model shows no significant coseismic stress change at the shallower depths, it is likely that there are additional postseismic processes occurring at these depths that were previously not included in our model. Similar to the discussion in Section 5.1.1, this could be indicative of further triggered slip along very shallow structures above the 5 - 10 km east dipping shallower fault used in both our stress driven afterslip and inversion model. If there are shallow faults locked closer to the surface that were critically stressed during the interseismic period, the coseismic stress change

could have unlocked these faults slowly over time following the earthquake. If this is the case, I will not be able to observe these smaller features using forward modeling.

Some uncertainties in our model generated using Coulomb may originate from the unknown distribution of receiver faults and the assumption of spatial homogeneity of the material. There is also incalculable small-scale slip variability that can lead to strong stress heterogeneities close to the source fault. Fluids and shallow hydrologic contributions could also cause the unexplained postseismic uplift to occur. Why significant afterslip is observed from inversions of geodetic data but not apparent from the Coulomb stress model still remains ambiguous.

Section 5.4 Aftershock Distribution and Relationship to Afterslip

To further investigate the relationship between aftershocks and afterslip, I compare the spatiotemporal behavior of aftershocks and afterslip within the area of the main earthquake fault. Aftershocks occur near or on the mainshock fault plane for years following events near plate boundaries. Though the relationship between postseismic deformation and aftershocks is not clearly understood, there are strong spatial-temporal correlations between them found in a number of earthquake events (*Perfettini and Avouac,* 2007). It is assumed that if both aftershocks and afterslip are driven by the same process, they should exhibit a similar decay rate in time. This analysis results in an observable linear trend between both total afterslip moment and cumulative number of aftershocks (Figure 35). This observation can indicate that the triggering processes of the aftershocks could be mechanically linked to afterslip (*Lange et al*., 2014).

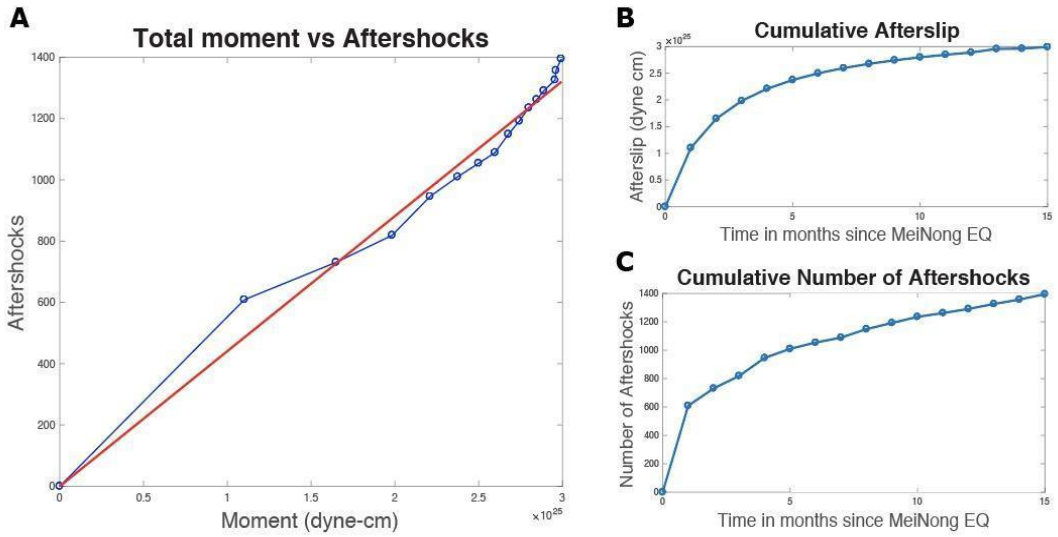

Figure 35: Total moment in dyne-cm vs cumulative number of aftershocks > M_w 1.0 (A). Fitting using least squares method. Red line indicates fit, blue line indicates actual data. Cumulative afterslip 15 months following the MeiNong earthquake (B) and cumulative number of aftershocks following the earthquake (C) with interseismic contribution removed.

In the postseismic time series, both cumulative afterslip moment and number of aftershocks show a logarithmic decay in time (Figure 35B-C). To further compare the temporal decay rate between afterslip and aftershocks, I sample the cumulative number of aftershocks for each month and plot with the cumulative monthly afterslip moment (Figure 35C). Together they can be fitted with a line using least square (the red line in Figure 35A), therefore demonstrating a linear decay rate of both afterslip and aftershocks.

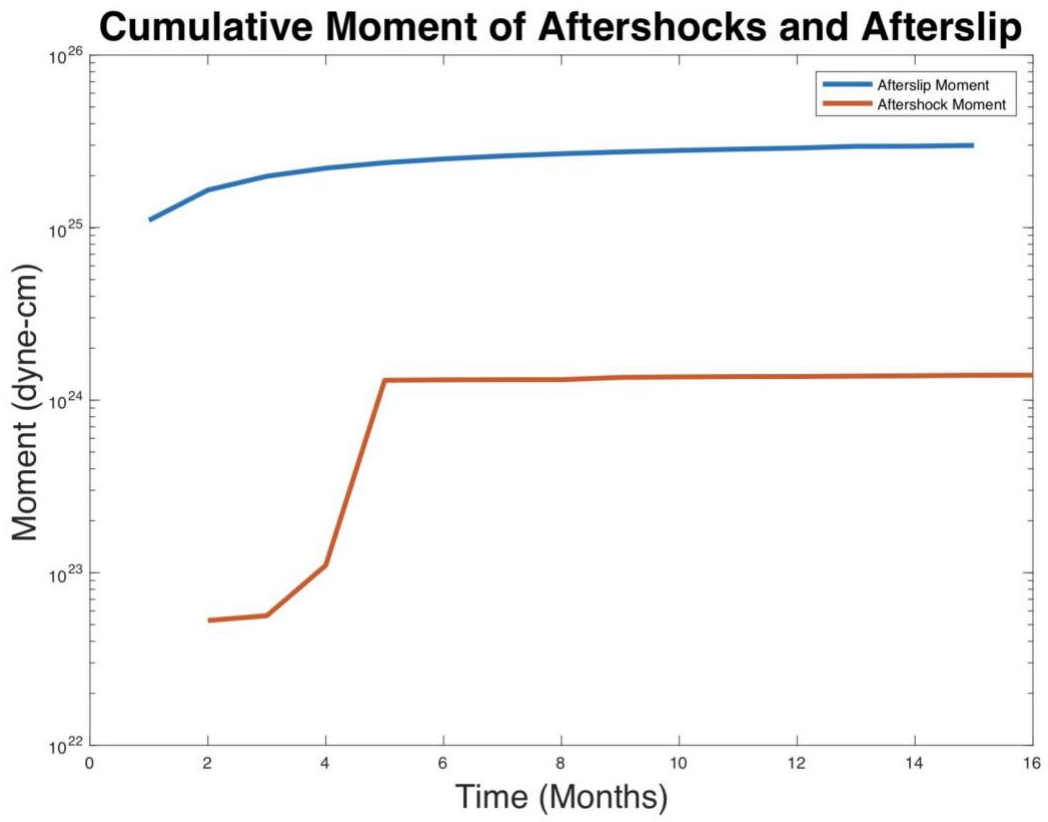

Figure 36: Cumulative moment of aftershocks (orange line) and cumulative moment of afterslip (blue line) comparison over 15 months. Moment is in units of dyne-cm.

I also compare the cumulative moment of both afterslip and aftershocks (Figure 36) in order to observe the time series trend. By the 14th month, the cumulative aftershock moment is only 8% of the cumulative afterslip moment. The large increase in moment of aftershock between month 4 and 5 is due to the greatest M_w 5.1 aftershock. This similar spatial decay rate of afterslip and aftershocks may indicate the location of afterslip may have a direct influence on the location of aftershock occurrence. Our inversion data and relocation of aftershocks indicate that there is also a spatial correlation between postseismic stress release and aftershock location (Figure 37).

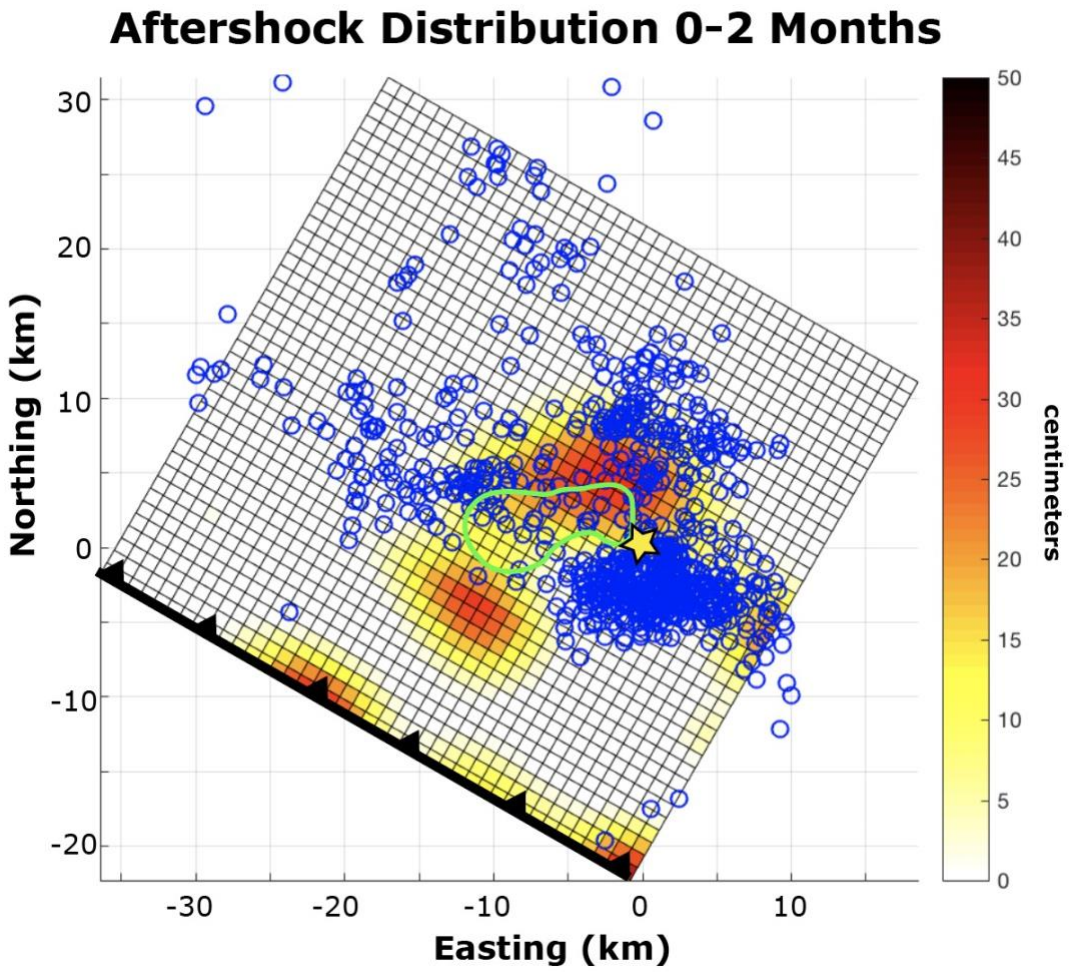

Figure 37: First 2 months distribution of aftershocks (blue circles) within +/-5 km of the main fault plane. Afterslip is after the first 2 months. Green circle represents 1.2 meter coseismic slip asperity from Figure 5).

Following an earthquake, afterslip can drive the stress on the fault to move from locations of stable sliding to areas that are locked. When the sliding areas reach locked parts of the fault, this can trigger aftershocks to follow an Omori's Law decay (*Dieterich*, 1994) due to the postseismic stress. The logarithmic decay in time of aftershock occurrence on the fault is a similar decay rate to that of afterslip on the same fault. Aftershocks within the first two months of the earthquake appear to be located in

areas surrounding the 2-month distribution of afterslip on the main fault. The absence of aftershocks in areas where afterslip is present could indicate afterslip driving the aftershock locations. This can be explained by the coseismic stress causing areas that are velocity weakening to fail, causing aftershocks (Figure 38). These observations of both decay in time and location provide further evidence that afterslip and aftershocks can be mechanically linked.

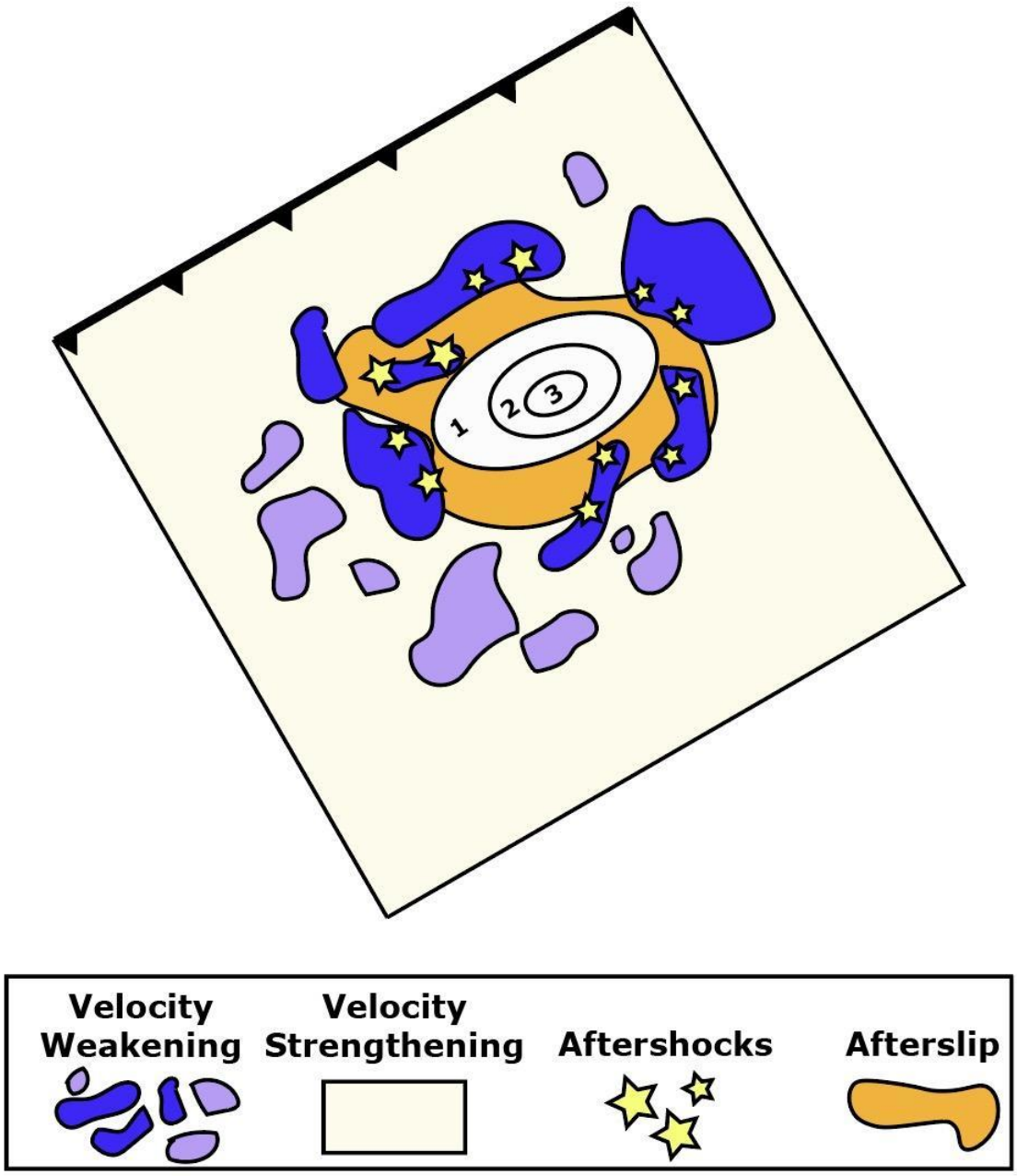

Figure 38: Example of afterslip and aftershock relationship on a fault. Afterslip occurs in areas that are velocity strengthening (tan color) while aftershocks are located on asperities (purple blobs) that become critically stressed (blue blobs) and exhibit velocity weakening behavior. Aftershocks are yellow stars and up-dip direction indicated by black arrows.

Section 5.5 Comparison of Postseismic and Coseismic Ratio

Moderate earthquakes that have postseismic deformation exceeding the amount of coseismic deformation have been recorded in the past. Similar to the 2004 Parkfield earthquake in California, afterslip appears to occur in areas of low seismicity and low coseismic slip at a similar depth of 5 km (*Freed.*, 2007). As I typically expect to see more coseismic deformation than postseismic deformation, I compare the postseismic-to-coseismic displacement ratio from GPS observations. I take up to 15 months of displacement as postseismic displacement, since displacement in the later postseismic displacement becomes insignificant. To achieve this, I collate both the horizontal and vertical components of 103 GPS stations in the area of the MeiNong earthquake. In order to see if postseismic or coseismic is dominating, I take the log of the postseismic-to-coseismic displacement ratio (Figure 39).

When analyzing the ratio of coseismic to postseismic in the horizontal, it is evident that in lower-elevation areas such as the Coastal Plains, some GPS stations reveal more postseismic deformation. On the other hand, the GPS stations located in the Western Foothills, an area of higher elevation, appear to be dominated by coseismic deformation. The Tainan Tableland, the area with a rapid postseismic transient visible on InSAR shows an equal amount of coseismic and postseismic deformation in the horizontal.

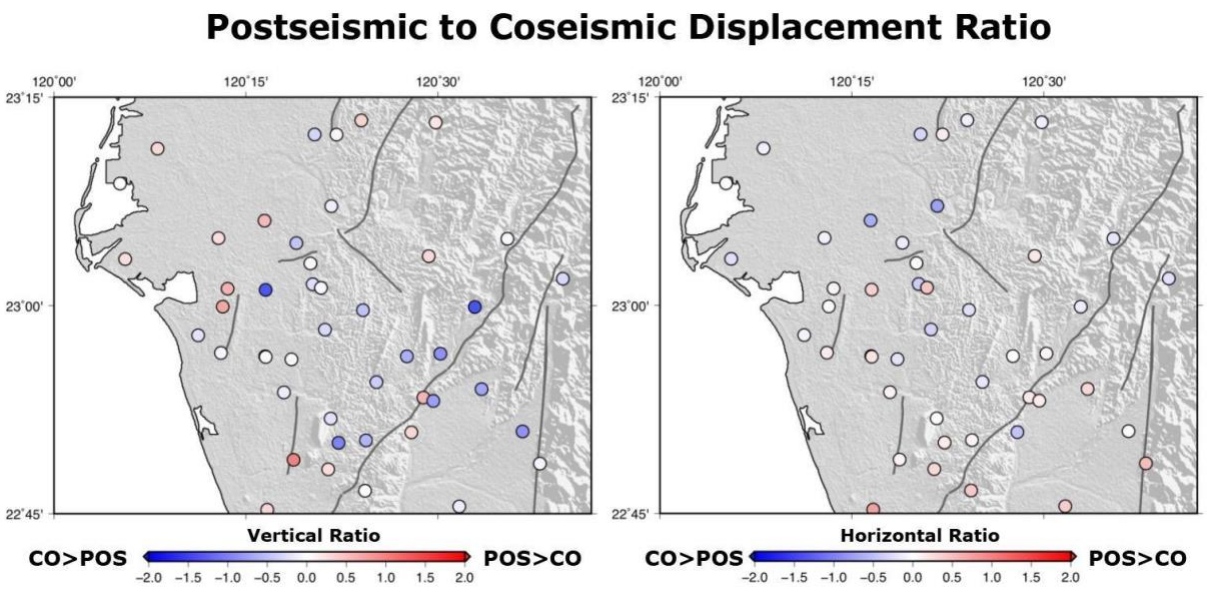

Figure 39: Ratio comparison in log scale between postseismic and coseismic horizontal and vertical displacements. Circles represent GPS stations. Dark gray lines represent active mapped faults. Red indicates more postseismic deformation present and blue indicates more coseismic deformation present.

In the vertical component, there are some GPS stations located along the Central Range that exhibit more coseismic than postseismic deformation. In the Western Foothills, there are also some stations exhibiting greater coseismic signal, similar to that in the horizontal. GPS stations located on, or near, active creeping faults show greater amounts of postseismic deformation. The Tainan Tableland shows more postseismic deformation in the vertical which is consistent with our geodetic results.

This observation clearly indicates that stress-driven afterslip alone cannot be the only postseismic mechanism, as stress-driven afterslip cannot exceed the amount of coseismic slip. Although I have not explored inclusion of shallow faults above or south of the main fault for afterslip inversions, I anticipate areas with more postseismic than coseismic displacements can be explained by shallow fault slip that was accelerated by the MeiNong earthquake. Shallow faults may have been locked and critically stressed interseismically, allowing them to accelerate slip rate in response to

the coseismic stress change. This unlocking of shallow faults and releasing of energy could have happened slowly over the 15 months after the earthquake. However, I also cannot rule out the possibility of hydrologic response near the fault zone to earthquake stress change (e.g. *Wang and Manga*, 2015; *Manga et al.* 2016). Future direction including comparison with regional groundwater level change before and after the earthquake may provide more insights into this topic.

The importance of this work is to analyze postseismic deformation using inversions of geodetic techniques in order to contribute to future seismic hazard mitigation. I link geodetic observations with regional geology to provide a better understanding the subsurface geology of the tectonically active and complex region of southwest Taiwan. Compiling and analyzing a large dataset with multiple mediums of observation can be the first step in understanding earthquake cycles and seismic potential of areas with buried faults. A previous limitation in earthquake analysis has been the lack of spatial coverage of areas affected by these natural hazards. Combining GPS and InSAR allow us to get the high temporal and spatial resolution needed to fully image surface responses to all components of the earthquake cycle.

Chapter 6: Conclusion

The rapidly colliding tectonic environment of the island of Taiwan allows us to visualize processes as the rapid convergence rate can result in much shorter earthquake cycles than other regions of the world. The 2016 M_w 6.4 MeiNong earthquake was the deadliest event to strike Taiwan since the 1999 ChiChi earthquake. This earthquake occurred on a previously unknown blind thrust fault located at ~17 km depth on a fault orientation similar to a previous event, the 2010 JiaShian earthquake. Both events are considered as reactivation of older structure related to the opening of the South China Sea (Huang et al., 2013, 2016b). Although there is no direct observation of these buried and deep structures, some of the buried structures were accelerated due to the earthquake. Geodetic measurements of the postseismic deformation can then illuminate the location of these structures, which is essential in better understanding the fault system of this area. Understanding the seismic hazard within the complex structural geology of southwest Taiwan is critical for preparing the residents for future events.

With the introduction of geodetic techniques such as InSAR and GPS, we are able to take our understanding of earthquake cycles further than previously explored. The ability to resolve ground motion to a near millimeter accuracy while covering an area of hundreds of square kilometers has allowed us to better observe the effects earthquakes have on the surface. In combining the high temporal resolution of GPS with the high spatial coverage of InSAR, we are better able to constrain faults at depth, a task difficult to accomplish prior to geodesy.

With 15 months of GPS and InSAR data, I observe the coseismic and postseismic surface displacements as well as generate a time series analysis of surface

deformation. The coseismic interferograms and GPS velocities indicate the surface uplifted ~10 cm during the earthquake in an area ~15 km away from the epicenter. Aside from the small patch of coseismic uplift roughly 9 km wide by 21 km long, no other coseismic uplift is clearly visible. In the months following the earthquake, a postseismic signal indicated the surface was continuing to uplift and areas where no coseismic displacement occurred had begun showing postseismic transients. The Tainan Tableland, ~30 km away from the epicenter, had a rapid postseismic uplift of 4 cm/year following the earthquake before returning to its previous interseismic rate. Postseismic deformation can illuminate buried faults or shallow structures which can lead us to better understanding of the fault system in this area.

This migration of afterslip may suggest heterogeneous friction properties on the fault plane surface, which allows aftershocks to occur on velocity weakening asperities and afterslip to occur on velocity strengthening asperities. After observing GPS and InSAR inversion results in the form of afterslip on the main fault and horizontal and vertical displacements on the surface, it is evident that shallow fault structures above the main detachment were accelerated by the MeiNong earthquake and produce postseismic displacement with short (<10 km) wavelength. My afterslip model that is solely based on slip among the main earthquake fault is unable to predict these short-wavelength displacements. On the other hand, the inversion model fits the overall long-wavelength postseismic signal. Modeling additional postseismic deformation mechanisms such as poroelastic rebound and inclusion of shallower faults above the main detachment to this study will assist generating a better understanding of the underlying mechanism that generated the short-wavelength displacements.

The stress driven afterslip model can fit the overall locations of deformation in the region in both vertical and horizontal components but cannot account for the total amount of surface uplift or westward motion shown from geodetic data. Similar to inversion results, the stress driven afterslip model also indicates either a combination of locked shallow faults above the detachment were stressed coseismically and began creeping, or poroelastic rebound caused the remainder of the uplift. A combination of postseismic mechanisms, not just afterslip, and a shallow distribution of faults are needed in order to better explain the postseismic surface response of the MeiNong earthquake.

Given that I see more postseismic deformation than coseismic deformation in some regions, this is another indication that other mechanisms are generating uplift following the earthquake. The coseismic stress could be the triggering mechanism of the critically stressed shallow faults that released energy slowly over time as a result of the coseismic stress perturbation. Understanding locations of blind thrust faults, the triggering mechanism for shallow faults as well as the movement of fluids at shallow depths of southwest Taiwan is important for future studies. Postseismic studies assist in illuminating these buried structures and play an important role in understanding earthquake cycles for future seismic hazard mitigation.

Appendices

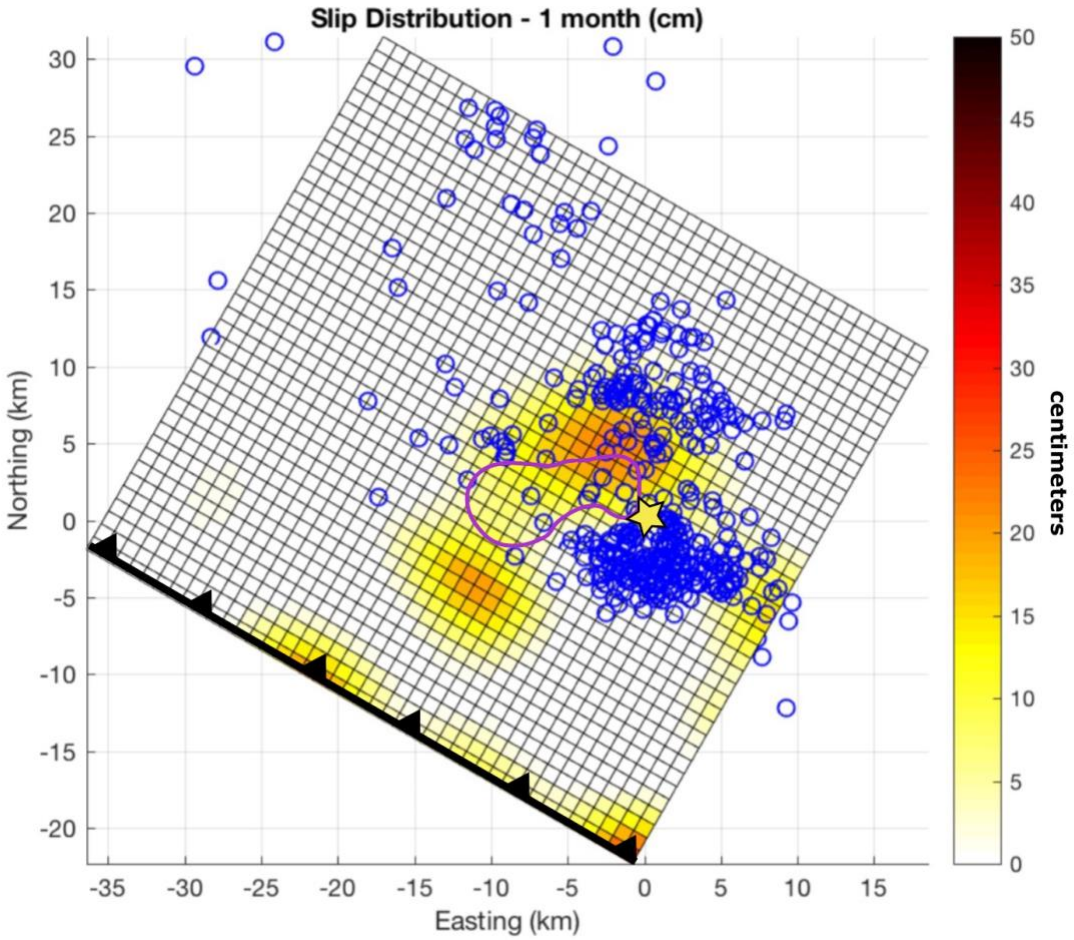

Figure A1: 1-month afterslip distribution. Blue circles indicate aftershocks in the same time period. Slip distribution is in cm.

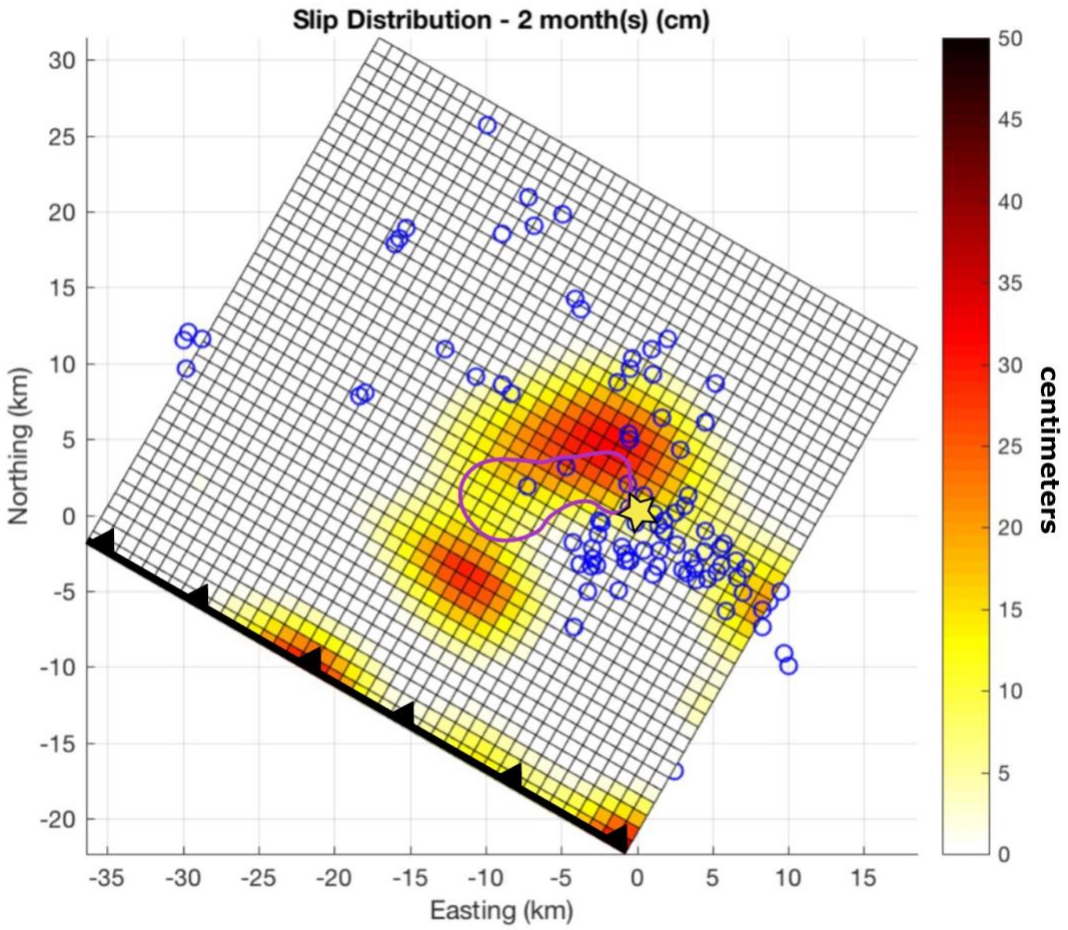

Figure A2: 2-month afterslip distribution. Blue circles indicate aftershocks in the same time period. Slip distribution is in cm.

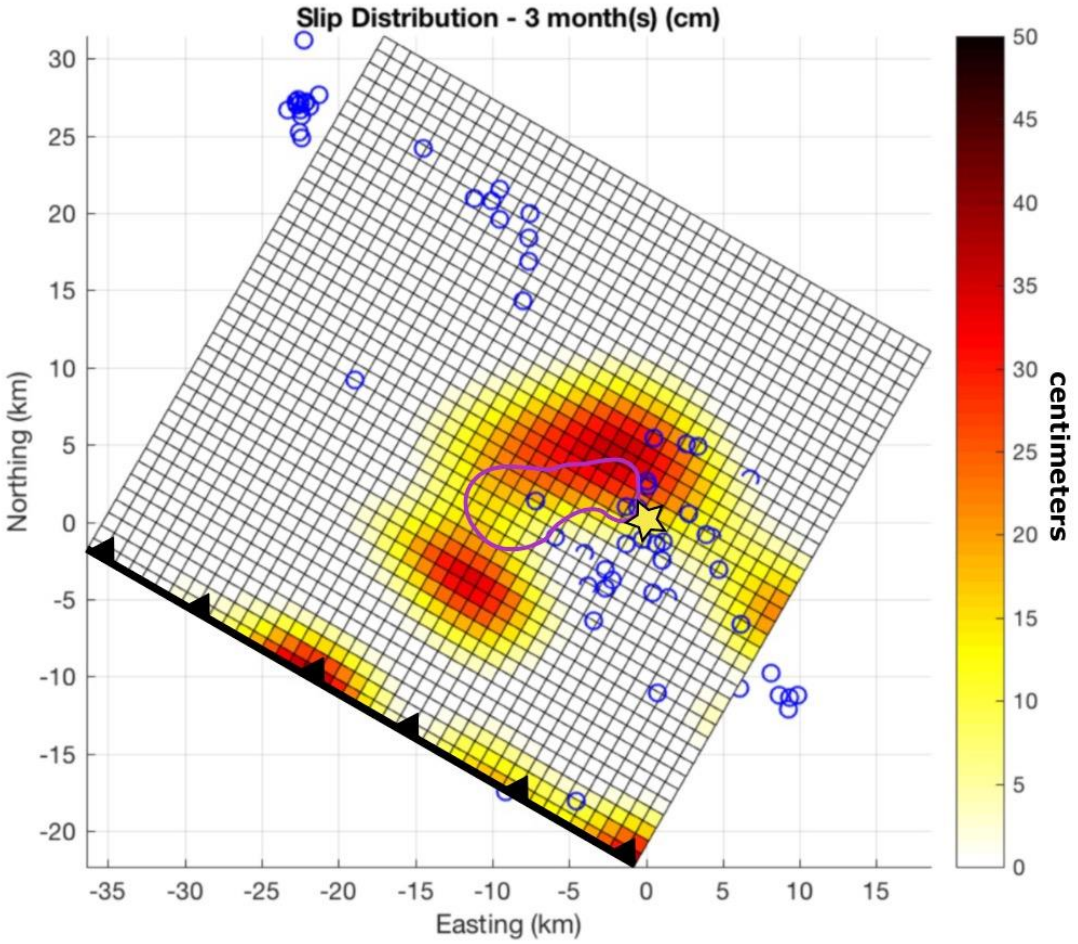

Figure A3: 3-month afterslip distribution. Blue circles indicate aftershocks in the same time period. Slip distribution is in cm.

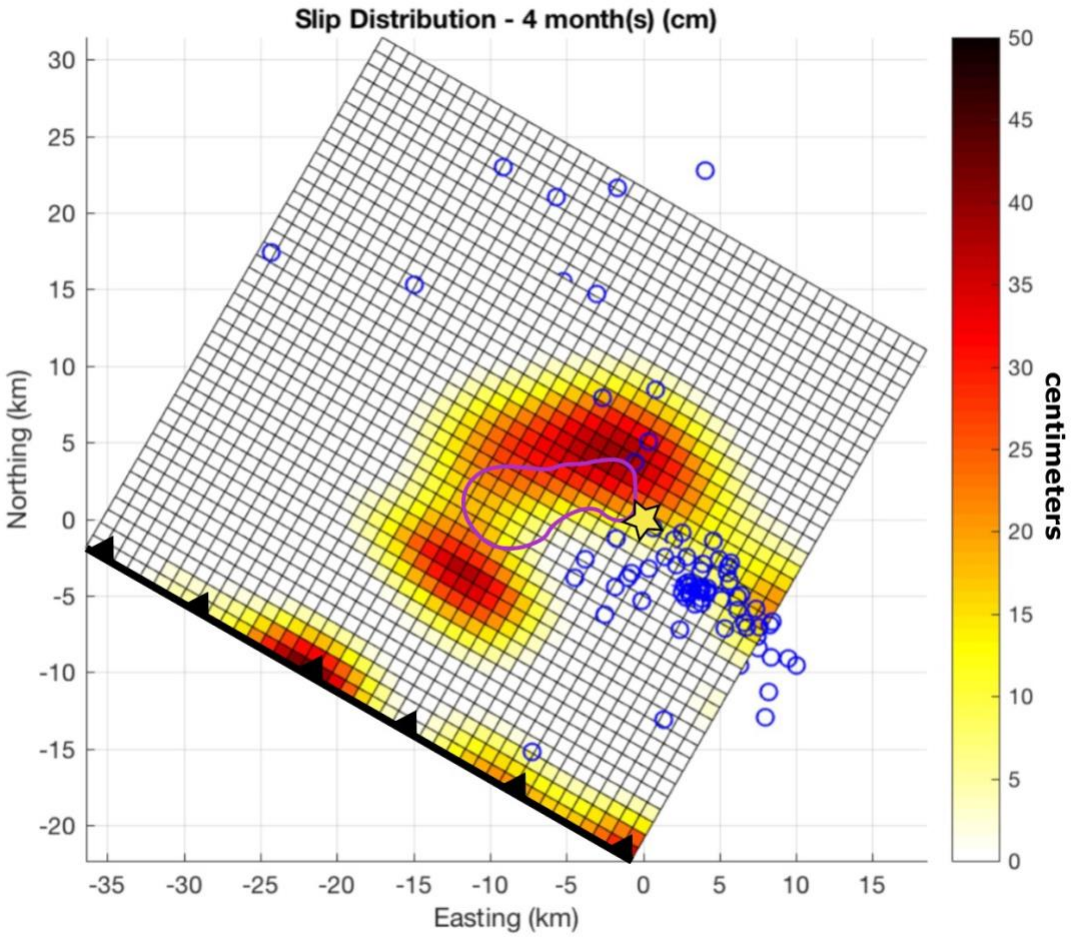

Figure A4: 4-month afterslip distribution. Blue circles indicate aftershocks in the same time period. Slip distribution is in cm.

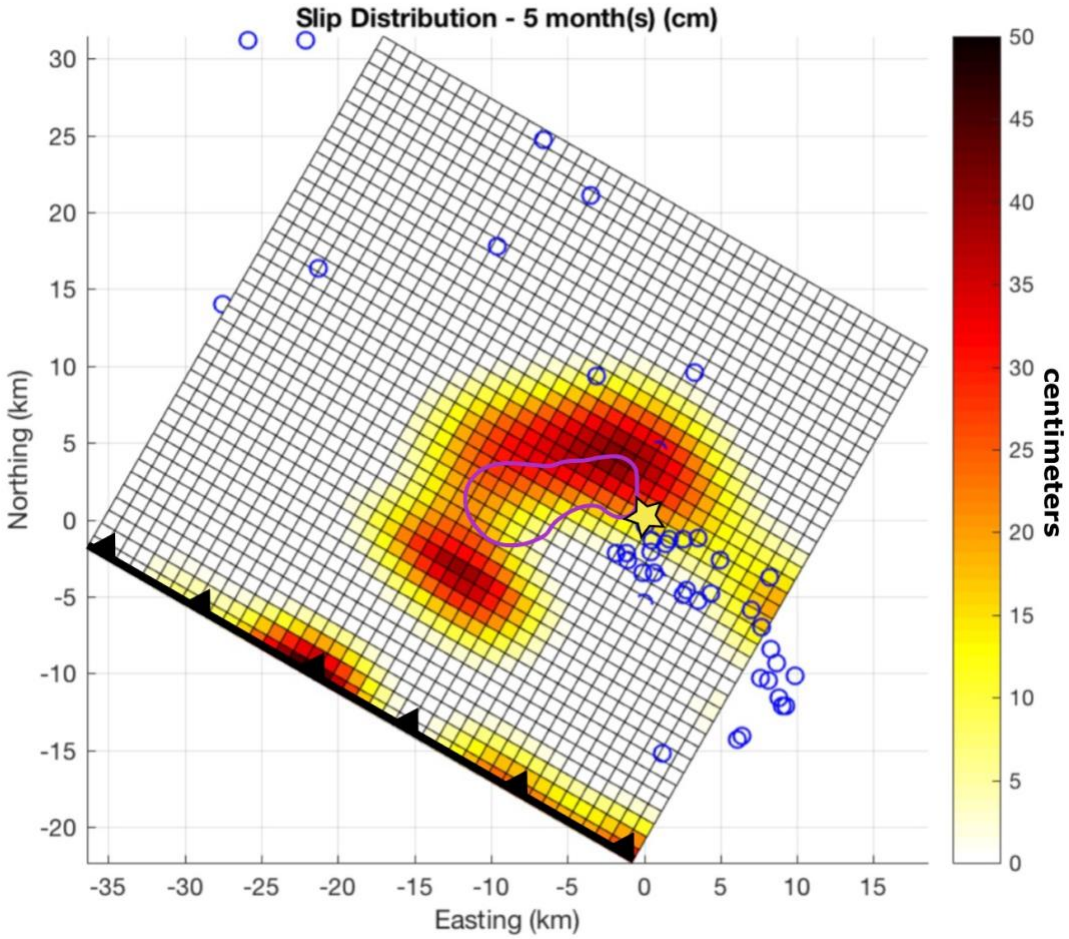

Figure A5: 5-month afterslip distribution. Blue circles indicate aftershocks in the same time period. Slip distribution is in cm.

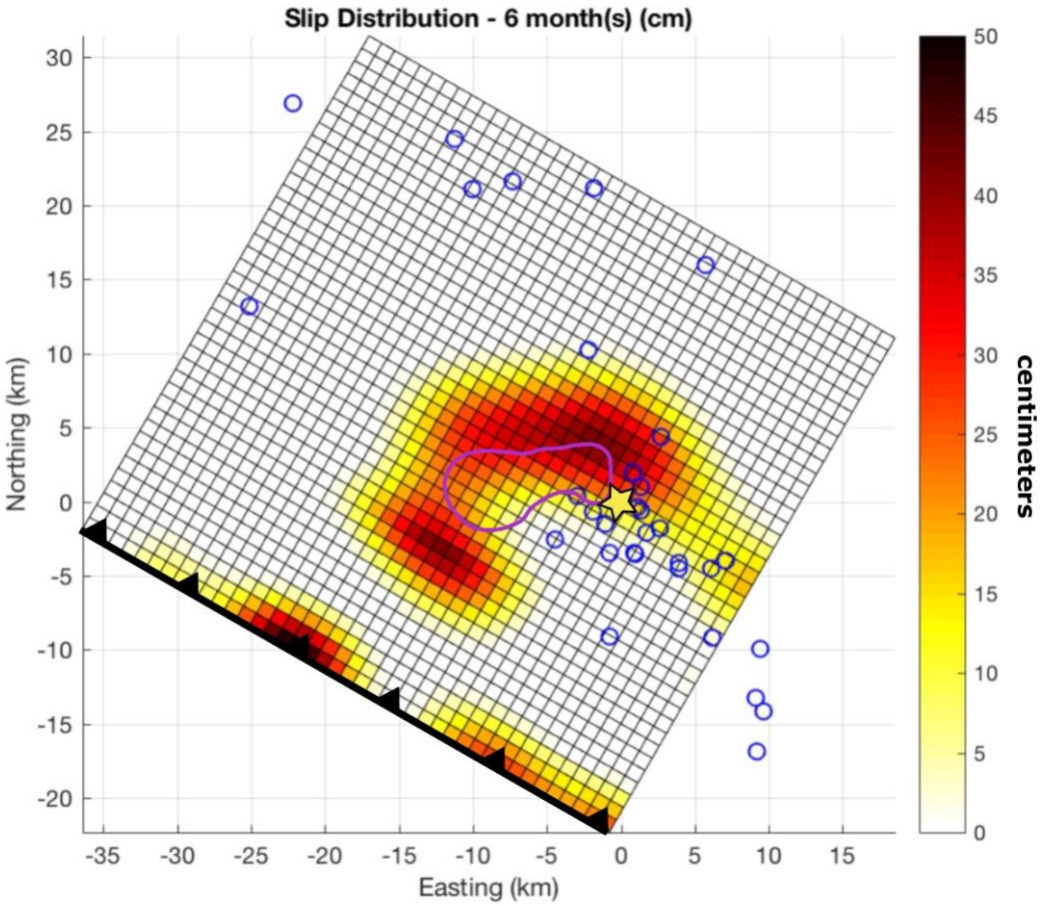

Figure A6: 6-month afterslip distribution. Blue circles indicate aftershocks in the same time period. Slip distribution is in cm.

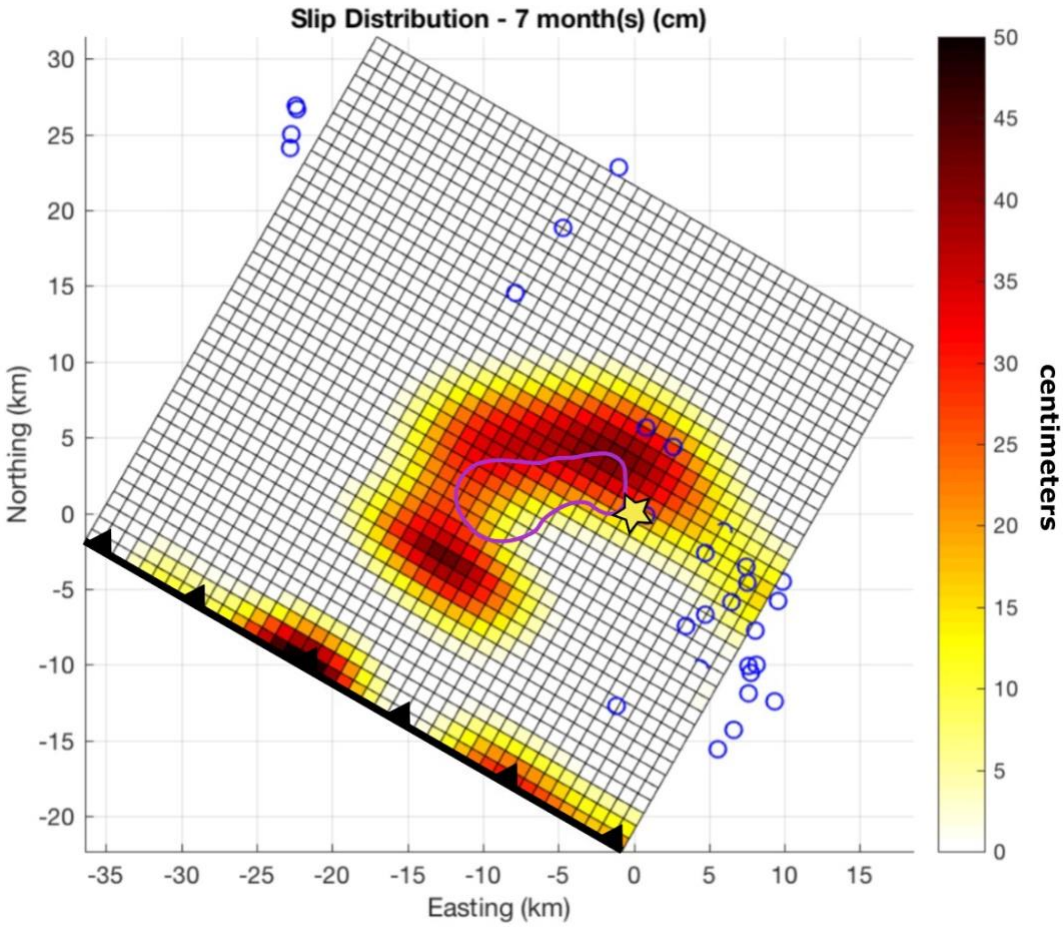

Figure A7: 7-month afterslip distribution. Blue circles indicate aftershocks in the same time period. Slip distribution is in cm.

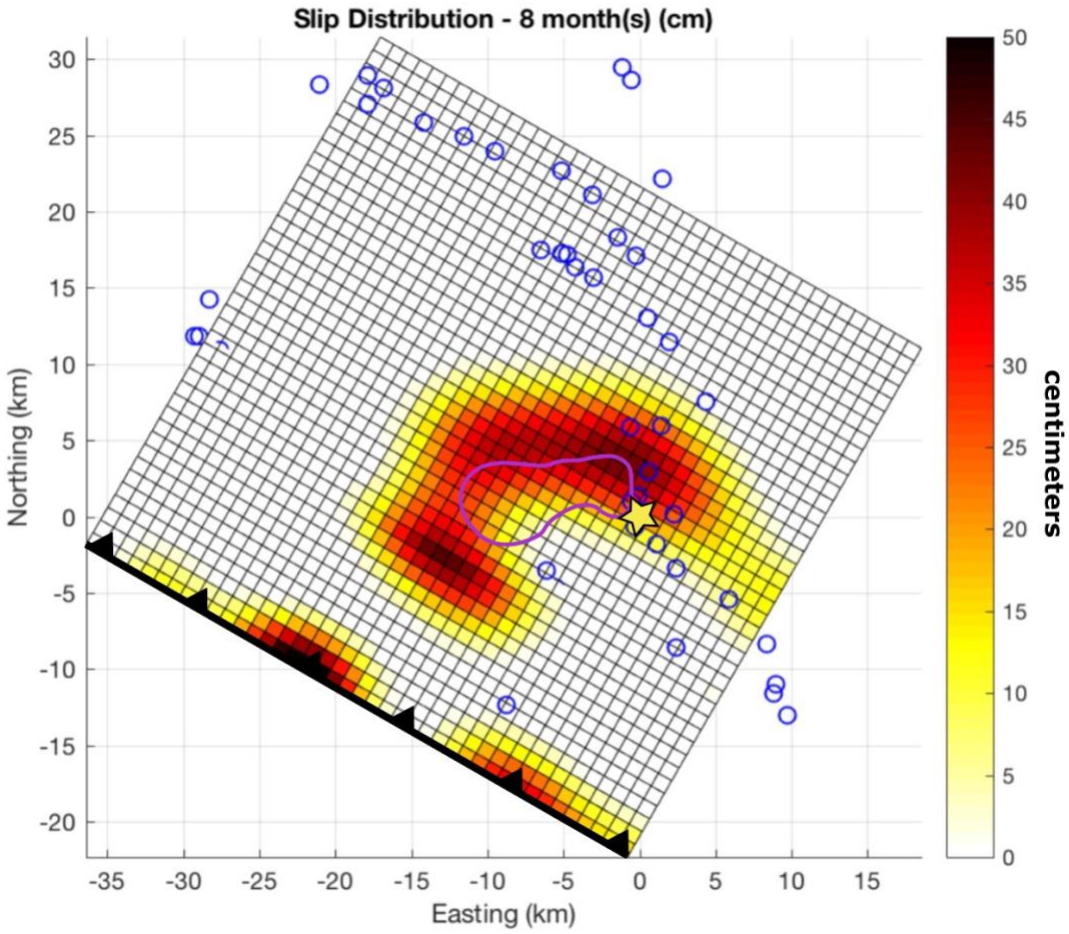

Figure A8: 8-month afterslip distribution. Blue circles indicate aftershocks in the same time period. Slip distribution is in cm.

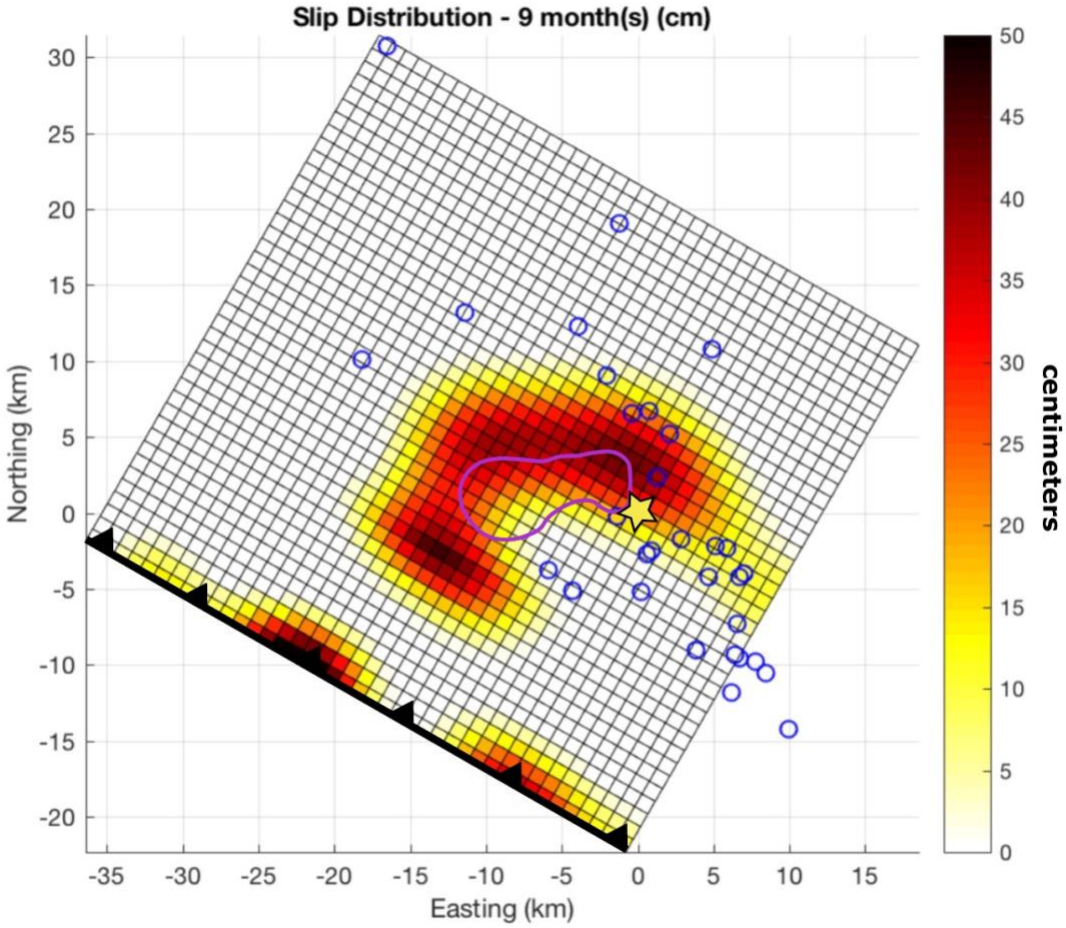

Figure A9: 9-month afterslip distribution. Blue circles indicate aftershocks in the same time period. Slip distribution is in cm.

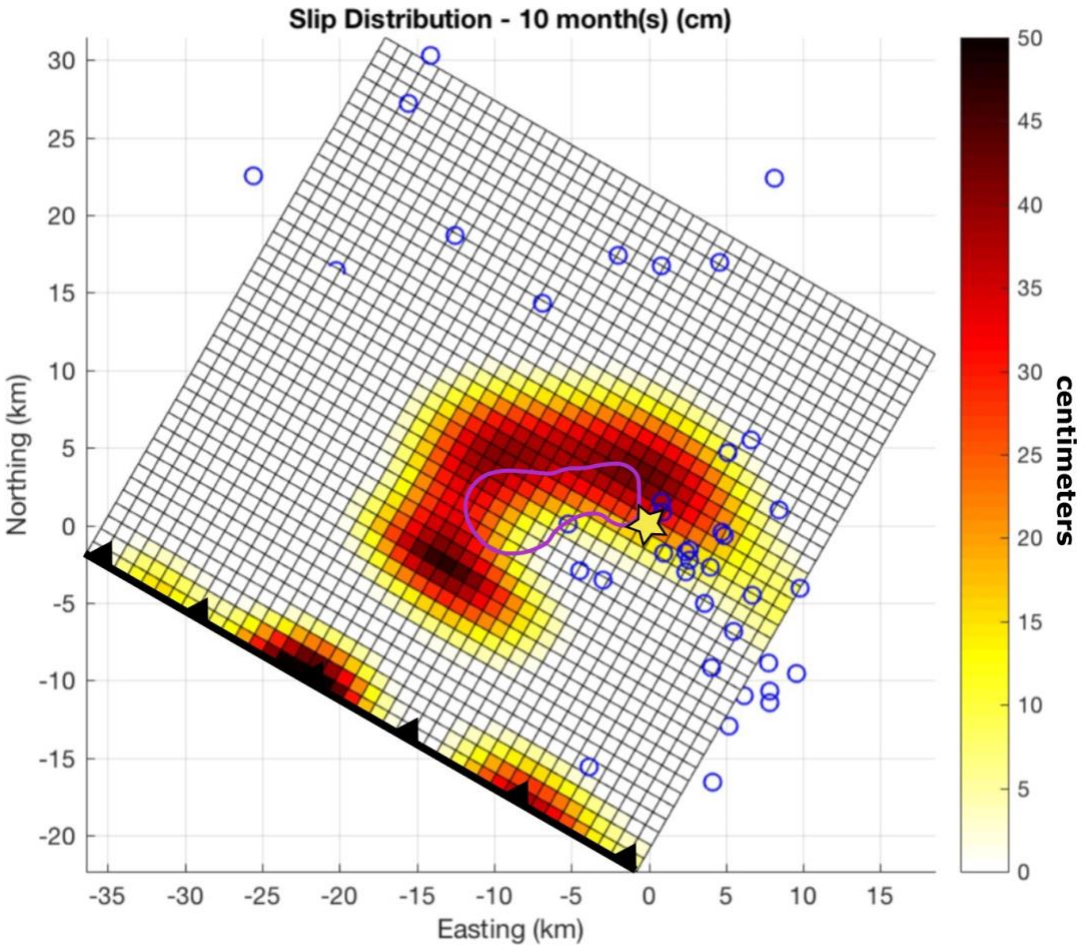

Figure A10: 10-month afterslip distribution. Blue circles indicate aftershocks in the same time period. Slip distribution is in cm.

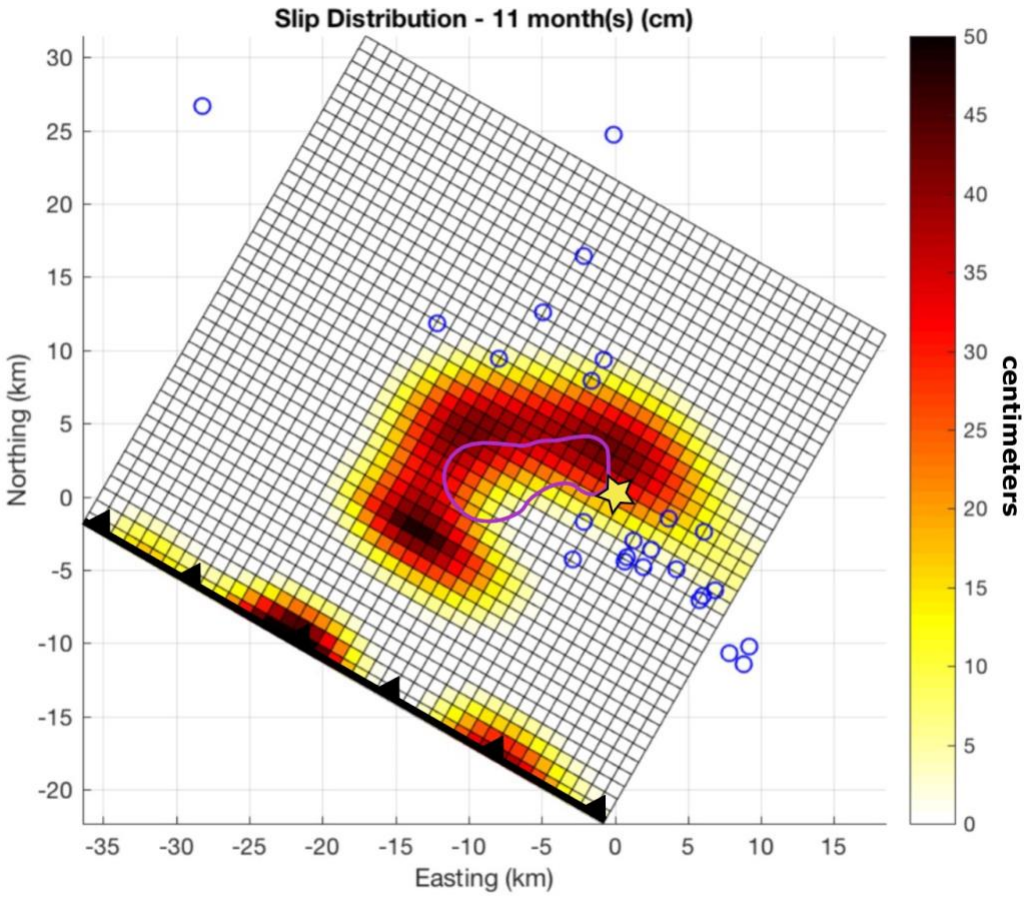

Figure A11: 11-month afterslip distribution. Blue circles indicate aftershocks in the same time period. Slip distribution is in cm.

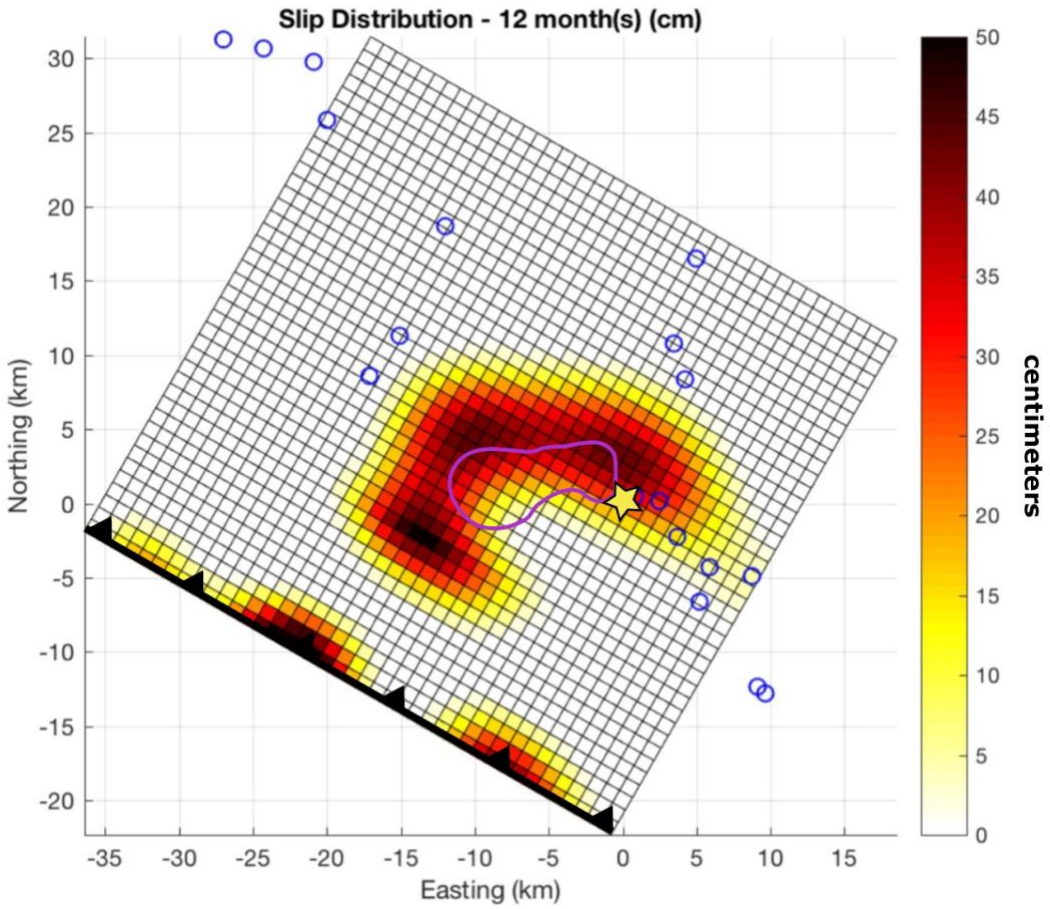

Figure A12: 12-month afterslip distribution. Blue circles indicate aftershocks in the same time period. Slip distribution is in cm.

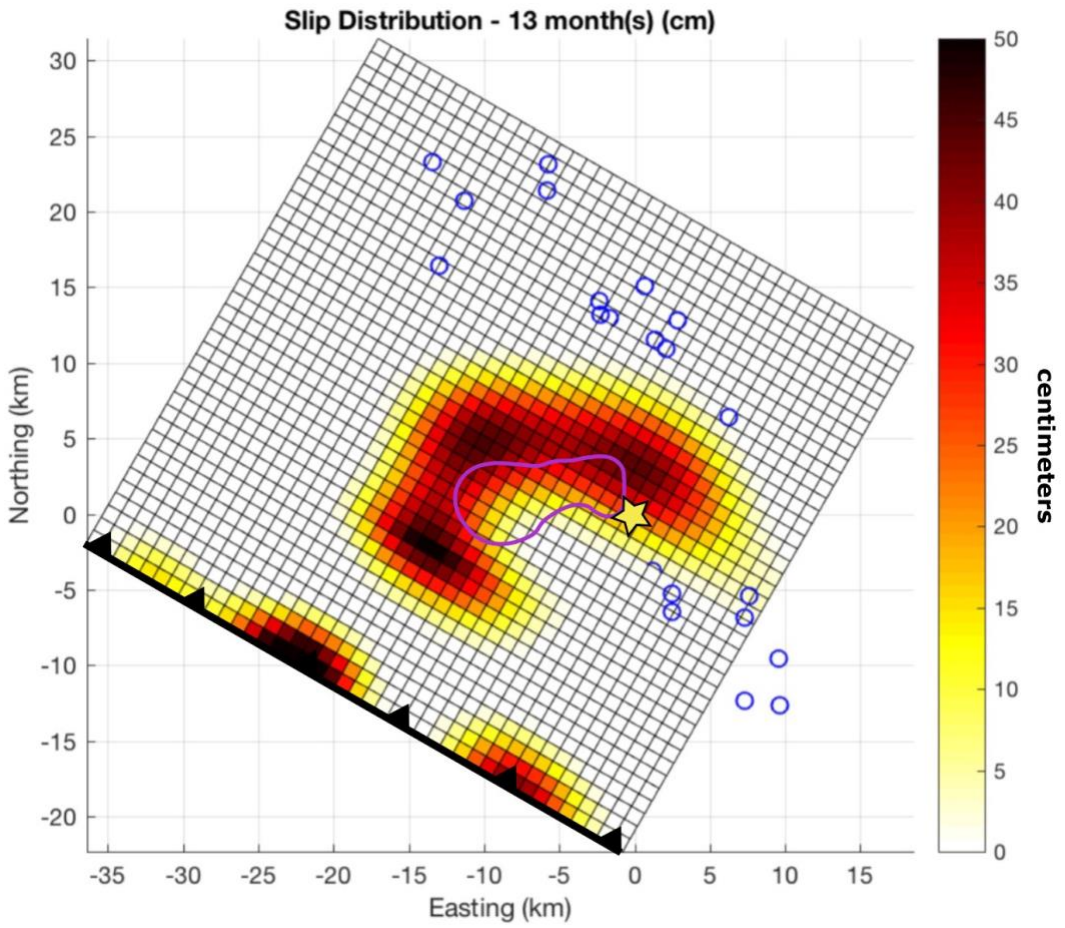

Figure A13: 13-month afterslip distribution. Blue circles indicate aftershocks in the same time period. Slip distribution is in cm.

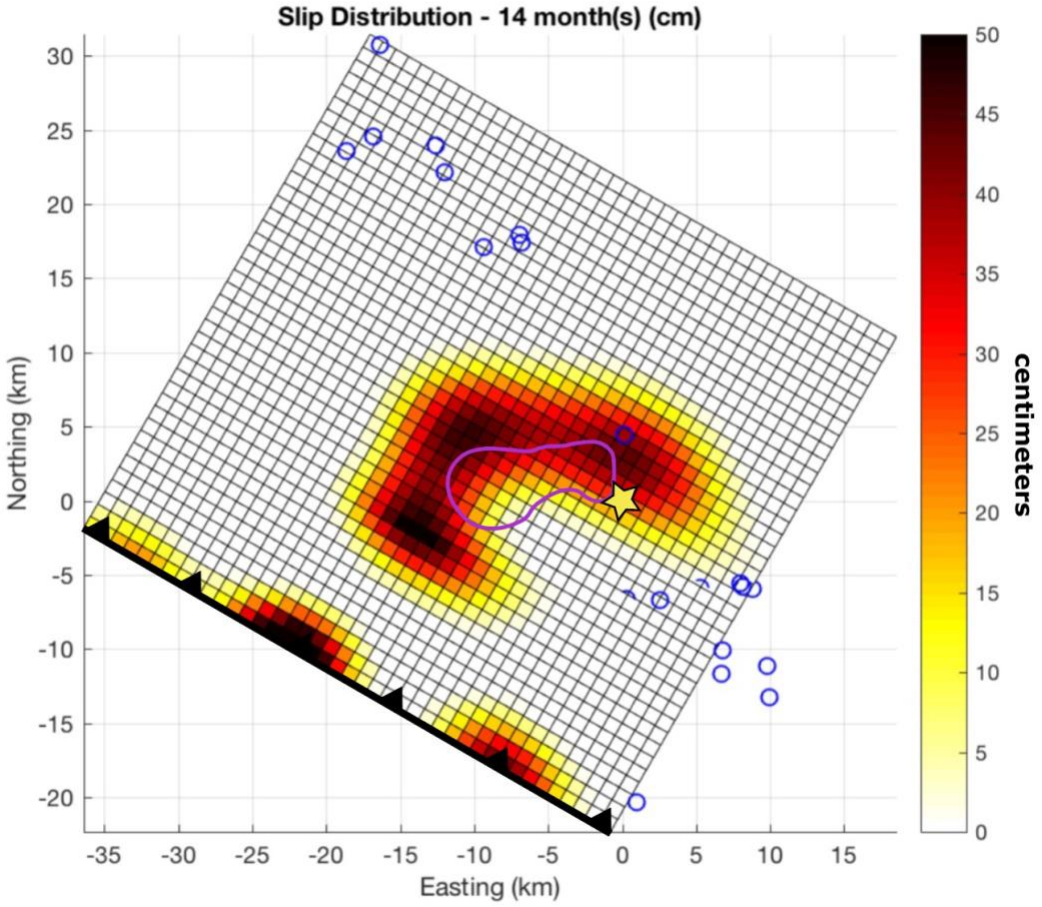

Figure A14: 14-month afterslip distribution. Blue circles indicate aftershocks in the same time period. Slip distribution is in cm.

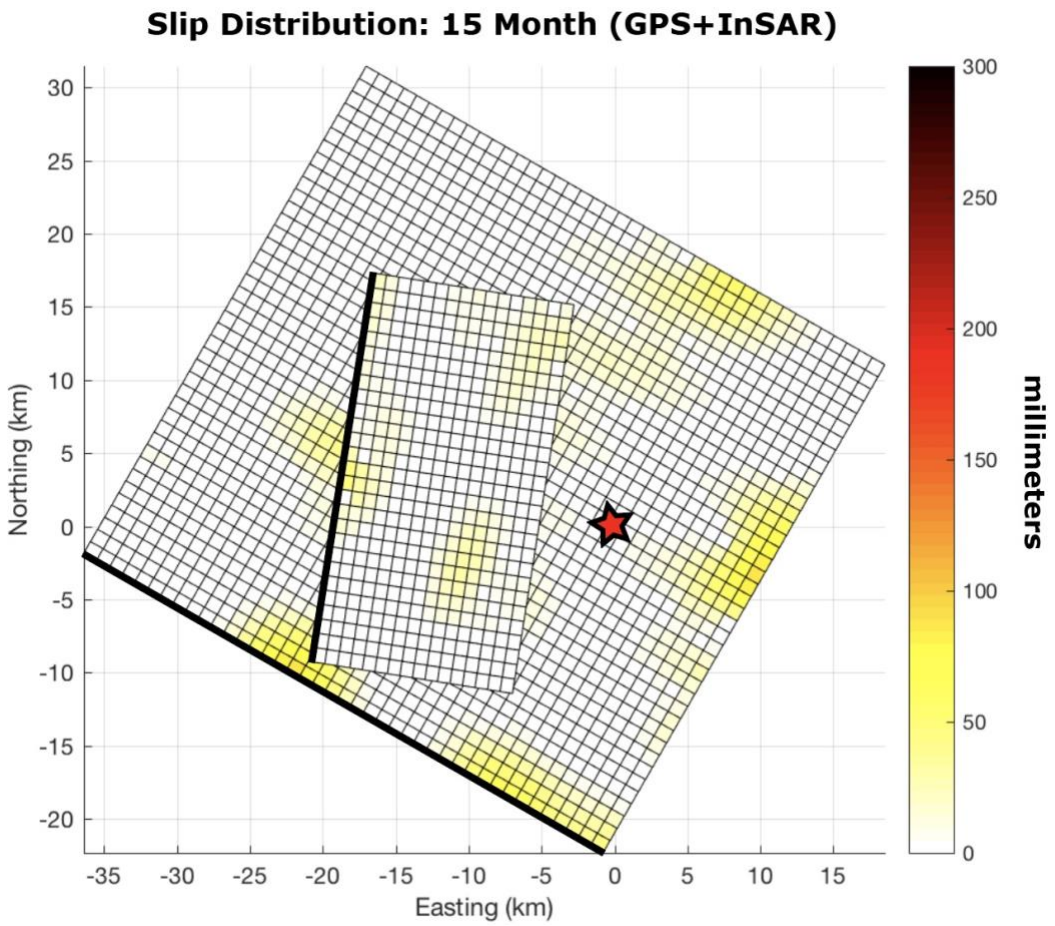

Figure A15: 14 to 15-month afterslip distribution of the main and shallow fault. Slip distribution is in mm.

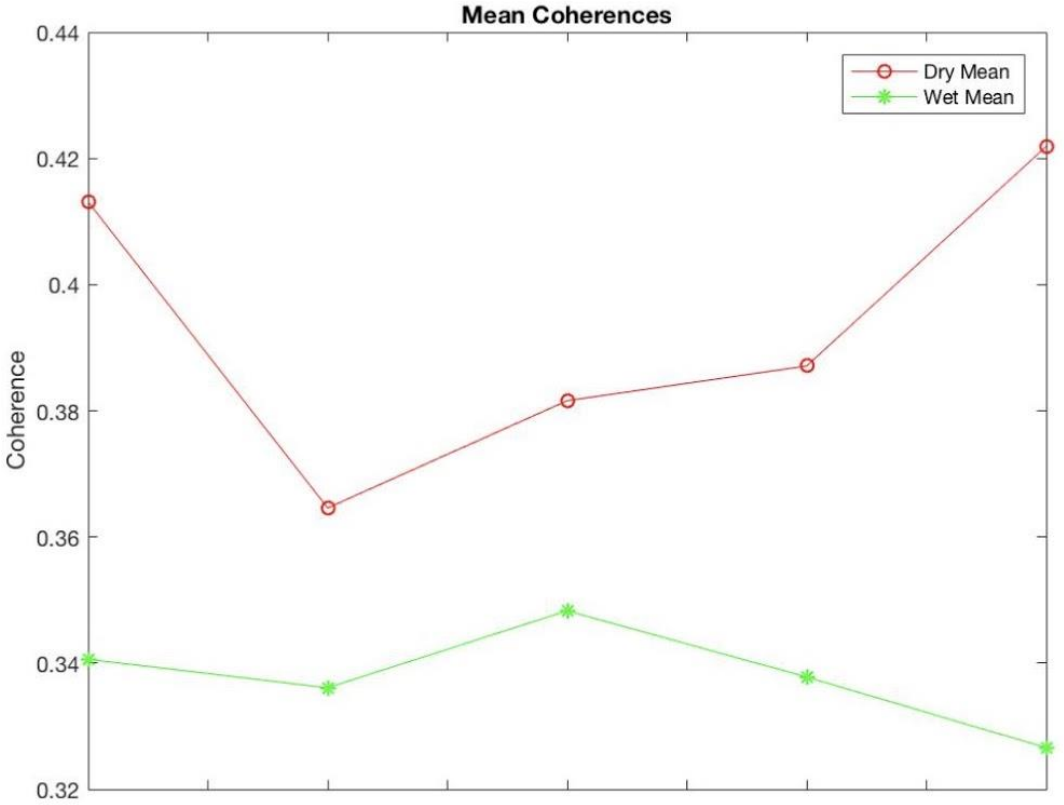
Mean Coherences
Dry Mean
Wet Mean
Coherence
0.44
0.42
0.4
0.38
0.36
0.34
0.32

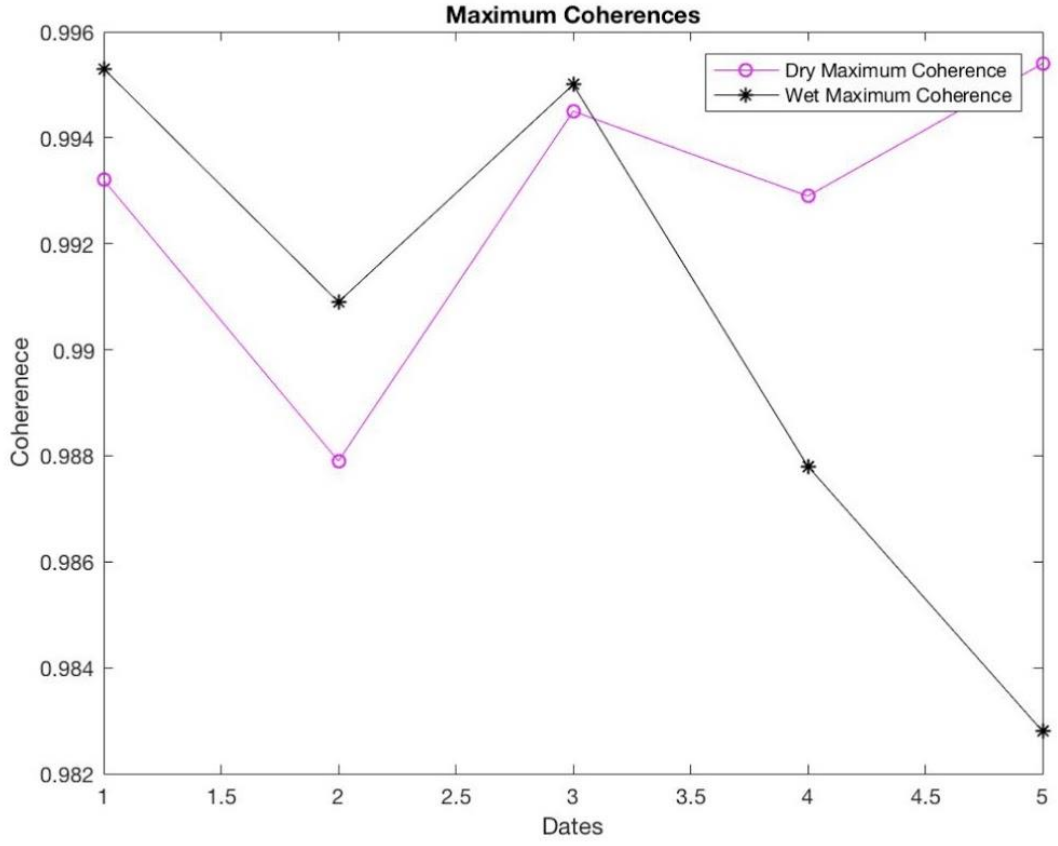
Maximum Coherences
Dry Maximum Coherence
Wet Maximum Coherence
Coherenece
0.996
0.994
0.992
0.99
0.988
0.986
0.984
0.982
1
1.5
2
2.5
3
3.5
4
4.5
5
Dates

Figure A16: Mean coherence and maximum coherence for both wet and dry seasons.

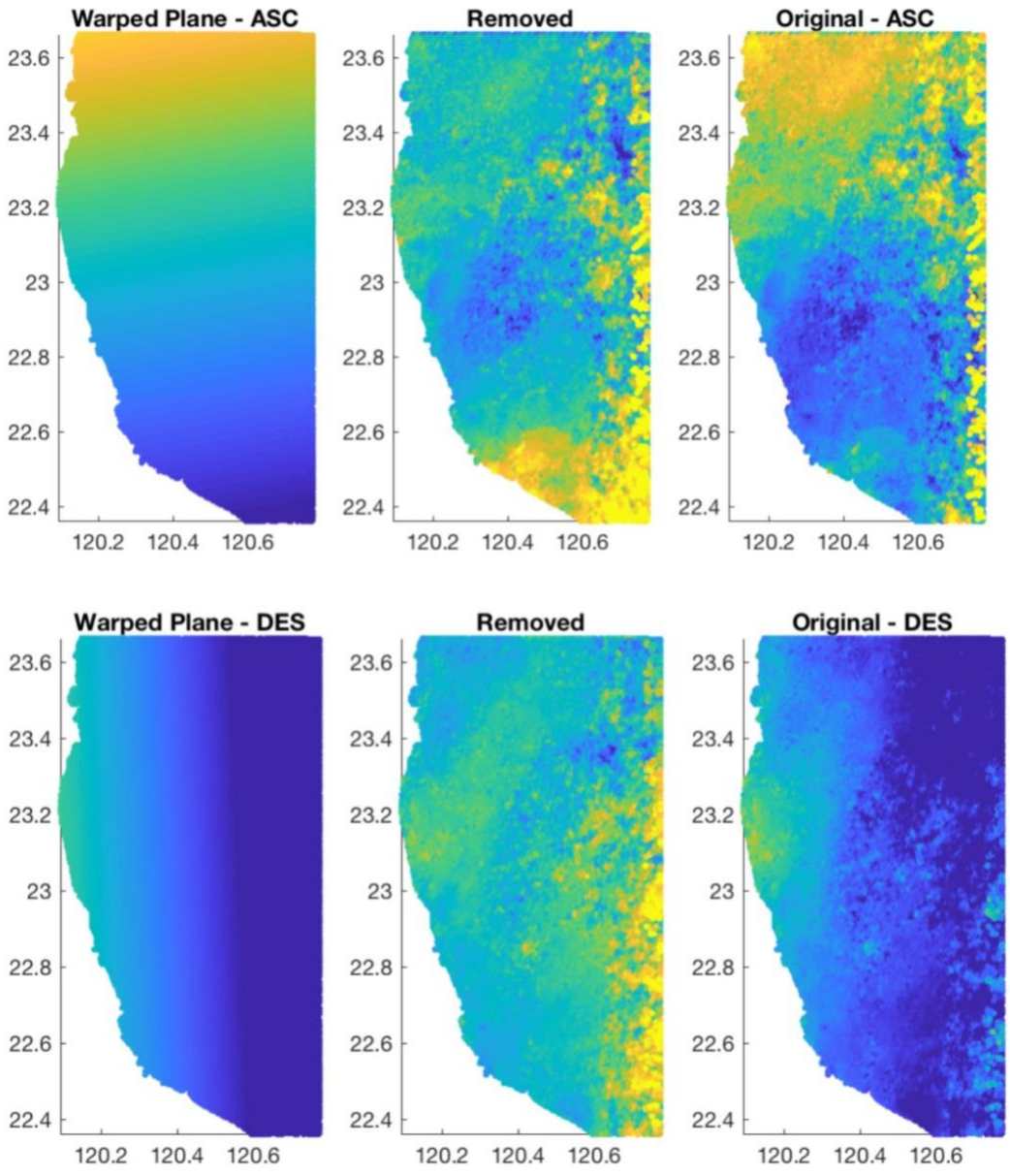

Figure A17: Ascending and descending plane functions removed from original data.

Bibliography

Berardino, P., Fornaro, G., Lanari, R., Sansosti, E., 2002. A new algorithm for surface deformation monitoring based on small baseline differential SAR interferograms. *IEEE Trans. Geosci. Remote Sens. 40*, 2375–2383.

Allen, C.T., 1995. Interferometric synthetic aperture radar. *IEEE Geoscience and Remote Sensing Society Newsletter*, No. 96; Sept. 1995, pp. 6-13.

Bürgmann, R., Rosen, P. A., & Fielding, E. J. (2000). Synthetic Aperture Radar Interferometry to Measure Earth's Surface Topography and Its Deformation. *Annual Review of Earth and Planetary Sciences*, *28*(1), 169-209. doi:10.1146/annurev.earth.28.1.169

Colesanti, C., Ferretti, A., Novali, F., Prati, C., Rocca, F., 2003. SAR monitoring of progressive and seasonal ground deformation using the permanent scatterers technique. *Geosci. Remote Sens. IEEE Trans. 41* (7), 1685–1701.

Chen, Y.-G. and Liu, T.-K., 2000, Holocene uplift and subsidence along an active tectonic margin southwestern Taiwan, Quaternary Science Reviews, 19, 923-930.

Chen, C.W., and H. A. Zebker (2002), Phase unwrapping for large SAR interferograms: Statistical segmentation and generalized network models, IEEE Trans. Geosci. Remote Sens., 40(8), 1709–1719.

Chiang, P.-H., Y.-J. Hsu, and W.-L. Chang (2016), Fault modeling of the 2012 Wutai, Taiwan earthquake and its tectonic implications, *Tectonophysics*, *666*, 66–75, doi:10.1016/j.tecto.2015.10.015.

Chinese Petroleum Corporation, 1989: Geological map of Tai-Nan, scale 1:100,000. Taiwan Petroleum Exploration Division, Chinese Petroleum Corporation, Taiwan, R.O.C.

Ching, K.-E., K. M. Johnson, R.-J. Rau, R. Y. Chuang, L.-C. Kuo, and P.-L. Leu (2011), Inferred fault geometry and slip distribution of the 2010 Jiashian, Taiwan, earthquake is consistent with a thick-skinned deformation model, *Earth Planet. Sci. Lett.*, doi:10.1016/j.epsl.2010.10.021.

Chung, C. T., 1968: Regional stratigraphic and structural study of the Tainan foothills area, southern Taiwan. Petrol. Geol. Taiwan, 6, 15-31.

Diao, F., X. Xiong, R. Wang, Y. Zheng, T. R. Walter, H. Weng, and J. Li (2013), Overlapping postseismic deformation processes: Afterslip and viscoelastic relaxation following the 2011Mw 9.0 Tohoku (Japan) earthquake, Geophys. J. Int., 196, 218–229, doi:10.1093/gji/ggt376.

Dieterich, J. H. (1994), A constitutive law for the rate of earthquake production and its application to earthquake clustering, *J. Geophys.Res.*,99, 2601–2618.

Ding, J.T. Freymueller, Q. Wang, R. Zou. 2015. Coseismic and early postseismic deformation of the 5 January 2013 *M*w 7.5 Craig earthquake from static and kinematic GPS solutions. *Bull Seismol Soc Am*, 105, pp. 1153-1164

Farr, T. G., et al. (2007), The shuttle radar topography mission, Rev. Geophys., 45, RG2004, doi:10.1029/2005RG000183.

Ferretti, A., Prati, C., Rocca, F., 2001. Permanent scatterers in SAR interferometry. *Geosci. Remote Sens. IEEE Trans. 39* (1), 8–20.

Fielding, E. J., T. J. Wright, J. Muller, B. E. Parsons, and R. Walker (2004), Aseismic deformation of a fold-and-thrust belt imaged by synthetic aperture radar interferometry near Shahdad, southeast Iran, Geology, 32, 577–580, doi:10.1130/G20452.1.

Freed, A. M. (2007), Afterslip (and only afterslip) following the 2004 Parkfield, California, earthquake, *Geophys. Res. Lett.*, 34, L06312, doi:10.1029/2006GL029155.

Harris, R.A., and Segall, P., 1987, Detection of a Locked Zone at Depth on the Parkfield, California, Segment of the San Andreas Fault: *J. geophys*. Res, v. 92, p. 7945-7962.

Ho, Chun-sun, 1975: Tai-wan-di-zhi-gai-lun, Ministry of Economic Affairs, R.O.C., p. 118.

Hu, J.-C. et al. (2007), Coseismic deformation revealed by inversion of strong motion and GPS data: the 2003 Chengkung earthquake in eastern Taiwan, *Geophysical Journal International*, *169*(2), 667–674, doi:10.1111/j.1365-246x.2007.03359.x.

Huang, H.-H., Y.-M. Wu, X. Song, C.-H. Chang, S.-J. Lee, T.-M. Chang, and H.-H. Hsieh (2014), Joint Vp and Vs tomography of Taiwan: Implications for subduction-collision orogeny, Earth Planet. Sci. Lett., 392, 177–191, doi:10.1016/j.epsl.2014.02.026.

Huang, M.-H., Hu, J.-C., Hsieh, C.-S., Ching, K.-E., Rau, R.-J., Pathier, E., Fruneau, B., Deffontaines, B., 2006. A growing structure near the deformation front in SW Taiwan as deduced from SAR interferometry and geodetic observation. Geophys. Res. Lett. 33, L12305.

Huang, M.-H., J.-C. Hu, K.-E. Ching, R.-J. Rau, C.-S. Hsieh, E. Pathier, B. Fruneau, and B. Deffontaines (2009), Active deformation of Tainan tableland of southwestern Taiwan based on geodetic measurements and SAR interferometry, *Tectonophysics*, *466*(3-4), 322–334, doi:10.1016/j.tecto.2007.11.020.

Huang, M.-H., D. Dreger, R. Bürgmann, S.-H. Yoo, and M. Hashimoto (2013), Joint inversion of seismic and geodetic data for the source of the 2010 March 4, Mw 6.3 Jia-Shian, SW Taiwan, earthquake, *Geophys. J. Int.*, 193, 1608–1626.

Huang, M.-H., R. Bürgmann, and J.-C. Hu (2016a), Fifteen years of surface deformation in western Taiwan: Insight from SAR interferometry, *Tectonophysics*, doi:10.1016/j.tecto.2016.02.021.

Huang, M.-H., H. Tung, E. J. Fielding,H.-H. Huang, C. Liang, C. Huang, and J.-C. Hu (2016b), Multiple fault slip triggered above the 2016 Mw 6.4 MeiNong earthquake in Taiwan, *Geophys. Res. Lett*., 43, 7459–7467, doi:10.1002/2016GL069351.

Hsu, Y.-J., S.-B. Yu, M. Simons, L.-C. Kuo, and H.-Y. Chen (2009), Interseismic crustal deformation in the Taiwan plate boundary zone revealed by GPS observations, seismicity, and earthquake focal mechanisms, *Tectonophysics*, 479, 4–18, doi:10.1016/j.tecto.2008.11.016.

Hsu, Y.-J., S.-B. Yu, L.-C. H. Kuo, Y.-C. Tsai, and H.-Y. Chen (2011), Coseismic deformation of the 2010 Jiashian, Taiwan earthquake and implications for fault activities in southwestern Taiwan, *Tectonophysics*, 502, 328–335, doi:10.1016/j.tecto.2011.02.005.

Kanamori, H., (1994), MECHANICS OF EARTHQUAKES: Annual Review of Earth and Planetary Sciences, v. 22, p. 207-237.

Kenny, C., 2009, Why do people die in earthquakes? The costs, benefits and institutions of disaster risk reduction in developing countries.

Lallemand, S. and Liu, C. S., (1998), *Geodynamic implications of present-day kinematics in the southern Ryukyus, J. G. S. C.* ***41****: 551–564.*

Lange, D., J. R. Bedford, M. Moreno, F. Tilmann, J. C. Baez, M. Bevis, and F. Kruger (2014), Comparison of postseismic afterslip models with aftershock seismicity for three subduction-zone earthquakes: Nias 2005, Maule 2010 and Tohoku 2011, *Geophysical Journal International*, *199*(2), 784–799, doi:10.1093/gji/ggu292.

Le Béon, M. L. et al. (2017), Shallow geological structures triggered during the Mw 6.4 Meinong earthquake, southwestern Taiwan, *Terrestrial, Atmospheric and Oceanic Sciences*, *28*(5), 663–681, doi:10.3319/tao.2017.03.20.02.

Lin, C.-Y., Chien, Y.-Y., Su, C.-J., Kueh, M.-T., & Lung, S.-C. (2017). Climate variability of heat wave and projection of warming scenario in Taiwan. *Climatic Change*, *145*(3), 305–320. https://doi.org/10.1007/s10584-017-2091-0

Lin, K.-C., J.-C. Hu, K.-E. Ching, J. Angelier, R.-J. Rau, S.-B. Yu, C.-H. Tsai, T.-C. Shin, and M.-H. Huang (2010), GPS crustal deformation, strain rate, and seismic activity after the 1999 Chi-Chi earthquake in Taiwan, *Journal of Geophysical Research*, *115*(B7), doi:10.1029/2009jb006417.

Manga, M., C.-Y. Wang, and M. Shirzaei (2016), Increased stream discharge after the 3 September 2016 Mw 5.8 Pawnee, Oklahoma earthquake, Geophys. Res. Lett., 43, doi:10.1002/2016/GL071268.

Marc, O., J. Suppe, S. Huang, M. Le Béon, M. H. Huang, and J. C. Hu, (2010), Deep structure and deformation history of the rapidly growing Tainan anticline, southwestern Taiwan. AGU Fall Meeting, San Francisco, USA.

Osmanoğlu, B., Sunar, F., Wdowinski, S., & Cabral-Cano, E. (2016), Time series analysis of InSAR data: Methods and trends. *ISPRS Journal of Photogrammetry and Remote Sensing, 115*, 90-102. doi:10.1016/j.isprsjprs.2015.10.003

Peltzer, G., Rosen, P., Rogez, F., and Hudnut, K. (1998), Poroelastic rebound along the Landers 1992 earthquake surface rupture, *J. Geophys. Res.*, 103(B12), 30131– 30145, doi:10.1029/98JB02302.

Perfettini, H., and Avouac, J.-P. (2004), Postseismic relaxation driven by brittle creep: A possible mechanism to reconcile geodetic measurements and the decay rate of aftershocks, application to the Chi-Chi earthquake, Taiwan, *J. Geophys. Res.*, 109, B02304, doi:10.1029/2003JB002488.

Perfettini, H., and J.-P. Avouac (2007), Modeling afterslip and aftershocks following the 1992 Landers earthquake,J. Geophys. Res.,112, B07409,doi:10.1029/2006JB004399.

Rosen, P. A., Gurrola, E., Sacco, G. F., Zebker, H. (2012), The InSAR scientific computing environment, Proc. EUSAR, Nuremberg, Germany, 730–733.

Scholz, C. (1998). Scholz, C. H. Earthquakes and friction laws. Nature 391, 37-42. Nature. 391. 37-42. 10.1038/34097.

Smith, S.W., and Wyss, M., 1968, Displacement on the San Andreas fault subsequent to the 1966 Parkfield earthquake: Bulletin of the Seismological Society of America, v. 58, p. 1955-1973.

Toda, S., R. S., Stein, V., Sevilgen, and J., Lin (2011), Coulomb 3.3 Graphic-rich deformation and stress-change software for earthquake, tectonic, and volcano research and teaching user guide: U.S. Geological Survey Open-File Report 2011-1060, 63

Wang, R., F. Lorenzo Martín, and F. Roth (2003), Computation of deformation induced by earthquakes in a multi-layered elastic crust-FORTRAN programs EDGRN/EDCMP, *Comput. Geosci*., 29, 195-207.

Wang, L., Shum, C. K., Simons, F. J., Tapley, B., and Dai, C. (2012), Coseismic and postseismic deformation of the 2011 Tohoku-Oki earthquake constrained by GRACE gravimetry, *Geophys. Res. Lett.*, 39, L07301, doi:10.1029/2012GL051104.

Wang, C.-Y., and M. Manga (2015), New streams and springs after the 2014 Mw 6.0 South Napa earthquake, Nat. Commun., 6, doi:10.1038/ncomms8597.

Williams, S. D. P., Bock, Y., Fang, P., Jamason, P., Nikolaidis, R. M., Prawirodirdjo, L., Miller, M., and Johnson, D. J. (2004), Error analysis of continuous GPS position time series, *J. Geophys. Res.*, 109, B03412, doi:10.1029/2003JB002741.

Yu, S.-B., Chen, H.-Y., Kuo, L.-C., 1997. Velocity field of GPS stations in the Taiwan area. *Tectonophysics* 274, 41–59.